STRUCTURAL CONTROLS OF SHEAR-HOSTED ÖZYURT GOLD DEPOSIT, NİĞDE, CENTRAL TÜRKİYE

A THESIS SUBMITTED TO
THE GRADUATE SCHOOL OF NATURAL AND APPLIED SCIENCES
OF
MIDDLE EAST TECHNICAL UNIVERSITY

BY

KAAN ONAT

IN PARTIAL FULFILLMENT OF THE REQUIREMENTS
FOR
THE DEGREE OF MASTER OF SCIENCE
IN
GEOLOGICAL ENGINEERING

AUGUST 2022

Approval of the thesis:

STRUCTURAL CONTROLS OF ÖZYURT SHEAR-HOSTED GOLD DEPOSIT, NİĞDE, CENTRAL TÜRKİYE

submitted by **KAAN ONAT** in partial fulfillment of the requirements for the degree of **Master of Science in Geological Engineering, Middle East Technical University** by,

Prof. Dr. Halil Kalıpçılar
Dean, Graduate School of **Natural and Applied Sciences** _____

Prof. Dr. Erdin Bozkurt
Head of the Department, **Geological Engineering** _____

Prof. Dr. Nuretdin Kaymakcı
Supervisor, **Geological Engineering, METU** _____

Examining Committee Members:

Prof. Dr. Erdin Bozkurt
Geological Engineering, METU _____

Prof. Dr. Nuretdin Kaymakcı
Geological Engineering, METU _____

Assist. Prof. Dr. Ali İmer
Geological Engineering, METU _____

Assoc. Prof. Dr. Bora Uzel
Geological Engineering, Dokuz Eylül University _____

Prof. Dr. Tolga Oyman
Geological Engineering, Dokuz Eylül University _____

Date: 26.08.2022

I hereby declare that all information in this document has been obtained and presented in accordance with academic rules and ethical conduct. I also declare that, as required by these rules and conduct, I have fully cited and referenced all material and results that are not original to this work.

Name Last name : Kaan Onat

Signature :

ABSTRACT

STRUCTURAL CONTROLS OF ÖZYURT SHEAR-HOSTED GOLD DEPOSIT, NİĞDE, CENTRAL TÜRKİYE

Onat, Kaan
Master of Science, Geological Engineering
Supervisor: Prof. Dr. Nuretdin Kaymakcı

August 2022, 136 pages

Shear-hosted Özyurt Gold Deposit is located in the Niğde Massif, a metamorphic core complex at the southern tip of Kırşehir Block, in Central Türkiye. The massif is composed of alternations of gneiss, schist, quartzite, marble, and amphibolites. It is tectonically overlain by Neotethyan ophiolites and intruded by Üçkapılı Granite. Gold mineralization is hosted along the foliation surfaces, by oxidized cataclastic breccias formed in schists along a high-angle fault network, as well as the gossans at the contacts of schist and overlying marbles. The pre-existing fault network was cut by syn-tectonic dikes that are coeval with the exhumation. The deposit undergone a supergene stage causing the breakdown of all sulfide minerals and liberating the gold in oxide zones. Two mineralization stage was observed in the polished thin sections. The primary mineralization is composed of disseminated marcasite-pyrrhotite-chalcopyrite±pyrite within the foliation surfaces. The secondary mineralization consists of pyrite±carbonate veins and veinlets followed by cross-cutting arsenopyrite-pyrite-chalcopyrite±tetrahedrite in carbonate±chlorite±sericite veins. The low-grade primary mineralization is the hypogene ore while high-grade secondary mineralization is formed due to supergene enrichment. Since schists were less competent than quartzites and marbles between ~5-13 km depths, they deformed

intensely during the exhumation of the massif. This deformation along foliation planes of schists provided fluid pathways for hydrothermal fluids. The spatial association of syn-tectonic dikes and gold mineralization within the foliation planes suggests that the intrusion might have played a role in mineralization. The possible age of the hydrothermal activity is interpreted as ~75 Ma considering the youngest dike age in the massif. The mineralization occurred at ~11 km depth and the peak temperature was ~350°C, under brittle-ductile to brittle conditions.

Keywords: Central Anatolia, Niğde Massif, Orogenic Gold, Shear-hosted Gold Deposit, Structural Control

ÖZ

ÖZYURT MAKASLAMA ZONU ALTIN YATAĞININ YAPISAL KONTROLLERİ, NİĞDE, TÜRKİYE

Onat, Kaan
Yüksek Lisans, Jeoloji Mühendisliği
Tez Yöneticisi: Prof. Dr. Nuretdin Kaymakcı

Ağustos 2022, 136 sayfa

Özyurt makaslama zonu altın cevherleşmesi, Kırşehir Bloğu'nun güney ucunda bulunan ve gnays, şist, kuvarsit, mermer ve amfibolit ardalanmasından oluşan bir metamorfik çekirdek kompleksi olan Niğde Masifi'nde yer almaktadır. Metamorfik kayalar tektonik dokanak ile Neotetis ofiyolitleri tarafından üzerlenmiş ve Üçkapılı Graniti tarafından kesilmiştir. Altın cevherleşmesi tamamen oksitlenmiş yüksek açılı fay ağında bulunan şistlerde gelişen kataklastik breşlerde, şistlerin foliyasyon düzlemlerinde ve şist ve mermer dokanağında düzlemsel gelişen gossanlarda bulunur. Önceden oluşmuş olan fay ağı, tektonizma ile eş zamanlı sokulum gösteren dayklar tarafından kesilmektedir. Hidrotermal aktivite sonrasında gerçekleşen süperjen evre, sülfit minerallerin bozunmasına ve içlerindeki altının serbest kalmasına olanak vermiştir. Mikroskop çalışmalarında iki cevherleşme evresi edilmiştir. Birincil cevherleşme evresi, foliyasyon düzlemlerinde saçınımlı markazit-pirotin-kalkopirit±pirit minerallerinden oluşmaktadır. İkincil cevherleşme evresi, pirit±karbonat damar ve damarcıklarını kesen karbonat±klorit±serizit damarlarında bulunan arsenopirit-pirit-kalkopirit±tetrahedrit minerallerinden oluşur. Düşük tenörlü birincil cevherleşme hipojen cevherleşmeyi oluştururken, yüksek tenörlü ikincil cevherleşme bunun süperjen zenginleşmiş halidir. Şistler, mermer ve

kuvarsitlere göre ~5-13 km arasında dayanımı daha düşük kayaçlar olduğu için daha yoğun deformasyon geçirmişlerdir. Şistlerin foliasyon düzlemlerinde gelişen bu deformasyon, hidrotermal sıvılar için akış yolları oluşturmuştur. Dayk ve altın cevherleşmesinin mekansal birlikteliği cevherleşmenin intrüzyon ile bir ilişkisi olabileceğini düşündürtmektedir. Hidrotermal aktivitenin, masifteki en genç dayk yaşı olan ~75 Ma zamanında gerçekleştiği tahmin edilmektedir. Buna göre cevherleşme ~11 km derinlikte ve ~350°C sıcaklıkta, gevrek-sünümlüden ila gevrek koşullar altında gerçeklemiştir.

Anahtar Kelimeler: Orta Anadolu, Niğde Masifi, Orojenik Altın, Makaslama Zonu Altın Yatağı, Yapısal Kontrol

To my grandmothers, Zehra and Halise

ACKNOWLEDGMENTS

I would like to express my gratitude to my supervisor Prof. Dr. Nuretdin Kaymakcı for his guidance, mentorship, and, all the opportunities he provided. His delicate and constructive criticism showed me to think from different perspectives and the importance of making unbiased observations.

I am grateful to Prof. Dr. İlkay Kuşcu for sharing his wisdom and experience through this journey. He showed me how to study a mineralization system and introduced me to Niğde Massif. Without his brief introduction, I would be lost in the complex geology of the massif numerous times.

I am indebted to Assist. Prof. Dr. Ali İmer for providing me a background for the recognition of ore minerals to perform thin section studies. His inspirational mineral deposits class during my BSc is the reason why I wanted to become an economic geologist.

I would like to thank Prof. Dr. Erdin Bozkurt and Prof. Dr. Bora Rojay for their fruitful discussions, Assoc. Prof. Dr. Kaan Sayıt for his help in metamorphic petrography.

This study is would not have been possible without the support of ESAN Eczacıbaşı Raw Industrial Co. Tuna Kaskatı and Hakan Yalçıntaş deserve special thanks for making this study possible.

I would like to thank Selma Ağbaba Aytekin, Erkan İstanbulluoğlu, Yağmur Han, Burak Gürel, Deniz Ekin Karabulut, Yaşar Kurşun, Hande Vona, Aydın Karataş, Alişan Gürsoy and our late friend Murat Ayyıldız for their invaluable help during my time with ESAN in Niğde.

I gratefully acknowledge the assistance of Egemen Oğuz and Seequent Ltd for providing Leapfrog Geo for modeling studies. I also wish to thank Mustafa Kaplan for reviewing and improving my 3D model with his insightful comments.

I would like to thank my fellow colleagues and friends Hakan Bora Okay, Akın Çil, Bülent Tokay, Meryem Dilan İnce, Sertan Eruysal, Boran Ersoy, Ayşegül Doğan, and Koray Taşbiçen for their constructive comments and helpful discussions.

I want to thank my close friends Volkan İmamoğlu, Arda Hasar, Yusuf Bera Bilici, Mert Aytaç, Uğur Şahin, and Faruk Küçüksubaşı for their advice and support.

My parents, Perihan Onat and Kadir Onat deserve special thanks for their unconditional support, encouragement, and patience during my studies.

Last but not least, I am grateful to Ezgi Melike Saday for her immense support during my never-ending field studies. Without her, I could not find the motivation to keep on going.

TABLE OF CONTENTS

ABSTRACT v

ÖZ vii

ACKNOWLEDGMENTS x

TABLE OF CONTENTS xii

LIST OF TABLES xvi

LIST OF FIGURES xvii

LIST OF ABBREVIATIONS xxv

CHAPTERS

1 INTRODUCTION 1

1.1 Purpose and Scope 1

1.2 Methodology 2

1.2.1 Remote Sensing and Fieldwork 2

1.2.2 3D Solid Modelling 2

1.2.3 Polished Thin Section Studies 3

1.3 Previous Studies 3

1.4 Tectonic Setting: The Kırşehir Block 14

1.5 Tectonic Setting and Geology of the Niğde Massif 17

1.5.1 Gümüşler Metamorphics 19

1.5.2 Kaleboynu Metamorphics 20

1.5.3 Aşıgediği Metamorphics 20

1.5.4 Niğde Mafic Complex 21

1.5.5 Üçkapılı Granite 22

1.6 The Exhumation of the Niğde Massif and Mechanisms 22

2 GEOLOGY OF ÖZYURT GOLD DEPOSIT 27
2.1 Deposit Lithology 30
2.1.1 Lower Kaleboynu Metamorphics 30
2.1.2 Lower Kaleboynu Schist 32
2.1.3 Upper Kaleboynu Marble 32
2.1.4 Upper Kaleboynu Schist 33
2.1.5 Marble-Schist Alternation 34
2.1.6 Beige Marble 35
2.1.7 White Marble 35
2.1.8 Üçkapılı Granite and Dike/Sill Array 36
2.1.9 Karstic Areas 38
2.2 Mineralized Outcrops 39
2.2.1 Iron Mineralization in Karstic Breccias 39
2.2.2 Copper Mineralization 41
2.2.3 Cataclastic Breccias 43
2.2.4 Gossans 44
2.3 Structural Geology 45
2.3.1 Foliations 45
2.3.2 Folds 46
2.3.3 Faults 47
2.3.4 Veins 53
3 3D SOLID MODEL OF ÖZYURT GOLD DEPOSIT 55
3.1 Modeling Procedure 55
3.1.1 Generating Topography 56

3.1.2 Importing Geologic Map and Digitizing GIS Features....58
3.1.3 Importing Drillholes....58
3.1.4 Form Interpolants and Structural Modeling....59
3.1.5 Interpretation of Drillholes and Interval Selection Procedure....59
3.1.6 Interpretation of Faults....64
3.1.7 Construction of the 3D Lithologic Model....66
3.1.8 Quantitative Oxidation Model....73
3.1.9 Construction of 3D Solid Geologic Model....74
3.2 Evaluation of 3D Solid Geologic Model....76
4 PETROGRAPHY AND ORE MINERALIZATION....81
4.1 Petrography and Alteration....81
4.2 Paragenesis....89
4.2.1 Stage 1....90
4.2.2 Stage 2....93
4.2.3 Stage 3....94
4.2.4 Stage 4....96
4.2.5 Supergene Oxidation....98
5 DISCUSSION....101
5.1 The Competence Difference and Exhumation of the Niğde Massif....101
5.2 Formation of Özyurt Gold Deposit....103
5.2.1 Host Rocks....104
5.2.2 Structure and Geometry....105
5.2.3 Ore Mineralogy and Alteration Minerals....107
5.2.4 Fluid Source and Hydrothermal Activity....107

5.2.5 Supergene Stage 108

5.2.6 Timing of Mineralization and Tectonic Setting 109

5.3 Comparison of Özyurt Gold Deposit with Deposits within Central Anatolian Metamorphic Massifs..... 111

5.4 Comparison of Özyurt Gold Deposit with Orogenic Gold Deposits 113

6 CONCLUSIONS 117

REFERENCES 119

7 APPENDICES 131

A. Offsets of a carbonate vein due to shearing along foliation planes of gneiss 131

B. Composite image of sericite-carbonate-pyroxene-albite rich layer between quartz-mica layers and ore minerals in the contact of them 132

C. The contact of quartz and pyroxene-rich layers..... 133

D. Stage 1 sooty textured colloform marcasite-pyrrhotite-chalcopyrite within a clay-carbonate vein replaced by subhedral, fresh-looking pyrite of stage 2..... 134

E. Stage 2 pyrite veinlets formed along fractures..... 135

F. Stage 3 pyrite within carbonate-chlorite vein crosscutting the foliation... 136

LIST OF TABLES

TABLES

Table 3.1. Lithology codes and simplified lithology groups used for modeling.....60

Table 5.1. Comparison of several gold deposits/prospects in Central Anatolia based on their deposit-scale characteristics with proximal intrusions.....112

LIST OF FIGURES

FIGURES

Figure 1.1: (a) Simplified tectonic map of Türkiye (b) Simplified geological map of Kırşehir Block. The study area is shown by the blue rectangle, (from Lefebvre et al., 2013). 15
Figure 1.2. Geologic map of Niğde Massif (modified from Gautier et al., 2008; after Göncüoğlu et al., 1991). The blue rectangle shows the location of the study area.18
Figure 1.3. Representative cross-section of the Niğde Massif (modified from Gautier et al., 2008). The line of section is given on the map (see Figure 1.2) 19
Figure 1.4. (a) Alternation of serpentinite and amphibolites in the upper levels of the Aşıgediği metamorphics (37.856306, 34.860103), (b) foliated serpentinite, (c) layered amphibolite..... 21
Figure 1.5. Pressure-Time diagram showing the burial and exhumation cycles of the Niğde Massif (Umhoefer et al., 2007) 23
Figure 1.6. (a) Oblique convergence along Inner Tauride subduction zone and predicted geometry of future CACC, (b) obducted ophiolite and continental magmatic belts formed in CACC due to subduction, (c) ophiolite slices stacking onto each other causing rapid burial and subsequent metamorphism and generation of crustally-derived Üçkapılı Granite (from Radwany et al., 2017) 24
Figure 2.1. General view of Özyurt Gold Deposit. Main faults related to the mineralization and position of the dike are illustrated. See the truck on the road as a scale (+: upthrown; -: downthrown) (Looking east). 27
Figure 2.2. General view of the mineralized shear zone and dike relationship (looking SE)..... 28
Figure 2.3. Geological map of the Özyurt gold deposit..... 29
Figure 2.4. Cross-section AB, see Figure 2.3 for location and legend. 30
Figure 2.5. Cross-section CD, see Figure 2.3 for location and legend. 30
Figure 2.6. General view from Aşılık Tepe Note that the Kaleboynu metamorphics are oxidized along EW faults (looking west)..... 31

Figure 2.7 Granular textured marbles from lower Kaleboynu metamorphics (37.933860, 34.837332). 32
Figure 2.8. Quartz lens formed along the foliation planes in marble (37.933073, 34.843609). 33
Figure 2.9. Banded marbles alternating with schists (37.941461, 34.849938). 34
Figure 2.10. Hematite mineralization in a karstic cavity and coatings along fractures are very common (37.932669, 34.850327). 35
Figure 2.11. Unaltered granite outcrop crosscut by late sub-vertical quartz veins with N20-30W strike (37.935555, 34.834833). 36
Figure 2.12. Clay-altered and sheared granite slice, bounded by late faults from above and bottom (37.932200, 34.842607). 37
Figure 2.13. Highly-oxidized schists around clay altered dike. The margin of the dike is slightly silicified (37.934857, 34.842581). 38
Figure 2.14. (a) General view of hematite veins in the marbles, (b) hematite coating on marble (37.945440, 34.852485). 39
Figure 2.15. Field view of: (a) clast-supported monomictic karstic breccias (37.935513, 34.841512), (b) matrix-supported monomictic karstic breccias (37.949560, 34,844354). 40
Figure 2.16. MKBX (interval within blue brackets) and PKBX (interval within red brackets) in two different drillholes. (a) PKBX interval is highly oxidized and composed of small fragments of both schist and marble. MKBX intervals consist only marble clasts within less oxidized clayey matrix. (b) PKBX interval has coarse schist clasts with marbles whereas MKBX has marble clasts in a clayey matrix. ..41
Figure 2.17. Malachite±chrysocolla stained along the fractures in schist (37.941550, 34.845745). 42
Figure 2.18. Carbonate-sulfide fracture fill. Chalcopyrite at the center and pyrite mineralization at the periphery. x10 magnification with a hand lens (OZD90- 155 m). 43
Figure 2.19. Highly-oxidized cataclastic breccias (intervals within orange brackets) and underlying MKBX (intervals within blue brackets) in a drillhole. 44

Figure 2.20. Gossans (interval within yellow brackets) in marble (interval within blue brackets). 45
Figure 2.21. Crenulated quartz-sericite schist (37.941599, 34.845614). 46
Figure 2.22. An anticline extending along the N60E direction (37.938956, 34.851707). 47
Figure 2.23. Layer-parallel shears along foliations of quartz schists. Top to the ENE shear sense determined by C-S fabrics (center) or clockwise rotated quartz lens (right) (37.931838, 34.845087). 48
Figure 2.24. A low-angle shear zone within quartz-sericite schist. C-C'-S structures show top to SE shear senses (37.929276, 34.847344). 49
Figure 2.25. Slickenlines formed at the foliations of schists (37.934516, 34.844556). 49
Figure 2.26. Strongly-oxidized high-angle fault, dike, and karstic breccias exposed at a drillhole location. (37.934700, 34.842582). 50
Figure 2.27. Photograph showing a high-angle fault and considerable oxidation in the surrounding rocks. The intensity of oxidation decreases away from the fault plane (37.934696, 34.843232). 51
Figure 2.28. Slickenlines on hematite-coated fault surface (37.941550, 34.84567). 52
Figure 2.29. Fault with silica infill (37.931320, 34.835522). 53
Figure 2.30. Vertical quartz vein with goethite coating, cross-cutting the marbles (37.931584, 34837358). 54
Figure 3.1. Diagram showing modeling procedure..... 56
Figure 3.2. Coordinate point data of the study area. 57
Figure 3.3. Topography generated from the point data shown in Figure 3.2. 57
Figure 3.4. The geologic map with digitized unit boundaries and foliation measurements are shown with disks. 58
Figure 3.5. Form interpolant surfaces, (a) looking NE, (b) looking NW..... 59
Figure 3.6. Drillholes with simplified lithologies (looking NE). 61

Figure 3.7. Interpreted drillholes in accordance with the units in the geologic map (looking NE). 61
Figure 3.8. Distribution of dike intervals. Dike_1 and Dike_2 as two parallel structures on different levels (looking NE). 62
Figure 3.9. Granite intervals in the drillholes (looking NE)..... 62
Figure 3.10. Quartzite and schists intervals in drillholes (looking NE). 63
Figure 3.11. Fe-oxides (IFM) group intervals in the drillholes. A discontinuous planar distribution can be observed in the east of the main mineralization area (looking NE). 64
Figure 3.12. General view of the faults in the main mineralization area. Red surfaces indicate hanging wall and blue surfaces indicate footwall (looking east). 65
Figure 3.13. Fault interpretation elements. Polyline on the surface, fault intercept disks, and related drillholes (looking SE)..... 66
Figure 3.14. Interpreted drillholes in accordance with the geologic map (looking NE). 67
Figure 3.15. New offset surface menu showing the selection of reference mesh and selected surface points. 68
Figure 3.16. The boundary surfaces of the units. 68
Figure 3.17. (a) The preliminary model formed accounting form interpolants and unit contacts, (b) resemblance of the preliminary model with geologic map (looking NE). 69
Figure 3.18. (a) Model with modified boundaries, (b) resemblance of the modified model with geologic map (looking NE). 70
Figure 3.19. General view of resulting lithologic model with drillholes (looking NE). 71
Figure 3.20. Close-up view of the mineralization area, (a) from the resulting lithologic model, (b) from the geologic map (looking east)..... 72
Figure 3.21. The blending structural trend used for the oxidation model and selected strength and range values of each element (looking NW). 73

Figure 3.22. Correlation of oxidation ratings with mineralization on the map (looking down). 74
Figure 3.23. The general view of the 3D solid geologic model (looking east)..... 75
Figure 3.24. ENE-WSW cross-section showing the oxidation distribution in units and faults (looking NNW)..... 75
Figure 3.25 The outcrop differences between (a) the resulting model and (b) the geologic map (looking NE)..... 77
Figure 3.26. The granite bodies in the study area (looking NE)..... 78
Figure 3.27. Dike_1, Dike_2 and IFM_selected in NW-SE cross-section (looking SE)..... 79
Figure 3.28. Comparison of (a) cross-section AB and (b) cross-section AB in the model..... 79
Figure 3.29. Comparison of (a) cross-section CD and (b) cross-section CD in the model..... 80
Figure 4.1. Altered schist showing alternating layers of quartz and K-feldspar-carbonate-sericite crosscut by a barren carbonate vein. Clay alteration is commonly observed. Pyrite and iron oxides are disseminated within foliation from OZD97-172.80 m under (a) PPL, (b) XPL, (c) reflected PPL. 82
Figure 4.2. General view of a marble samples. (a) calcite-albite-epidote assemblages in the marble from OZD103-264.40 m under XPL, (b) kink bands observed in twinning of calcites from OZD103-272.80 m under XPL, (c) hematite mineralization in a karstic cavity from OZD103-270.20 m, reflected PPL. 84
Figure 4.3. Quartz-muscovite-biotite gneiss contains pyrite-chalcopyrite disseminations from OZD-97, 423.30 (gneiss) under (a) PPL, (b) XPL and (c) reflected PPL..... 86
Figure 4.4 (a) Pyroxene clusters within albite, also coarse biotites. Actinolite as spikes developed in albite, from OZD91-296.20 m, XPL, (b) pyroxene boudins between quartz from OZD97-423.30 m, XPL, (c) Clinopyroxenes and open-space filling, botryoidal textured calcite vein from OZD91-295.90 m, XPL. 88
Figure 4.5. The paragenetic sequence of the Özyurt gold deposit. 89

Figure 4.6. Stage 1 mineralization in OZD97-143.70 m. (a) General view of the ore minerals (black) in the contact of the clinopyroxene-sericite-albite bearing layer with quartz-sericite schist, XPL, (b) general view of the ore minerals, reflected PPL, (c) Pyrrhotite-marcasite-chalcopyrite association. Marcasite is replacing the pyrrhotite with spikes from the periphery, reflected PPL, (d) Mica enclosed by ore minerals in the contact of clinopyroxene-sericite-albite bearing layer, XPL, (e) Mica enclosed by marcasite and chalcopyrite, reflected PPL, (f) pleochroic greenish chlorite replacing mica, PPL.....91
Figure 4.7. Stage 1 mineralization (a), (b), (c), (d) in OZD97-168.10 and (e), (f) in OZD97-143.70 m. (a) Stage 1 mineralization in clay-carbonate vein cross-cutting a big quartz vein, XPL, (b) Stage 1 marcasite and chalcopyrite with sooty texture replaced by stage 2 pyrite at the periphery of the clay-carbonate vein, reflected PPL, (c) a close-up view to the clay-carbonate vein. Stage 1 marcasite-chalcopyrite intergrowth is observed. Stage 2 pyrites replacing stage 1 minerals, reflected PPL, (d) pyrrhotite-marcasite-chalcopyrite cluster in the foliation. Marcasite is replacing the pyrrhotite, reflected PPL, (e) quartz-sericite layer contains ore minerals whereas carbonate-biotite layer does not, PPL, (f) pyrrhotite and marcasite within the foliation of quartz-sericite schist, reflected PPL. 92
Figure 4.8. Stage 2 mineralization in OZD97-414.30m. (a) Pyrite mineralization within a shear zone cross-cutting foliation obliquely, reflected PPL, (b) ore-bearing shear zone consists of sericite-biotite-carbonate while the rock contains sericite-K-feldspar-biotite, XPL, (c) pyrite vein formed in a fracture orthogonal to the foliation, reflected PPL, (d) carbonate-pyrite vein cross-cutting the foliation, reflected PPL. 93
Figure 4.9. Stage 3 mineralization (a), (d) from OZD97-172.80 m and (b), (c), (e), (f) from OZD103-175.30 m. (a) Arsenopyrite-carbonate vein cross-cutting stage 2 pyrite, reflected PPL, (b) ore-bearing sericite-chlorite vein cross-cutting the foliation of quartz-sericite schists, XPL, (c) pyrite and arsenopyrite within the sericite-chlorite vein, reflected PPL, (d) arsenopyrite-chalcopyrite-tetrahedrite within carbonate vein,

reflected PPL, (e)chalcopyrite and possible tetrahedrite aggregate, reflected PPL, (f) arsenopyrite and pyrite found together, reflected PPL. 95
Figure 4.10. Stage 4 mineralization (a), (b), (c) from OZD97-414.30 m, (d) from OZD103-158.50 m, (e) from OZD103-157.80 m, (f) from OZD103-172.80 m. (a) Carbonate vein cross-cutting the foliation of K-feldspar-quartz-sericite-biotite schist, XPL, (b) Fe-ox(?), pyrite and chalcopyrite near the carbonate vein, carbonate vein filled a fault, drag folds are visible, reflected PPL, (c) carbonate vein hosted a fault. On the left, pyrite undergone cataclasis. On the right, a brittle microfault cuts pyrite, reflected light (d) carbonate veins crosscutting sericite-quartz-biotite schist, faults rotate a slice of the foliation, XPL, (e) pyrites were cataclastically deformed and were cross-cut by a late carbonate vein, reflected PPL, (f) pyrite cluster was cross-cut by a carbonate vein which is also cross-cut by a pyrite veinlet, reflected PPL. 97
Figure 4.11. Supergene stage in cataclastic breccias (a), (b), (c), (d), (e) from OZD103-299.20 m, (f) from OZP-14. (a) Hematite within cataclastic zones, reflected PPL, (b) possible trace of an arsenopyrite, PPL, (c) native gold is observed within the possible arsenopyrite, reflected PPL, (d) electrum and native gold near goethite cluster of cataclastic breccia, reflected PPL, (e) possible electrum or native gold with ilmenite dissemination, reflected PPL, (g) oxidized anastomosing shear zones within quartz-sericite schist, XPL. 99
Figure 5.1: Strength profiles of quartzite (Rutter and Brodie 2004), schist (Shea and Kronenberg 1993) and marble (Schmit et al., 1980) lithologies with respect to increasing depth. The strain rate is taken as 10^{-15} s^{-1} (from Chen and Nabelek, 2017). 102
Figure 5.2. The competence difference between schists and marbles in the Niğde Massif. 103
Figure 5.3. Conceptual NNE-SSW-trending cross section showing the architecture of Özyurt gold deposit. (not to scale) 104
Figure 5.4. High-grade gold mineralization in cataclastic breccias along high-angle faults and adjacent foliation planes (37.934615, 34.842553). 106

Figure 5.5. The diagram showing supergene enrichment and leaching through meteoric water activity. (from Robb, 2005) 109
Figure 5.6. Pressure-Time-Depth diagram showing the burial and exhumation cycles of the Niğde Massif (modified from Umhoefer et al., 2007). The geothermal gradient is taken as 33 °C/km according to Gautier et al. (2008). Metamorphic facies and fault rocks depths are depicted according to temperature (adopted from Colvine et al., 1988; after Simpson 1986; Sibson, 1977, 1983). 111
Figure 5.7. Fault order hierarchy in Val d'Or district (Robert, 1990). 114
Figure 5.8. Proposed orogenic gold models according to different sources: (a) Magmatic-hydrothermal source model, (b) metamorphic source model (Groves and Santosh, 2016; Groves et al., 2020). 115

LIST OF ABBREVIATIONS

ABBREVIATIONS

ab	albite	Fe-ox	iron-oxide
act	actinolite	grt	garnet
As	arsenic	gt	goethite
Au	gold	hem	hematite
bt	biotite	ilm	ilmenite
clc	calcite	Kfs	K-feldspar
carb	carbonate	mrc	marcasite
ccp	chalcopyrite	ms	muscovite
chl	chlorite	po	pyrrhotite
cly	clay minerals	py	pyrite
cpx	clinopyroxene	qtz	quartz
Cu	copper	rt	rutile
el	electrum	ser	sericite
ep	epidote	tet	tetrahedrite
Fe	iron		

CHAPTER 1

INTRODUCTION

1.1 Purpose and Scope

From the beginning of early human history to modern times, various civilizations mined metals in Niğde Massif like tin, antimony, copper, mercury, iron, lead, zinc, tungsten, and gold (Klein, 1971; Akçay, 1995; Tümüklü et al., 2018; Powell et al., 2021). The latest archeological study in the southeast massif shows that Kestel mine, the world's oldest tin mine, extends to the early Bronze Age. Although it was not mined for gold, by-product gold was mined from hematite-quartz veins. (Powell et al., 2021)

The most recent mineral exploration strategies have led the mining companies to look into underexplored areas of the massif for new discoveries. The newly found Özyurt Gold Deposit (ÖGD) within the Niğde Massif is a good example of this effort. Understanding of characteristics and mechanism of the ÖGD may help to improve targeting strategies to explore undiscovered gold deposits in Anatolia and elsewhere. In this context, this study aims to understand the main characteristics and structural development of the ÖGD based on a local and regional geological perspective. The specific research questions addressed in this thesis include;

1. the associated lithologies and alterations with the mineralization,
2. the structural features controlling the geometry of the ore body,
3. temporal relationships and pressure-temperature-depth conditions during mineralization,
4. the possible source of the gold,
5. the type of mineralization in the Özyurt gold deposit.

1.2 Methodology

1.2.1 Remote Sensing and Fieldwork

Before the fieldwork, a remote sensing study was performed to prepare a lineation map to determine the probable faults of the study area and its surroundings. The lineaments were grouped into three depending on the presence of appreciable off-set features on the images. The fault category involves apparent off-sets, while the probable fault category involves linear features with prominent morphological features on the images, but lack of obvious off-set features. The lineaments category involves marked linear features on the images, but they do not display any off-set or prominent morphological feature to be classified as faults. All interpreted features were checked in the field, and then their categories were assigned on the final geologic map and the database.

An extensive fieldwork has been carried out between June-November 2021, which includes ground truthing of interpreted lineaments and detailed mapping of geologic features and metamorphic packages also involving measurement of planar and linear features such as foliation, shear zone, fault, mineral lineation, etc. The mapping was performed on 1 m ground resolution Worldview imagery obtained from Digital Globe.

At the end of the fieldwork, field observations and final geologic map of Özyurt area were combined to prepare cross-sections, which were also used for the development of 3D solid model of the study area with the help of drillhole data.

1.2.2 3D Solid Modelling

By the drillhole data provided by Esan Eczacıbaşı Raw Industrial Co., a 3D solid geological model was created by using Leapfrog Geo software of Seequent Limited. A total number of 141 drillholes, the geological map, and cross-sections were used

to create the model. The geologic map was utilized to determine the extent of the model. The intervals along each drillhole were interpreted into geologic units in Leapfrog Geo, by checking their core photos and the location of specific drillhole on the geologic map. After all of the drillholes were interpreted, a lithologic model was produced in accordance with the geologic map, cross sections and regional structural trends.

The faults related to mineralization were modeled by combining the surface fault traces with the fault intercepts along the nearby drillholes. Both surface fault traces and all intercepts of the same fault were included in a surface to show the 3D geometry and extent of each fault.

Modeling procedures and assumptions are discussed in more detail in Chapter 3.

1.2.3 Polished Thin Section Studies

A total of 19 polished thin sections were prepared from the selected intervals of OZD 91-97-103 drillholes and also one surface sample collected from the field, to determine petrography, ore and gangue mineralogy, dominant alterations, and deformation styles. The polished thin sections are prepared at İstanbul Technical University (İTÜ) and analyzed at Middle East Technical University (METU).

1.3 Previous Studies

Due to its unique geological characteristics and importance in the geology of the Tauride-Anatolide Belt, Niğde Massif has been studied by numerous researchers mainly during the last century. Below, a chronological summary of those studies focused on the massif's regional and economic geology is presented.

In the literature, Niğde Massif is first mentioned as a distinct rock assemblage and mapped as a circular granitic body on a 1/2000000 geological map of Turkey (Tchihatcheff,1869).

Phillipson (1918) showed the massif as a granite intrusion in his 1/3700000 scaled geological map.

Tromp (1942) first mentioned Niğde Series as a distinct body of rocks with pre-Devonian age.

Blumenthal (1941, 1952) did the first brief petrographic studies and defined the metamorphic rocks in the massif and grouped the metamorphic lithologies under the name of Niğde Complex.

Okay (1955) prepared the first geologic map of the massif with a scale of 1/100000.

Klein (1968) worked on the geology and geochemistry of the Niğde Massif in the scope of Hg-Sn-W prospection project led by the General Directorate of Mineral Exploration and Research (MTA). This study marked that antimony, mercury, tungsten and iron deposits are prominent within the massif.

Klein (1970) divided Niğde Massif into three packages as lower, middle and upper series according to the dominant lithologies. This study suggested that the metamorphism of the massif occurred before the Variscan Orogeny and there are three different structural deformation stages as pre-Variscan Orogeny, early Alpine and Alpine.

Klein (1971) studied the relationship between structural features and the economic occurrences of antimony, mercury and tungsten mineralizations. The study concluded that both dikes and mineralized quartz veins are structurally controlled. Klein also observed that marble and gneiss contacts host stibnite-scheelite-cinnabar-quartz veins, which is another structural control.

İleri (1972) studied the stibnite mineralization in Niğde metamorphics and divided the massif into four different packages, with a succession of 11 kilometers.

Viljoen and İleri (1973) studied the geology of the massif and stibnite mineralization. They grouped metamorphics as Pozantıdağ Massif with four formations as Maden formation, Ilıca formation, Kılavuz formation and Çamardı formation. According to

this study, stibnite mineralization in the massif occurs as open-space quartz veins (Klein, 1971) and as planar lens-like bodies along distinct stratigraphic levels; thus, showing a lithologic control.

İleri (1975) suggested stibnite mineralization is formed after the deformation of the massif and discussed the importance of lithologic control of mineralization.

İleri and Köksay (1977) concluded that the stibnite mineralization in the Niğde Massif is epigenetic.

Göncüoğlu (1977, 1981) prepared a 1/25000-scaled geologic map of west Niğde Massif and grouped metamorphic rocks into Niğde group and defined packages as Gümüşler formation, Kaleboynu formation, Aşıgediği formation, Sineksizyayla formation (gabbro), Üçkapılı granodiorite and meta-ophiolitic units. His studies include detailed inspections of the metamorphic rocks based on field study and microscopic studies. According to these studies, the Niğde Massif had experienced a series of complex deformation history. Older E-W to ENE-WSW recumbent folds verging to the north and relatively younger N-S to NNE-SSW upright open folds are defined in the massif. Göncüoğlu noticed that the folded flysch sediments are unconformably overlain the metamorphic rocks in the south-southeast of the massif. Flysch sediments are also unconformably overlain by a conglomerate and sandstone which are covered by Neogene tuffs (subsequently called as Cappadocian volcanics)

Yıldız (1978) carried out a study on mercury occurrences in Turkey. In the study, he noted that Gümüşler area contains an economic stibnite, scheelite deposit with cinnabar.

Özgüneyli (1978) worked on the base metal, iron, wolframite and gold occurrences in the massif, and suggested that the mineralizations are epigenetic.

Yetiş (1978) studied the Ecemiş Fault Zone, which delimits the massif in the east and claimed that the fault zone is of post-Paleocene to pre-Lutetian age.

Oktay (1982) worked on the geology of the Ulukışla Basin and established its stratigraphy. He claimed that the magmatic rocks in the basin are of magmatic-arc

origin. The opening of the basin is suggested to be constrained between early Paleocene to late Paleocene, or even up to middle Eocene in some places.

Göncüoğlu (1982) reported U/Pb ages of zircons extracted from paragneiss of Gümüşler formation and concluded that paragneisses should have been originated from a Proterozoic terrane with an age of 2059±77 Ma.

Oygür et al. (1985) made a compilation of the geology of the Niğde Massif as well as historical and current mineralizations. The report focuses on the potential iron mineralization zones in the massif.

Göncüoğlu (1986) performed a geochronological study on the Üçkapılı granodiorite of the massif and acquired the crystallization age as (lower Cenomanian) 95±11 Ma by using whole rock Rb/Sr and cooling ages as 77.8±1.2 Ma and 76.5±1.1 Ma by using whole rock/mineral K/Ar methods. According to this study, Üçkapılı granodiorite is a post-tectonic intrusion, which is derived from either by partial melting of the continental crust or from a considerably contaminated continental crust. The study concluded that ophiolite obduction and main metamorphism event occurred prior to Cenomanian.

Çağatay and Pehlivan (1988) worked on the mineralogy of tin mineralization around Celaller in the SE of the massif. They claimed that cassiterite mineralization is related to the quartz-hematite veins.

Gizaw (1992) studied the geology of the massif in Gümüşler area, prepared a 1/25000-scaled geological map and defined the occurrences of antimony deposits. He suggested that Sb-Hg mineralization in the Gümüşler formation is associated with the quartz veins along gneiss-marble contacts or within marble. According to the geochemistry results of the samples, Sb-Hg±Au and trace amounts of base metals are determined in the mineralized zones. Gizaw proposed a model for mineralization in the area where the hydrothermal fluids circulated through the faults providing fluid pathways and deposition sites for the mineral deposits. Also, fluid-wall rock interaction is responsible for the subsequent deposition of ores within the carbonates.

Kuşcu (1992) studied the geology of SE massif and the Madsan antimony deposit near Çamardı. He claimed that the mineralization is confined to the quartz±stibnite±pyrite veins hosted in the gneisses and marbles of the Gümüşler Formation. Geochemical studies show that trace cinnabar and gold are present within the veins. Sericitic alteration and silicification are the common wall rock alteration assemblages with minor chloritization. Kuşcu (1992) proposed lateral secretion and source bed models for the mineralizations and claimed that a source bed is more accountable for the genesis of Madsan antimony deposit.

Kuşcu and Erler (1993) studied the deformations of stibnites of the Madsan antimony deposits and suggested three different deformation phases. They proposed secondary remobilization of a mineralized source bed to explain the formation of Madsan deposit.

Kuşcu et al. (1993) studied the geology of the Çamardı region. There, Gümüşler formation overlies Aşıgediği formation with an unconformity. The whole metamorphic package is intruded by Üçkapılı Granodiorite and its pegmatite dikes. Conglomerate and sandstone bearing Çamardı formation (Late Cretaceous-Paleocene) are composed of the metamorphic clasts from the massif and overlies the massif with a nonconformity whereas it is overlain by the Evliyatepe formation (early - middle Eocene). Ulukışla Basin fill is composed of; from bottom to top; chaotic flysch and volcano-sedimentary rocks of the Ovacık formation and volcano-sedimentary and volcanic rocks of the Ulukışla Formation. Authors reported Celaller thrust and Üçkapılı normal fault as the prominent neotectonic features of the region.

Akçay (1994, 1995) studied the geology of Gümüşler area and prepared a model for the evolution of the hydrothermal fluids responsible for the formation of the mineral deposits. There are two different types of deposits as Sb±Hg±W±Ba±Au veins with subsequent Ba-Sb mineralization (Rasih İhsan deposit) and Hg±Sb±Au breccias (Mehmetler Yurdu Sivrisi Tepe-MYST). The vein deposits are observed in marbles and at gneiss-marble contacts along E-W striking and north dipping faults. Felsic dikes are reported to have a spatial relationship with both breccia and vein deposits.

The most common wall rock alteration is silicification but lesser sericite alteration, kaolinization, dolomitization and tourmalinization through the distal parts of mineralization are reported. Fluid inclusion studies revealed that the mineralization occurred in a broad temperature range from 350°C to 150°C with a salinity of 8±2.5 to 4 eq. wt. % NaCl, suggesting an increasing association of non-magmatic fluids. Pyrite and stibnite sulfur isotope compositions vary from -4.3 to +2.2‰ and approximately 18‰ for barite; thus, indicating a magmatic sulfur origin for sulfides/sulfates. Akçay (1995) pointed out that gold mineralization extends up to 37.3 ppm at MYST but concluded that ores are not economic due to their small sizes.

Whitney and Dilek (1997) pointed out the similarity of Miocene core complexes in West Anatolia and Central Anatolia based on petrologic and structural observations and the timing of exhumation. They suggested that the development of Niğde Massif is related to a north-dipping Alpine-type collision of continental fragments causing thickening and followed by exhumation due to thermally weakened/thickened crust. Their U-Pb monazite ages between 20 and 13.7 Ma from the Üçkapılı Granite contradicts with the earlier Rb/Sr whole-rock age of 95±11 Ma of Göncüoğlu (1986).

Whitney and Dilek (1998) conducted petrological and thermobarometric studies and prepared a P-T-t diagram for the high-grade metamorphics of the Niğde Massif. The results imply that the massif experienced a possible second stage of burial history.

Kuşcu and Erler (1999) proposed three deformation stages based on the textures of stibnite and pyrite from the Madsan antimony deposit (SE of Niğde Massif). According to this study, pressure lamellae in the first stage, curved pressured lamellae and annealing texture in the second stage and truncation of pressure lamellae represent the third deformational stage. Authors claim that the deformations developed at 0.2 MPa pressure and at nearly 180°C conditions.

Floyd et al. (2000) studied geochemistry and the tectonic setting of ophiolites and metabasites in the Central Anatolian Crystalline Complex (CACC). They divided the Upper Cretaceous ophiolitic-metabasic rocks into three different groups: the first one, stratiform ophiolites, has geochemical similarities and show subduction

characteristics while they were developing. The second group is composed of a mixture of sheared blocks in an ophiolitic mélange, shows MORB-like geochemistry with some OIB basaltic rock and are related to accretionary complex development (Ankara Mélange). The third one consists of amphibolites of the Kaleboynu metamorphics of the Niğde Massif reflects OIB type geochemistry and is thought to be involved in rifting of the Tauride-Anatolide carbonate platform. The authors also claimed that the ophiolites on the CACC and Ankara Mélange belong to an oceanic lithosphere, which was obducted onto the Tauride-Anatolide carbonate platform during the Late Cretaceous.

Fayon et al. (2001) dated Kırşehir, Akdağ (northeastern CACC) and Niğde massifs (southern CACC) in Central Anatolian Crystalline Complex using apatite fission-track method. Whereas northern massifs yield an age of ≈47-32 Ma, southern Niğde Massif yield ≈12-9 Ma; these ages are interpreted as exhumation ages. Therefore, the Niğde Massif was still at depth when Kırşehir and Akdağ massifs were at the surface. They proposed that Niğde Massif was unroofed along an oblique wrench zone related to the Ecemiş Fault Zone.

Whitney et al. (2001) subdivided the Central Anatolian Crystalline Complex (CACC) into four different tectonic blocks, according to their P-T-t paths, as Kırşehir (NW), Akdağ (NE), Aksaray (W) and Niğde (S) massifs. They concluded that the Niğde Massif is different than others since it is developed as a core complex within a wrench-dominated setting. The study also shows the evidence for a secondary low pressure-high temperature metamorphism over the regular P-T path of high-grade metamorphics and apatite fission-track ages ranging between 12-9 Ma (Miocene).

Gautier et al. (2002) observed that metamorphics of the Niğde massif are nonconformably overlain by early Eocene sedimentary rocks in the SE. The basal conglomerates of this sedimentary package include both metamorphic and granite pebbles; thus, the metamorphics and the intrusion should have been on the surface by early Eocene at the latest, and the granite intrusion which was previously dated as 12-9 Ma (apatite fission-track) and 20-13.7 Ma (U-Pb, monazite) possibly reflects

another thermal event, proposedly widespread late Neogene Volcanism. A detachment fault zone is observed in the northern parts of the massif, between meta-ophiolitic rocks at the top and high-grade metamorphics at the bottom. Field studies led to a discussion of whether a tectonic contact or a nonconformity developed between metamorphics and Eocene sedimentary rocks. Assuming the synchronous regional extension in Kırşehir Block, the authors suggested that the massif was affected by an intense extension between Campanian to Paleocene.

Whitney et al. (2003) performed U-Pb SHRIMP and $^{40}Ar/^{39}Ar$ analysis of granite and metamorphic rocks of the Niğde Massif. The results are interpreted to record melting interval of 92-85 Ma, peak metamorphism temperature of 725°C, and age of 91.0±2.0 Ma and cooling ages of 83-74 Ma. Considering the unroofing of the massif in the Late Cretaceous and new radiometric age data, the authors interpreted that the crust melted and incipient intrusion during the peak metamorphic conditions and/or decompression caused by the extension.

Whitney and Hamilton (2004) dated garnet-sillimanite gneiss from the Kırşehir Massif in central Anatolia and acquired the age of 84.1±0.8 Ma (Late Cretaceous). They also and compared the massif with the Menderes Massif in western Anatolia. They argued that such an age difference (gap) should not exist for the similarly-evolved terranes; thus, the authors concluded that Anatolia formed due to the collision of various microcontinents.

Fayon and Whitney (2007) reviewed the apatite fission-track (AFT) ages from the high-grade metamorphics of the Niğde Massif, assessing if there is resetting due to Neogene Volcanic activity. Combining geological observations, models of AFT ages together with track length data and thermal modeling, they claimed that AFT ages were not disrupted by any thermal event; therefore, timing of AFT ages report exhumation of the Niğde Massif.

Umhoefer et al. (2007) and Whitney et al. (2007) suggested that the Niğde Massif had undergone two different burial-exhumation cycles, name by *"yo-yo tectonics",* due to the interplay of transpressional and transtensional deformation along the

Central Anatolian Fault Zone (CAFZ). By evaluating all radiometric and biostratigraphic ages and geologic data, they constrained the durations of exhumation and burial cycles for the Niğde Massif.

Gautier et al. (2008) observed two different synchronous shearing trends in the metamorphics of the Niğde Massif. The high-grade metamorphic rocks of the massif are considered as lower unit. The authors determined that the lower levels of the lower unit show top-to-SSW shearing, while the higher levels of that unit show top-to-NE/ENE shearing. By using $^{40}Ar/^{39}Ar$ ages and previously published age data, they suggested that two opposing shearing events occurred synchronously. Authors interpreted oblique shearing as a lateral underflow event where the lower crust flowed horizontally oblique to the extensional direction.

Idleman et al. (2014) presented new age data that sheds light on to reheating and reburial history of the Niğde Massif. Although four of eight samples are consistent with the cooling age of ≈75 Ma ($^{40}Ar/^{39}Ar$ muscovite ages from gneiss), the other four samples taken near the faulted unconformity contact of the Ulukışla Basin rocks have perturbed spectra. The thermal perturbation age is interpreted as reheating event peaked at ≈30 Ma. Transpression caused by the Ecemiş Fault resulted in reburial. Reburial event is considered as the reason for thermal perturbation.

Tümüklü et al. (2016) reported that iron mineralization in the Niğde Massif has a hydrothermal origin and is accompanied by copper and gold.

Tokoğlu et al., (2016) studied the shear zone-hosted gold occurrence in metapelitic rocks near Gümüşler, Niğde. The mineralization in the area is grouped as (i) Au-Hg-As mineralization at cataclasites along the foliation surfaces and (ii) Au-Pb mineralization along low-angle faults with cataclasites, crosscutting the foliations. The second mineralization is hosted in quartz veins with stibnite±galena±marcasite ±gold.

Ray (2016) studied the Niğde mafic complex (NMC), a part of the Central Anatolian Ophiolite (CAO), which is obducted onto the CACC, during the closure of the

Neotethys Ocean. NMC is composed of a metamorphosed assemblage of diabase, gabbro, plagiogranite and ultramafic rocks and overlies the metamorphic rocks of Niğde Massif, tectonically. The mineral assemblage of the NMC gabbros indicates supra-subduction conditions. Geothermometry studies from hornblende and plagioclase minerals show that the NMC experienced middle to upper amphibolite facies conditions, which is similar to the metamorphics of the massif.

Demircioğlu and Eren (2017) studied the SE of Niğde Massif and differentiated at least four distinct ductile deformation stages.

Ballı (2017) studied the geology of south and east Niğde and mapped the faults in the area.

Radwany et al. (2017) performed whole-rock analyses on gabbro pebbles of middle Miocene sedimentary rocks which derived from both CAO and Tauride ophiolites and Late Miocene sedimentary rocks which originated from CAO. Authors interpreted that the uplift of the Niğde Massif occurred in late Miocene, forming a topographic high. Arching of the Taurides changed the distribution of sediments and their depositional centers.

Seyitoğlu et al. (2017) and Gürer et al. (2018) claimed that İvriz detachment fault is responsible for the exhumation of the CACC. Where it is defined the İvriz detachment fault juxtaposes the metamorphic Bolkar group of Taurides and Paleocene-Eocene Ulukışla Basin fill. Two groups similarly suggest that the detachment fault should be active during Late Cretaceous-Eocene time interval (~80 and ~48 Ma).

Tümüklü et al. (2018) and Altuncu et al. (2018) reported the known historical mines. In the region, tin, iron, mercury, antimony, lead and zinc mineralizations were observed. They noted that mineralizations commonly occurs along the discontinuity zones.

Tosunbaş (2019) and Safalı (2019) studied the Sb mineralization in the Niğde Massif; they concluded that mineralization is found as bands or in fault breccias. Native gold is also present with antimony as determined in polished thin sections.

Çoban (2019) studied geology and structural features of the east of Niğde Massif and Ulukışla Basin concluded that they deformed together due to the closure of Inner-Tauride Ocean before Oligocene. In the neotectonic stage, strike-slip and normal faults are developed.

Özözlü (2019) compared Esendemir Tepe skarn mineralization with Horoz skarn mineralization. While the first one formed after the intrusion of Esendemir Tepe diorite (60-56 Ma) into limestone levels in the Ulukışla Basin, the second one is formed after the emplacement of Horoz granitoid (56-47 Ma) into Tauride carbonates. The study includes the mineral assemblages of both mineralizations in each phase.

Radwany et al. (2020) conducted a geochronology study and provided new ages for the CAO and NMC. Comparing the crystallization age of an unmetamorphosed CAO fragment (~ 91 Ma), $^{40}Ar/^{39}Ar$ hornblende age of highly metamorphosed metagabbro from NMC (~87 Ma) and $^{40}Ar/^{39}Ar$ biotite age of highly metamorphosed quartz-feldspathic rock with metaophiolite rocks (~78 Ma) shows that the ophiolites are imbricated on each other and metamorphosed with the rocks of the Niğde Massif, whereas unmetamorphosed CAO fragments in CACC obducted on land in the north. Authors claimed that this difference is caused by oblique convergence.

Umhoefer et al. (2020) discussed the tectonic history of the Ecemiş Fault Zone with Niğde Massif and Taurides. The second burial of the Niğde Massif with the sediments of the Ulukışla Basin in Late Eocene-Oligocene occurred due to a transpressional deformational stage and resulted in a north vergence thrusting. The change of tectonic regime to transtensional deformation stage in Late Oligocene caused the onset of the second exhumation of the Niğde Massif and at least 25 km sinistral displacement along the Ecemiş Fault. The authors suggested that the

transtensional stage started at 23-22 Ma, based on geochronological and thermochronological data.

Demircioğlu and Coşkuner (2020) suggested that multi-phased deformations caused NE-SW plunging recumbent folds in the metamorphic rocks of the Niğde Massif.

Tümüklü and Tosunbaş (2021) studied Gümüşler Sb mineralization, discussing two structural controls: (i) quartz band parallel to the foliation planes in the metamorphics, (ii) fault breccias along faults. Ore and gangue mineralogy are stibnite±cinnabar and quartz±barite, respectively. Quartz crystals locally contain native gold.

1.4 Tectonic Setting: The Kırşehir Block

Kırşehir Block (KB) comprises the Central Anatolian Crystalline Complex (CACC) (Göncüoğlu et al., 1991), which was previously named as Central Anatolian Massif (Ketin, 1955) or Kırşehir Massif (Görür et al., 1984) or Kırşehir Complex (Lünel, 1985). The KB is a triangular shaped, tectonic block in Central Türkiye (Figure 1.1) delimited in the west by the Tuzgölü Fault, in the east by the Ecemiş Fault Zone and in the north by the Ankara-Erzincan Suture zone. The rock assemblages of the Kırşehir Block are grouped into four main categories as (i) metamorphics, (ii) ophiolites, (iii) intrusives and (iv) volcanics and sedimentary rocks. The crystalline rocks of the KB include various rocks metamorphosed to greenschist to amphibolite facies rocks (Central Anatolian Metamorphics). The intrusive bodies range from granitoids to syenitoids (e.g., Aydın et al., 1998; Lefebvre et al., 2013). The other crystalline rocks of the KB include mafic and ultramafic rocks and epi-ophiolitic deposits belonging to supra subduction zone ophiolites (Central Anatolian Ophiolites) (Yalınız et al., 1996, 1997, 2000; Yalınız and Göncüoğlu, 1998; Yalınız, 2008)

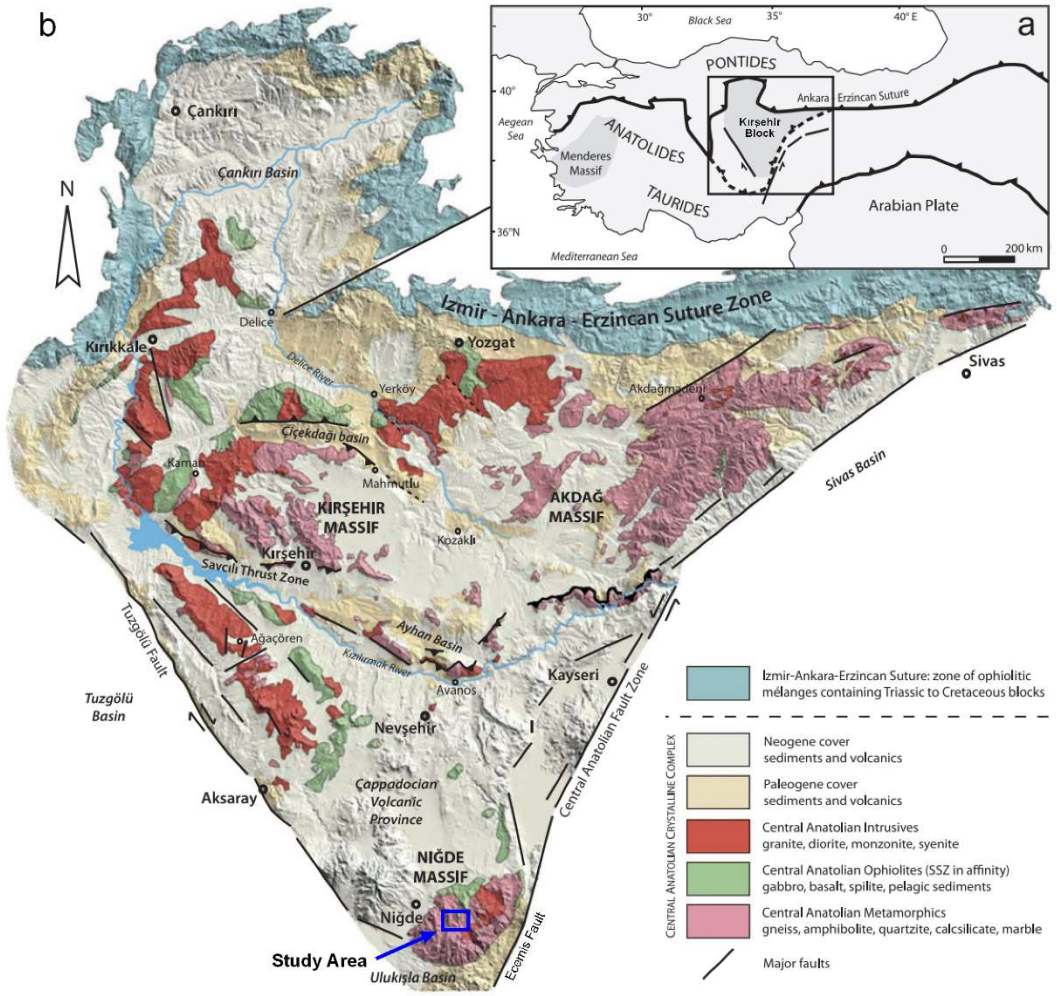

Figure 1.1: (a) Simplified tectonic map of Türkiye (b) Simplified geological map of Kırşehir Block. The study area is shown by the blue rectangle, (from Lefebvre et al., 2013).

Kırşehir Block experienced collision and subsequent amalgamation with Pontides along the Ankara-Erzincan Suture Zone (Şengör and Yılmaz, 1981), and with the Taurides along the Inner-Tauride suture (Görür et al., 1984, Gülyüz et al., 2013; (Figure 1.1). Closure of the intervening oceans around the Kırşehir Block gave way to the obduction of ophiolites during the Late Cretaceous which have been intruded and overlain by widespread post-collisional magmatic rocks (İlbeyli and Pearce, 1997; Boztuğ, 1998, 2000; Aydın et al., 1998; Düzgören-Aydın et al., 2001; Kuşcu et al., 2002).

The Paleozoic-Mesozoic metamorphics are consistently observed all over the Kırşehir Block and are composed of gneiss, mica-schist, quartzite, marble, calc-silicate and amphibolite. Hence, they are named as Central Anatolian metamorphics (CAM) (Göncüoğlu, 1977; Göncüoğlu et al., 1991). The Central Anatolian metamorphics are observed in the three massifs of the Kırşehir Block; Kırşehir Massif (northwest) (Seymen, 1981), Akdağ Massif (northeast) (Vache, 1963) and Niğde Massif (south) (Göncüoğlu, 1981). The massifs show similar lithologies and have undergone a Barrovian-type metamorphism (HT/MP regional metamorphism conditions up to upper amphibolite facies (Erkan, 1976; Seymen 1981; Göncüoğlu et al., 1991). The peak metamorphic conditions in the Kırşehir Block are determined as 6-8 kbar and 700-800°C at 91-92 Ma and overprinted by a secondary metamorphic event reaching 2-3 kbar and 300°C, locally (Kocak and Leake, 1994; Whitney and Dilek, 1988; Whitney et al., 2001). The metamorphics are tectonically overlain by ophiolites.

Late Cretaceous Central Anatolian Ophiolites (CAO) (Yalınız et al., 1996, 1997, 2000, 2008; Yalınız and Göncüoğlu, 1998) refers to the isolated supra-subduction (SSZ)-type ophiolites dispersed all over the Kırşehir Block as klippen. CAO consists of mainly mafic rocks such as gabbro, plagiogranite, basalts, rarely felsic volcanics, ultramafics and pelagic sedimentary rocks. The crystallization age of the CAO is estimated as ~ 90 Ma by U-Pb zircon dating of plagiogranites at Sarıkaraman (van Hinsbergen et al., 2016). Although most of the CAO rocks have not been metamorphosed or have only been slightly metamorphosed under sub-greenschist facies conditions, metagabbros in the Niğde Massif (Sineksizyayla metagabbro of Göncüoğlu, 1977) show ductile deformation and higher-grade metamorphic conditions reaching middle to upper amphibolite facies conditions. They are subgrouped as the Niğde mafic complex (NMC) to differentiate them from the rest of the CAO (Ray, 2016; Radwany et al., 2017, 2020).

Central Anatolian Intrusives (CAI) intrude both metamorphics (CAM) and ophiolitic fragments (CAO) and covers vast areas (Erler and Göncüoğlu, 1996). CAI has calc-alkaline characteristic and shows felsic composition such as syenite, granite and

monzonite. The timing of intrusions within the Kırşehir Block determined as 95-75 Ma by several researchers (Akıman et al., 1993; Aydın et al., 1998; İlbeyli et al., 2004, Köksal et al., 2004). The intrusions are syn to late-kinematic with the exhumation of the massifs in the Kırşehir Block (Whitney and Dilek, 1998; Whitney et al., 2003; van Hinsbergen et al., 2016).

All units in the Kırşehir Block are unconformably overlain by Upper Cretaceous-Quaternary sedimentary and volcanic rocks. Contemporaneous and subsequent depressions formed prior to the exhumation of massifs acted as depocenters to sediments and volcanics. Basins located at the edges of the Kırşehir Block such as Ulukışla, Tuzgölü, Haymana and Çankırı basins, documented the evidence for Late Cretaceous to Recent deposition (Görür et al., 1984, 1998; Erdoğan et al., 1996; Çemen et al., 199; Kaymakcı et al., 2009). Also, intracontinental Yıldızeli, Sorgun, Kaman Çiçekdağı and Ayhan basins recorded sedimentation between Paleocene-Eocene times (Göncüoğlu, 1992; Görür et al., 1998; Advokaat, 2011; Advokaat et al., 2014; Gülyüz et al., 2013; Tokay, 2015). Neogene magmatism, mainly comprising rhyolite, rhyodacite and ignimbrites, covers large areas in the south of the Kırşehir Block and named as the Cappadocian Volcanic Province (CVP) (Le Pennec et al., 1994; Toprak, 1998) (Figure 1.1).

1.5 Tectonic Setting and Geology of the Niğde Massif

Niğde Massif is an extensional metamorphic core complex located at the southernmost edge of the Kırşehir Block (Whitney and Dilek, 1997, 1998, 2003; Gautier et al., 2008) (Figure 1.2). Low to moderate dipping foliation measurements outward from the center of the massif to the periphery and vergence of folds at different localities supports an antiformal dome structure (Whitney and Dilek, 1997, Gautier et al., 2008).

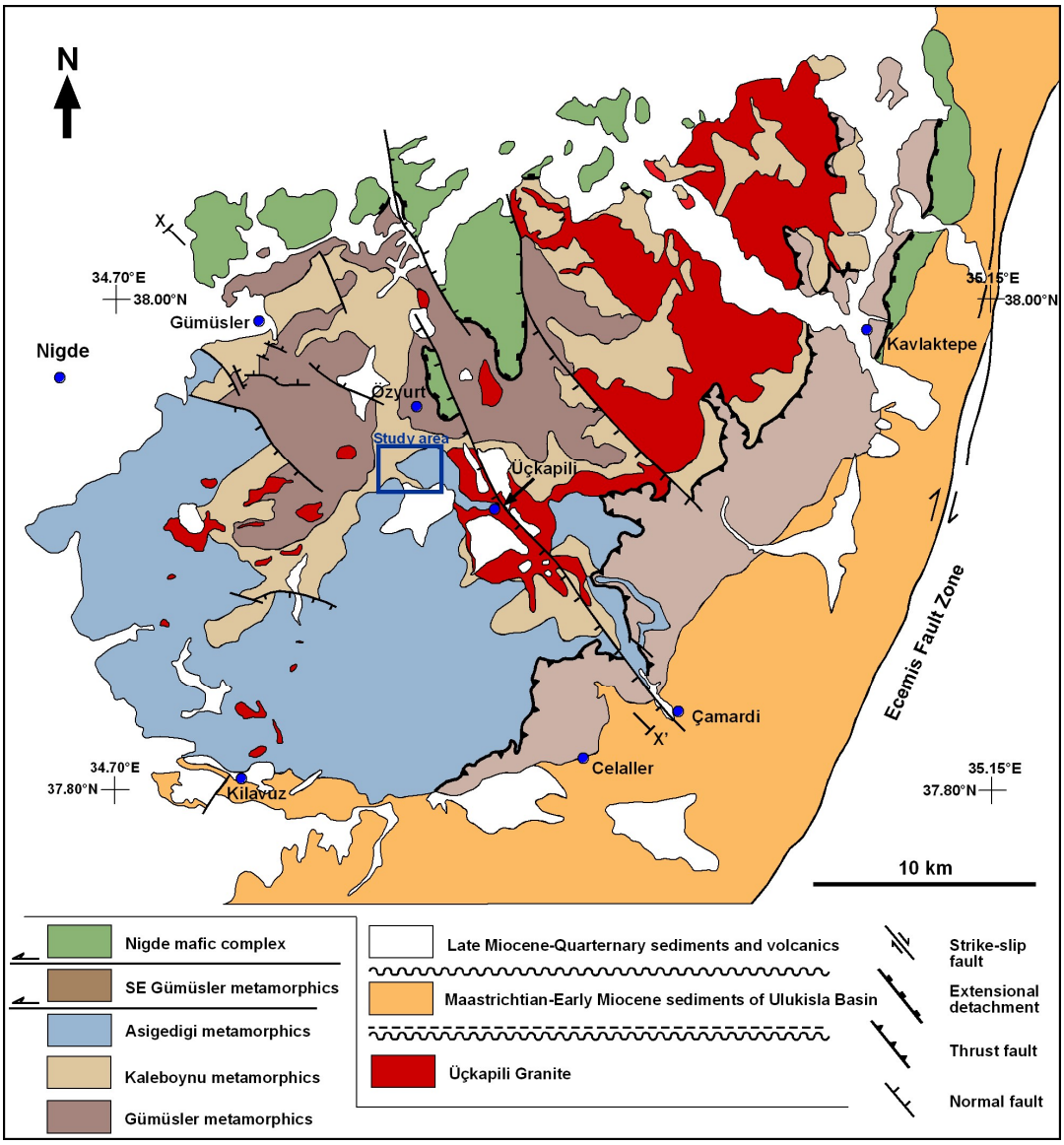

Figure 1.2. Geologic map of Niğde Massif (modified from Gautier et al., 2008; after Göncüoğlu et al., 1991). The blue rectangle shows the location of the study area.

The massif is composed of high-grade metamorphics, meta-ophiolites and intrusives. The metamorphics of the massif are grouped from bottom to top as Gümüşler metamorphics, Kaleboynu metamorphics and Aşıgediği metamorphics (Göncüoğlu, 1977, 1981). Niğde mafic complex (NMC) is composed of mainly meta-gabbros and tectonically overlies the metamorphic sequence with a tectonic boundary. Üçkapılı Granite intrudes all units of the massif and covers a large outcrop area in the massif, especially in the NE of the massif.

Niğde Massif is either unconformably overlain by or has a faulted contact with early Eocene Ulukışla basin sedimentary rocks, which suggests that the massif should have been exhumed at the earliest by the Eocene (Gautier et al., 2002) (Figure 1.2 and Figure 1.3). Locally, tuffs of the Cappadocian Volcanic Province overlie the metamorphics unconformably (Figure 1.2).

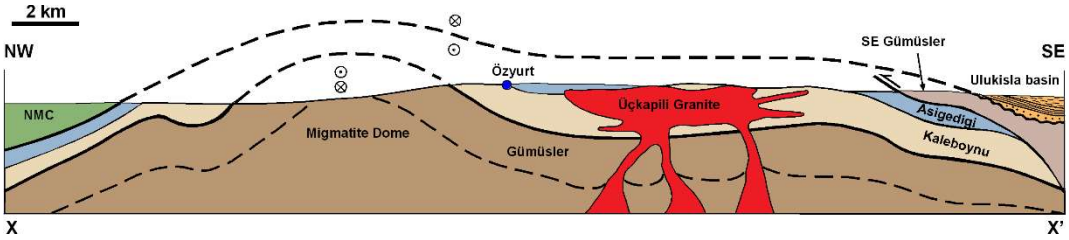

Figure 1.3. Representative cross-section of the Niğde Massif (modified from Gautier et al., 2008). The line of section is given on the map (see Figure 1.2)

1.5.1 Gümüşler Metamorphics

Gümüşler metamorphics is the lowermost unit of the Niğde Massif. It is dominantly characterized by paragneiss with amphibolite, marble and bands of calcsilicate-marble-quartzite (Göncüoğlu, 1977, 1981). It starts with sillimanite-biotite gneiss occasionally shows evidence for partial melting. This unit had undergone highest metamorphic conditions during the burial cycles. Structurally lowest portions of the Gümüşler metamorphics experienced partial melting which resulted in the formation of migmatites in some exposed localities. Within the Gümüşler metamorphics, garnet-sillimanite paragneiss are formed at 5-6 kbar and >700°C and thermometry results of garnet-biotite pair yielded a temperature interval of 680-780°C (Whitney & Dilek, 1998). The parent rock of the gneiss is interpreted as psammopelitic sediments (Göncüoğlu, 1981).

The southeastern part of the massif contains a slice of the Gumusler Metamorphics (Figure 1.2).This slice is essentially considered as the Gümüşler metamorphics since it shows also metapelitic origin; yet, it lacks migmatitic textures, and amphibolite/garnet mica schists of this unit indicate relatively lower formation

temperatures (630-650°C) (Whitney et al., 2001). Unlike the migmatitic Gümüşler metamorphics at the core, this slice is tectonically located on the Aşıgediği metamorphics.

1.5.2 Kaleboynu Metamorphics

Kaleboynu metamorphics overlies the Gümüşler metamorphics. The unit consists of alternation of marble and mica-schist with amphibolite and quartzite bands. The alternating nature of the unit can be easily recognized at the outcrop scale. Its thickness of the unit is approximately 600 m. The protolith of the Kaleboynu metamorphics is thought to be an alternating series of sandstone-claystone and limestone with basic volcanics and tuff intercalations (Göncüoğlu, 1981).

1.5.3 Aşıgediği Metamorphics

Aşıgediği metamorphics overlies the Kaleboynu metamorphics. It is generally composed of massive calcitic/dolomitic marbles with minor amphibolite, mica-schist and quartzite inter layers in the upper levels (Göncüoğlu, 1981). Aşıgediği metamorphics are approximately 2000 m thick.

At the higher levels of the Aşıgediği metamorphics, there are alternations of foliated serpentinites (different from meta-gabbros of the NMC) and amphibolite layers with marbles (Figure 1.4). The serpentinites and amphibolites are intensely foliated and metamorphosed up to amphibolite facies (Gautier et al., 2008). Göncüoğlu et al. (1991) explain the alternating nature of these rocks as ophiolitic nappe fragments and underlying olistostromes while Floyd et al. (2000) and Gautier et al. (2008) interpret the alternated series as a metamorphosed ophiolitic mélange.

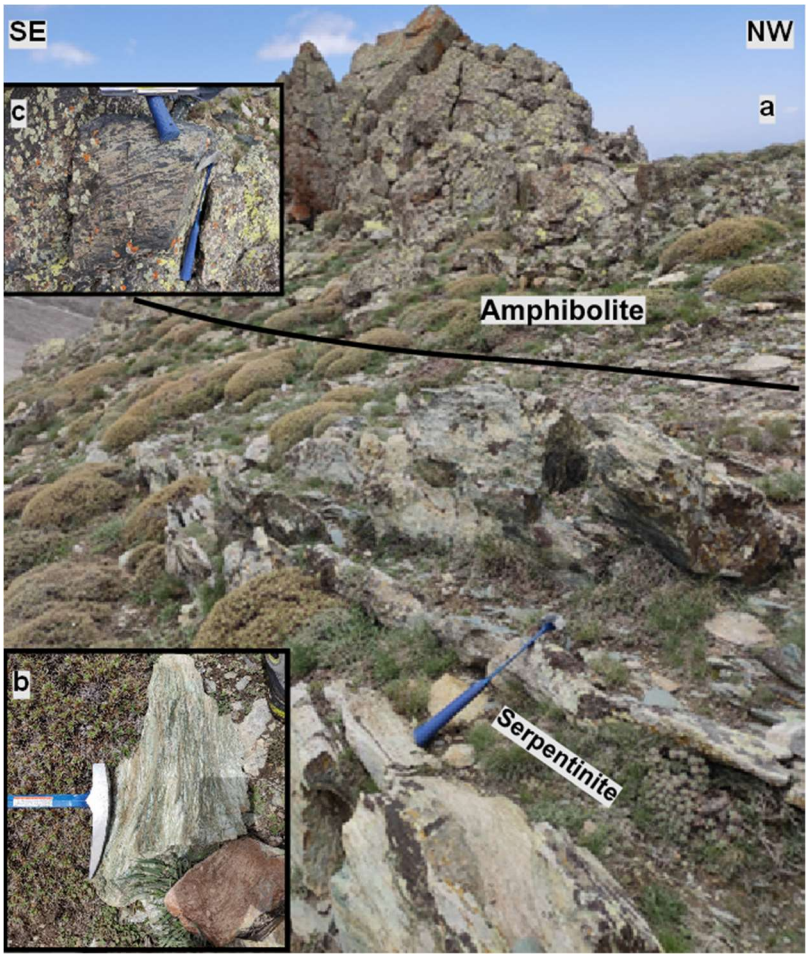

Figure 1.4. (a) Alternation of serpentinite and amphibolites in the upper levels of the Aşıgediği metamorphics (37.856306, 34.860103), (b) foliated serpentinite, (c) layered amphibolite

1.5.4 Niğde Mafic Complex

NMC (Ray, 2016, Radwany et al., 2017, 2020) or previously called Sineksizyayla Metagabbro (Göncüoğlu, 1977) refers to the massive ophiolitic fragments metamorphosed up to amphibolite facies. Although NMC is geochemically similar to the rest of the CAO, the latter shows no metamorphism or very low metamorphism, to greenschist facies conditions (Floyd et al., 2000). In contrast, NMC shows a higher degree of metamorphism.

NMC consists of dominantly metagabbros but also contains metaplagiogranite, metadiabase and metaperidotite (Radwany et al., 2020). It shows ductile deformation, and the foliation planes are coherent with the underlying metamorphics (Radwany et al., 2017, 2020). Between metamorphics and the NMC, flat to low-angle, mylonitic shear zones occurs (Gautier et al., 2008; Radwany et al., 2017). NMC is deformed together with the metamorphic series, showing similar metamorphic facies with underlying rocks, and both are intruded by Üçkapılı Granite (Figure 1.2 and Figure 1.3).

1.5.5 Üçkapılı Granite

Üçkapılı Granite is a peraluminous, crustally-derived (S-type), two-mica granite and crops out at vast area in the center (Üçkapılı Village) of the massif. It is generated by the partial melting of continental crust during crustal thickening and subsequent decompression (Whitney et al., 2003). It intrudes into metamorphic rocks and the NMC in the massif. Although intrusion cuts all metamorphic units in the massif, the main intrusion level is along the Kaleboynu metamorphics (Göncüoğlu, 1981). The aureole zone contains andalusite and cordierite in metapelitic rocks and its thickness ranges from centimeters to decimeters (Göncüoğlu, 1986). The granite intrusion is accompanied by a dense array of dikes and sills in aplitic and pegmatitic compositions. Üçkapılı Granite is a late-kinematic intrusion since it undergoes the same deformation with the surrounding basement rocks (Gautier et al., 2008).

1.6 The Exhumation of the Niğde Massif and Mechanisms

The metamorphics of the Niğde Massif are composed of gneiss, schist, marble and amphibolite; the protoliths of these rocks are a mixed carbonate-clastic sequence (Göncüoğlu, 1977; 1981; Atabey et al., 1990), deposited on the platform of Neotethys Ocean (Umhoefer et al., 2007).

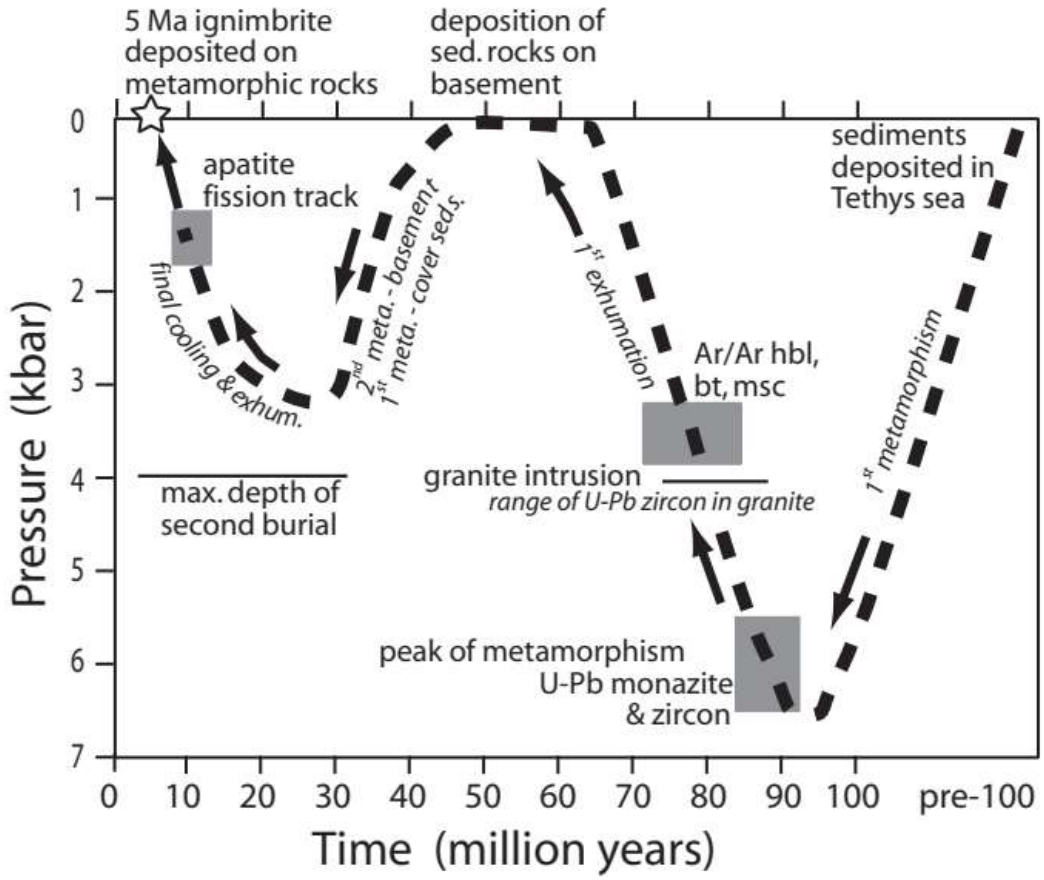

Figure 1.5. Pressure-Time diagram showing the burial and exhumation cycles of the Niğde Massif (Umhoefer et al., 2007)

Niğde Massif experienced two different burial and exhumation cycles (Umhoefer et al., 2007) (Figure 1.5). The first burial occurred in Late Cretaceous due to crustal thickening caused by stacking of ophiolite slices onto each other, presumably during closure of the so-called Inner Tauride oceanic basin. (Tekeli et al., 1984; Andrew and Robertson, 2002; Parlak and Robertson, 2004). The oblique convergence of Tauride and Anatolide blocks in the NE direction along the Inner Tauride subduction zone resulted in with obduction of ophiolites and subsequent continental magmatism along the western boundary of the Kırşehir Block (Radwany et al., 2017, 2020; van Hinsbergen et al., 2016) (Figure 1.6). The interleaving of ophiolite slices caused duplex structure development and was followed by crustal thickening in the southern tip of the Kırşehir Block (Radwany et al., 2017, 2020). Increasing metamorphic

conditions combined with initial decompression caused the partial melting of the crust and generation of the Üçkapılı Granite (Whitney et al., 2003).

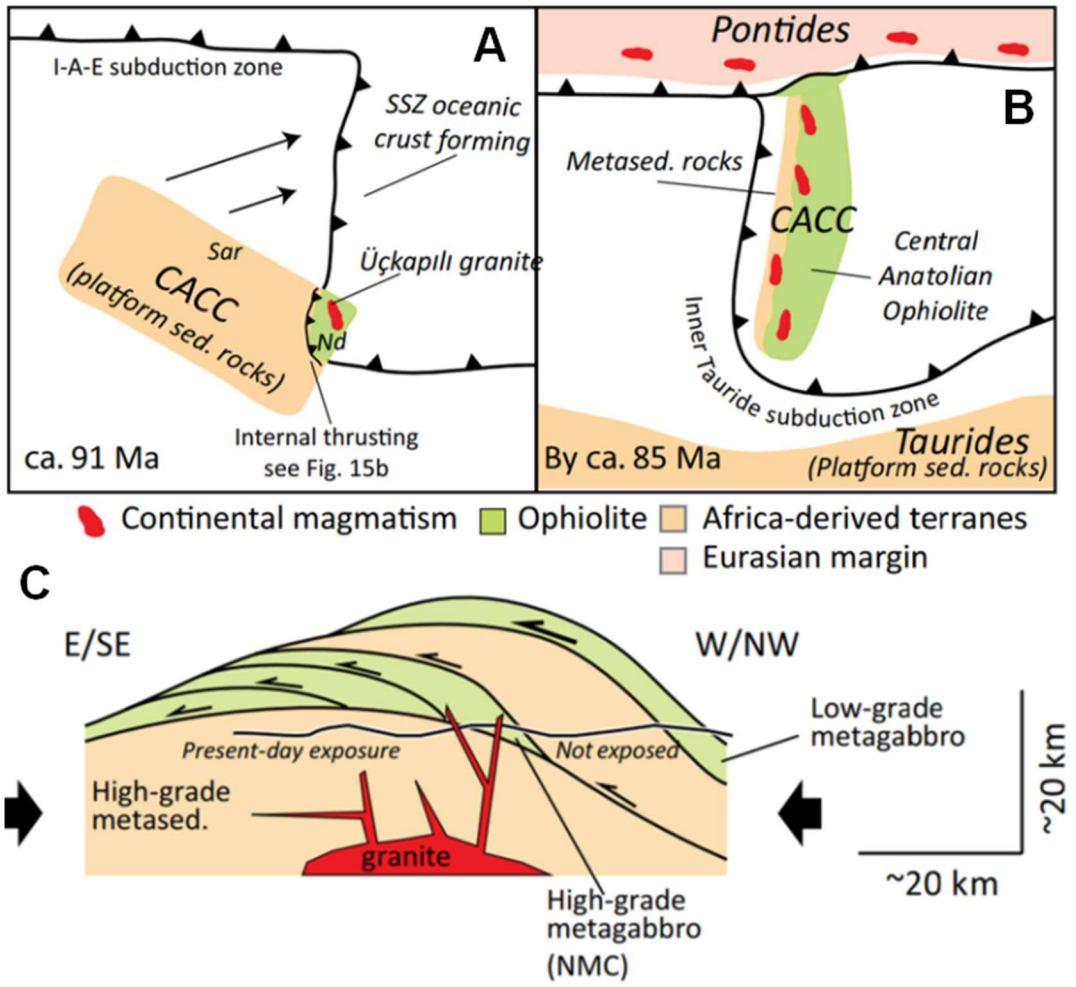

Figure 1.6. (a) Oblique convergence along Inner Tauride subduction zone and predicted geometry of future CACC, (b) obducted ophiolite and continental magmatic belts formed in CACC due to subduction, (c) ophiolite slices stacking onto each other causing rapid burial and subsequent metamorphism and generation of crustally-derived Üçkapılı Granite (from Radwany et al., 2017)

The peak metamorphic conditions at the Niğde Massif occurred at 725°C and were dated as 91.0±2.0 Ma from zircon rims and 84.7±0.7 Ma from monazite of sillimanite schists by using U-Pb geochronology (Whitney et al., 2003). Therefore, the peak metamorphic condition period is marked as 85-91 Ma for the massif. Migmatization and partial melting of the middle crust occurred due to high temperature gradients. Partial melting accompanied by subsequent unroofing resulted in the formation and

emplacement of the Üçkapılı Granite. Similar geochronologic measurements of both crystallization and cooling times of high-grade metamorphics and deformational history similar to the high-grade metamorphics indicate syn to late-extensional emplacement of the Üçkapılı Granite between 85-76 Ma (Whitney et al., 2003; Gautier et al., 2008)

Niğde Massif is nonconformably overlain by Paleocene-Eocene aged, conglomeratic Çamardı Formation of the Ulukışla Basin which includes pebbles of metamorphics and the granite (Gautier et al., 2002). Çamardı Formation intertongues with the Evliyatepe Formation, which is composed of marine sedimentary rocks and fauna, deposited during early to middle Eocene times (54-46 Ma, Gautier et al., 2002). Therefore, the massif had been exhumed in the early-middle Eocene and completed the first burial and exhumation cycle (Figure 1.5). The unconformity plane between the metamorphic rocks of the massif and the Çamardı Formation is sheared (Gautier et al., 2002; Umhoefer, et al., 2007) (Figure 1.3).

Folding and reverse faulting observed in the Paleocene-Eocene strata of the Ulukışla Basin and overprinting greenschist facies metamorphism in both Niğde Massif and the Ulukışla Basin fill suggests a secondary burial and exhumation cycle (Whitney et al., 2007; Umhoefer et al., 2007, 2020) (Figure 1.5). The peak metamorphic conditions (6-10 km burial depth) at the eastern massif are determined as 30.5± 5 Ma by Idleman et al. (2014) and the massif then started to exhume and cool after 25 Ma (Fayon et al., 2001; Idleman et al., 2014). Apatite-fission track (AFT) ages of 17-9 Ma are interpreted as the final exhumation/cooling period of the massif and adjacent Ulukışla Basin fill (Fayon et al., 2001; Whitney et al., 2007; Umhoefer et al., 2007, 2020). Gautier et al. (2002) argue that protracted Neogene magmatism in the Cappadocian Volcanic Province or a concealed intrusive at depth might have thermally reset the system; however, others claimed that (Whitney et al., 2007; Fayon and Whitney, 2007; Umhoefer et al., 2007) AFT ages (17-9 Ma) are considerably older (at least 5-15 Ma older) than ignimbrites of Neogene magmatism in the region. early-middle Miocene Çukurbağ Formation unconformably overlies

Paleocene-early Miocene Ulukışla Basin strata thus indicating a second stage of unroofing of the Niğde Massif.

There are three different hypotheses on the exhumation mechanism of the Niğde Massif.

Umhoefer et al. (2017) and Whitney et al. (2017) suggested that transpressional to transtensional stress regime variations caused by the activity of the Ecemiş Fault Zone is responsible for the mechanism of repeated burial and exhumation cycles in other words, *"yo-yo tectonics"*.

On the other hand, Gautier et al. (2008) discussed the presence of two synchronous shear zones in the massif; one is more ductile and observed in the deeper levels with top-to-SSW direction, other is more brittle and occured in the upper levels, along top-to-NE/ENE direction. Authors suggests that two oblique contemporaneous shears resulted in due to a lateral underflow, in other words, a lateral flow of lower crust in a direction oblique to the extension direction; thus, two distinct shear domains and a migmatitic core could co-exist in a metamorphic dome.

Seyitoğlu et al. (2017) and Gürer et al., (2017) similarly accounted for the existence of regional-scale İvriz detachment, a low-angle northward-dipping detachment extending from the Taurides and Afyon Zone to north Kırşehir Block. It is thought to be active between Late Cretaceous and early Eocene (~80 - ~48 Ma). While metamorphic massifs are interpreted as the exhumed parts of this detachment, Late Cretaceous-Eocene sedimentary basins have developed on the depressions formed due to differential exhumation of the detachment.

CHAPTER 2

GEOLOGY OF ÖZYURT GOLD DEPOSIT

The Özyurt gold deposit (Figure 2.1 and Figure 2.2) is located 3 km SSW of Özyurt Village. Geologically, the deposit lies at the contact of the Kaleboynu and Aşıgediği Metamorphics. Doing detailed field studies, the metamorphics were subdivided into several sub-units. In this chapter, the geologic map of the deposit (Figure 2.3) and related cross-sections (Figure 2.4 and Figure 2.5) are presented and each sub-unit, mineralized outcrops, and structural geology are discussed, in detail.

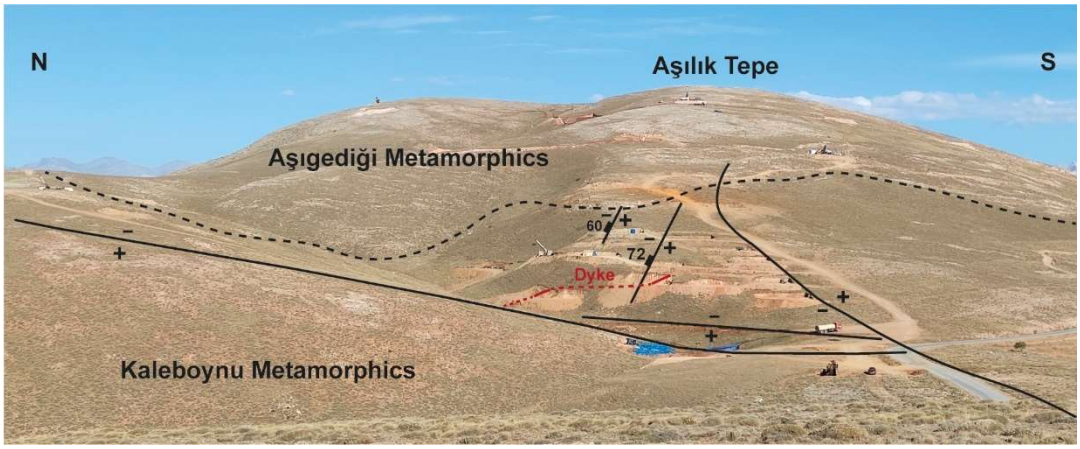

Figure 2.1. General view of Özyurt Gold Deposit. Main faults related to the mineralization and position of the dike are illustrated. See the truck on the road as a scale (+: upthrown; -: downthrown) (Looking east).

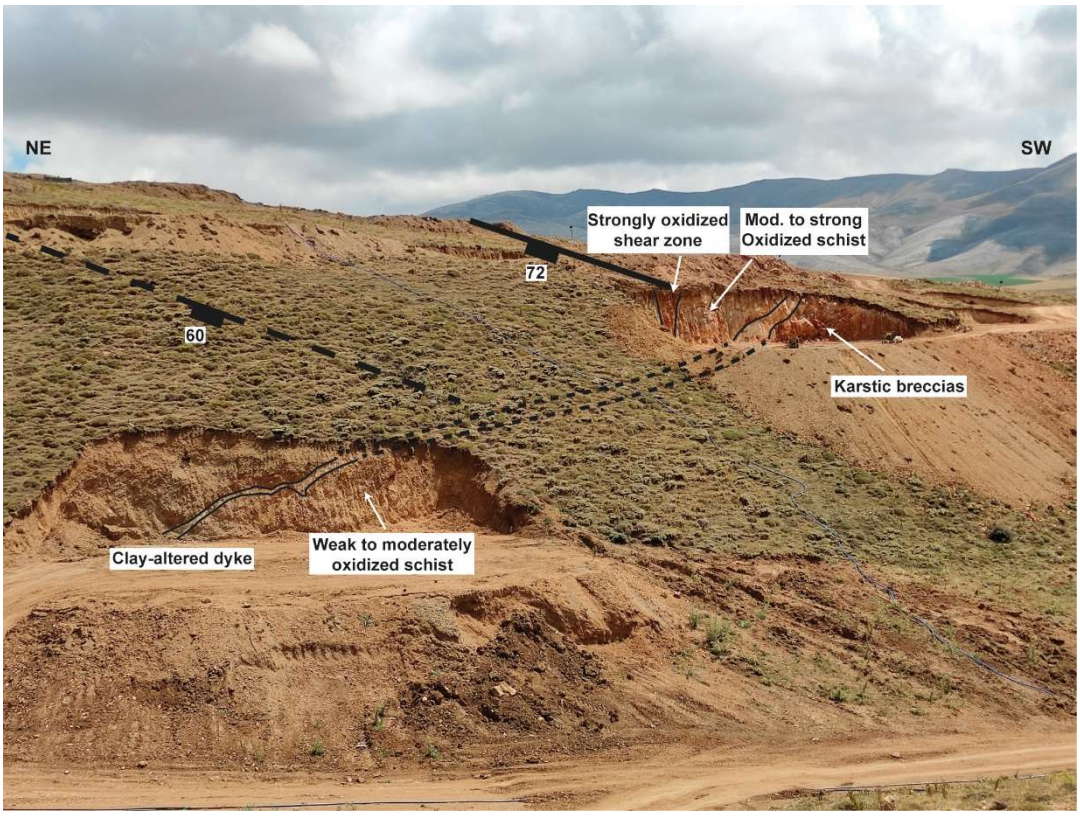

Figure 2.2. General view of the mineralized shear zone and dike relationship (looking SE).

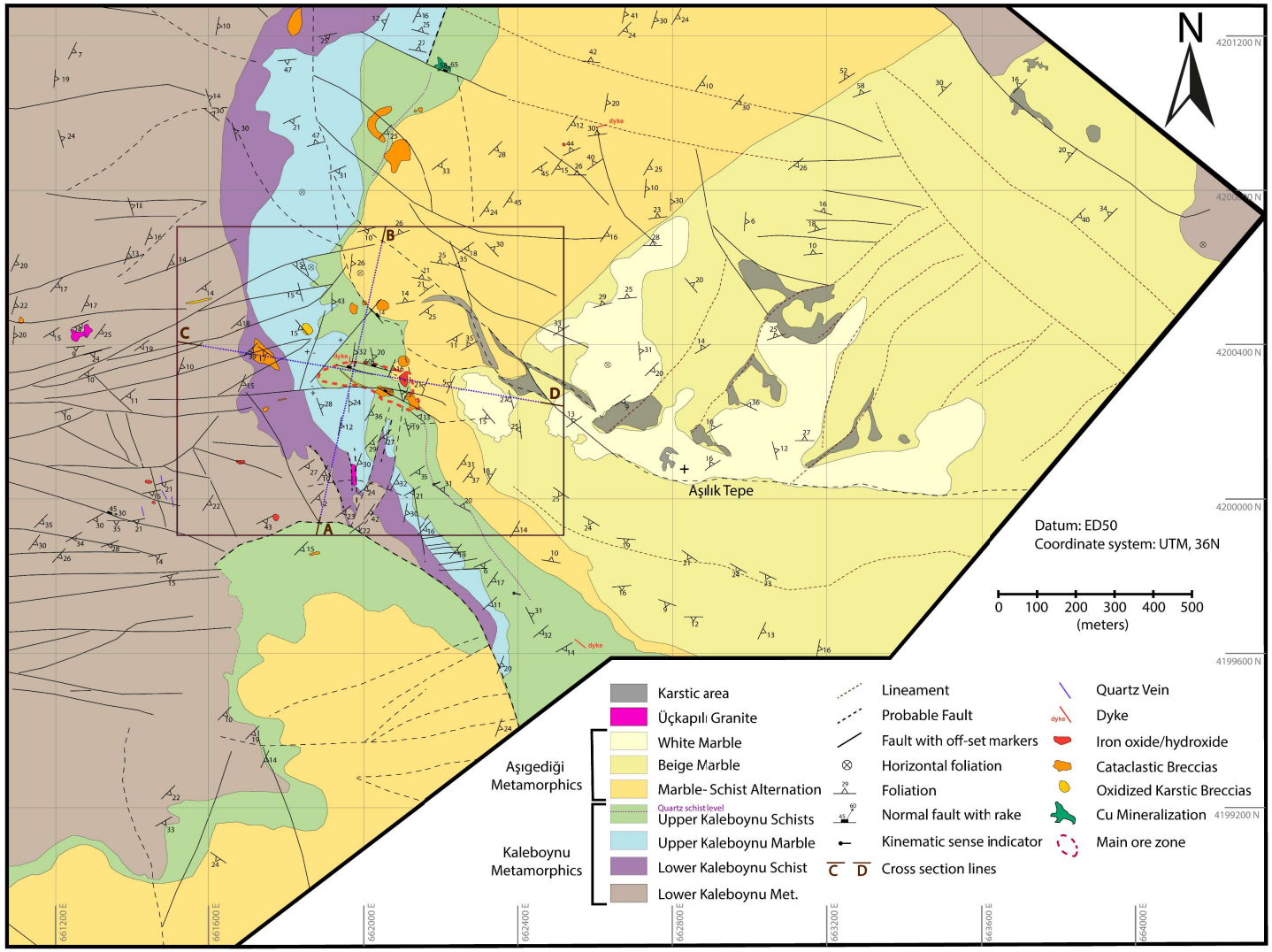

Figure 2.3. Geological map of the Özyurt gold deposit

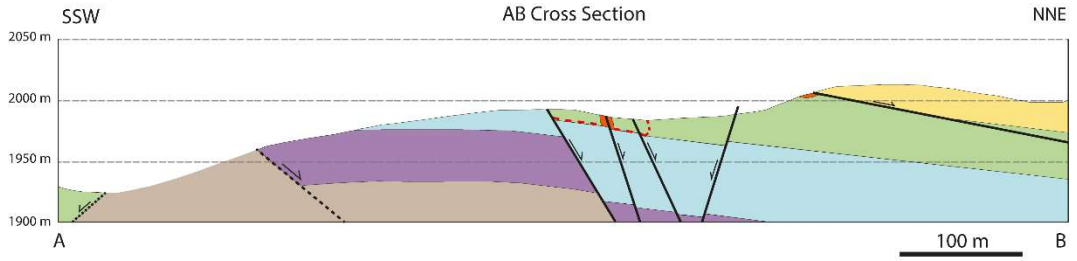

Figure 2.4. Cross-section AB, see Figure 2.3 for location and legend.

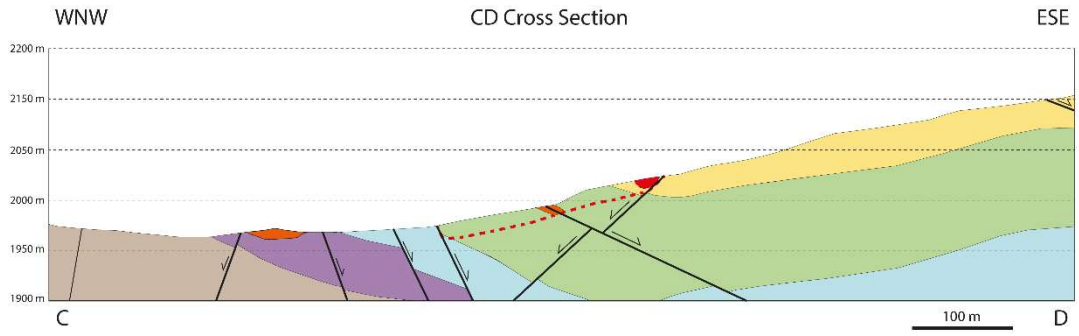

Figure 2.5. Cross-section CD, see Figure 2.3 for location and legend.

2.1 Deposit Lithology

In the study area, Kaleboynu and Aşıgediği metamorphics are divided into seven different units, all of which have been intruded by the Üçkapılı Granite.

2.1.1 Lower Kaleboynu Metamorphics

Lower Kaleboynu metamorphics consists of alternation of marble, amphibolite and quartz-sericite schists. It is the predominant unit in the eastern part of the study area. It is not possible to trace the same lithologic levels consistently in the field since this unit is highly deformed by E-W-striking faults (Figure 2.6). Sericite alteration is observed in the marbles in this unit. Schist and amphibolite are generally weathered and covered by soil; however, white-cream-colored marbles are easy to recognize in the field. The texture of the marbles is usually granular and coarse-grained at lower levels (Figure 2.7), but the granular texture gradually disappears upwards and become pure white massive marbles in the upper levels. Banded texture is also

present in the lower levels. Oxidation typically increases near the E-W faults. When oxidized, marbles are pinkish colored and have hematite veinlets.

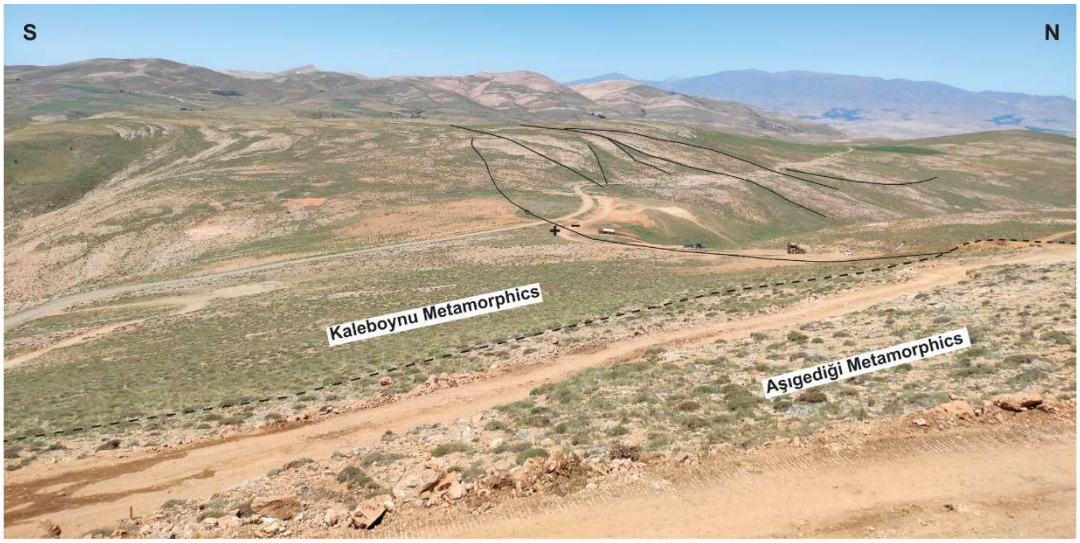

Figure 2.6. General view from Aşılık Tepe Note that the Kaleboynu metamorphics are oxidized along EW faults (looking west)

Figure 2.7 Granular textured marbles from lower Kaleboynu metamorphics (37.933860, 34.837332).

2.1.2 Lower Kaleboynu Schist

Lower Kaleboynu schists is a distinct mappable schist level located forming part of the Kaleboynu Metamorphics. It corresponds to the second schist-dominant layer from the top of the Kaleboynu metamorphics. It is composed of yellowish-brownish to orange-colored quartz-sericite schists but there are also reddish schists due to increased oxidation in some places. Schists are generally cataclastically deformed, brecciated, and clay altered.

2.1.3 Upper Kaleboynu Marble

This unit is composed of white to gray pure massive marbles. Karstification is common along joints and foliation planes. Near the contact of the overlying schist

unit, the texture of the marble is spotty. There are reddish-purple colored oxide veins and veinlets, mostly hematite, filling these joints and foliation planes. Also, discontinuous quartz lenses along foliation planes of the marbles are observed (Figure 2.8).

Figure 2.8. Quartz lens formed along the foliation planes in marble (37.933073, 34.843609).

2.1.4 Upper Kaleboynu Schist

Upper Kaleboynu schist forms the uppermost part of Kaleboynu Metamorphics and starts with an approximately 70-80 m thick reddish-brownish schist unit. In general, the unit consists of sericite-quartz±carbonate±biotite schists but also contains rare marble layers with massive texture. This unit is generally found as deformed

cataclasites and brecciated fragments. In the SW of the main ore zone, foliation of the schists has been obscured due to intense brecciation. The monomictic breccias consist of marble fragments, whereas polymictic breccias are composed of schist and marble fragments. Although oxidation degree is moderate to high in the main mineralization zone, it is especially higher in breccias. Oxidation assemblages are hematite-Mn oxide±goethite and are associated with clay alteration. Calcite veins crosscutting the foliations are very common. In the lateral continuation of these units, a dark gray resistant quartz schist level (Figure 2.23), which can be traced as a key horizon is present showing ductile deformation features. Discontinuous quartz lenses are present within the schists.

2.1.5 Marble-Schist Alternation

Upper Kaleboynu schist unit is overlain by alternating series of marble and schist. Rarely, quartzite, banded marbles and calc-schist levels are also present (Figure 2.9). The marbles are massive while thin schist levels are commonly white to yellow and clay altered.

Figure 2.9. Banded marbles alternating with schists (37.941461, 34.849938).

2.1.6 Beige Marble

Beige to yellowish marbles overlie marble-schist alternation. The marbles are thick bedded and jointed. This unit has been commonly karstified along joints and faults.

2.1.7 White Marble

White to cream-colored marble overlies the beige marbles. The two marbles are separated by a thin amphibolite level. Siderite-ankerite-hematite veins and karstic cavities with reddish hematite fillings within the marbles are rarely observed (Figure 2.18).

Figure 2.10. Hematite mineralization in a karstic cavity and coatings along fractures are very common (37.932669, 34.850327).

2.1.8 Üçkapılı Granite and Dike/Sill Array

Although Üçkapılı Granite covers vast exposure on the surface 5 km to the east of Üçkapılı Village; there are however only a few outcrops present in the study area (Figure 2.3). One of these exposures is located at the west of Aşılık Tepe, where unaltered granite exposure intruded into Lower Kaleboynu metamorphics (Figure 2.11). The other outcrop is located in a drill siteat the SW of the Aşılık Tepe, altered, arenitized, sheared granite outcrop (Figure 2.12). This outcrop is found as a slice bounded by two faults from top and bottom.

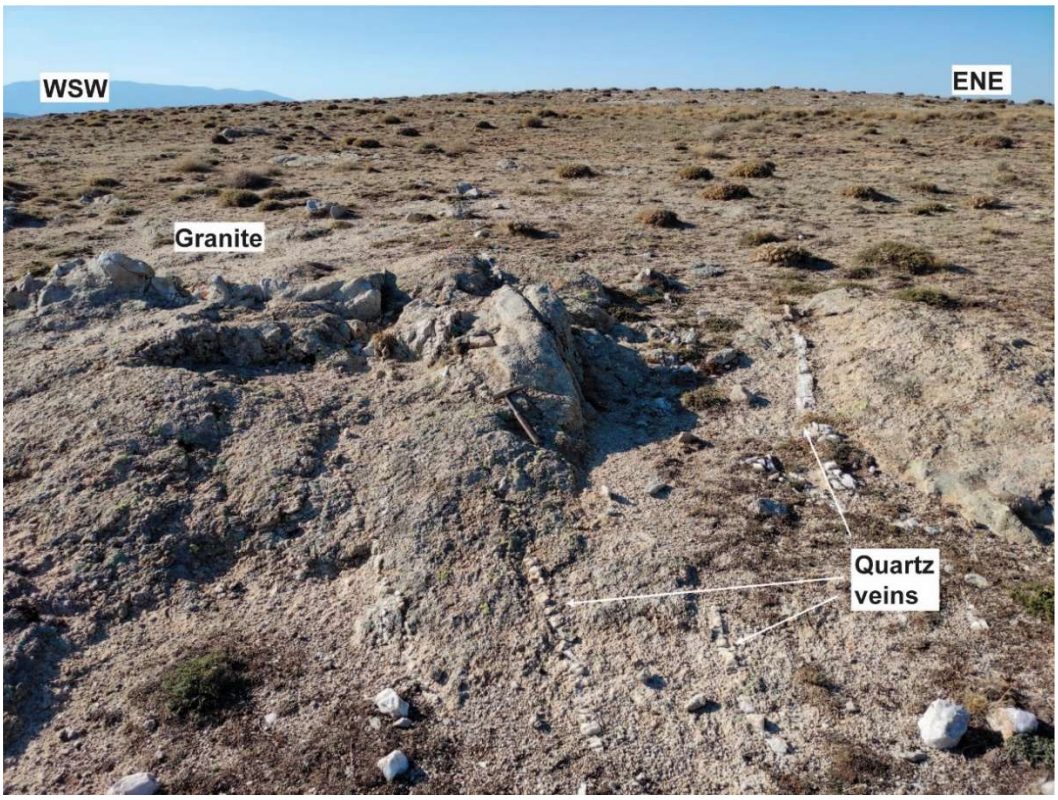

Figure 2.11. Unaltered granite outcrop crosscut by late sub-vertical quartz veins with N20-30W strike (37.935555, 34.834833).

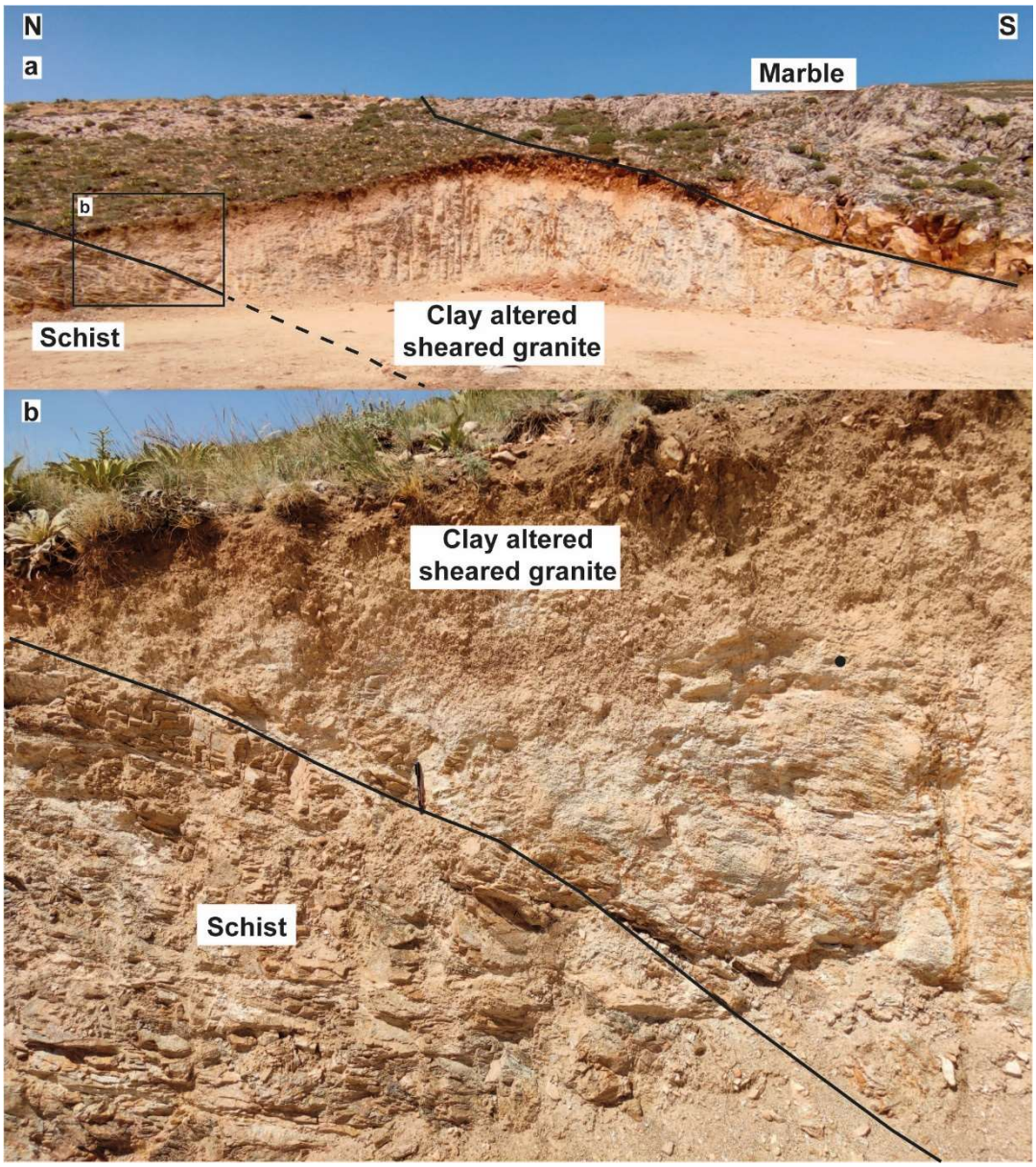

Figure 2.12. Clay-altered and sheared granite slice, bounded by late faults from above and bottom (37.932200, 34.842607).

A dense aplitic and pegmatitic dike and sill array accompany the granitic intrusions. Aplitic and pegmatitic units were distinguished based on their relative crystal sizes in the intrusives. Whereas pegmatitic dikes and sills contain well-developed coarse crystals of quartz, tourmaline and muscovite; aplitic ones have finer crystals. These intrusives are commonly clay altered and are occasionally carbonate altered. Many of the intrusives in the Niğde Massif are concordant with the foliation of

metamorphic rocks or shallowly cross-cut the foliation. In general, oxidation state of the schist are higher, proximal to clay-altered (argillized) dikes. Along their margin, these intrusives are slightly silicified.

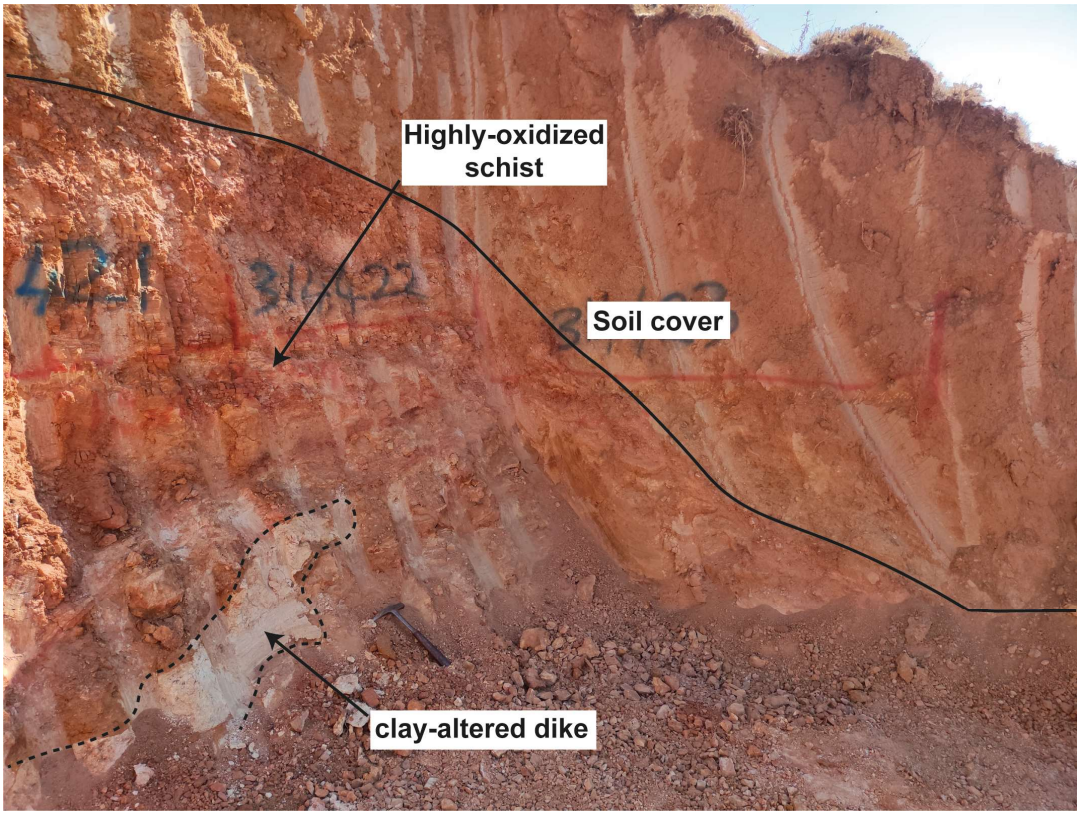

Figure 2.13. Highly-oxidized schists around clay altered dike. The margin of the dike is slightly silicified (37.934857, 34.842581).

2.1.9 Karstic Areas

Karstic areas are observed within marbles. They are mostly found at Aşılık Tepe but are also present in the north of the study area. Karstic areas are best developed along faults and streambeds.

2.2 Mineralized Outcrops

2.2.1 Iron Mineralization in Karstic Breccias

Iron mineralization in the area is commonly represented by hematite ±goethite assemblages and is mostly hosted in the marbles. Iron mineralization is observed along fractures of weakly karstified marbles as hematite veins, or in the matrix of the karstic breccias.

Fracture-fill iron mineralization is hosted in the marbles as veins or veinlets and usually has selvedges (Figure 2.14). Hematite is the dominant mineral in these reddish-purple-colored veins. Hematite veins are structurally occur below karstic breccias.

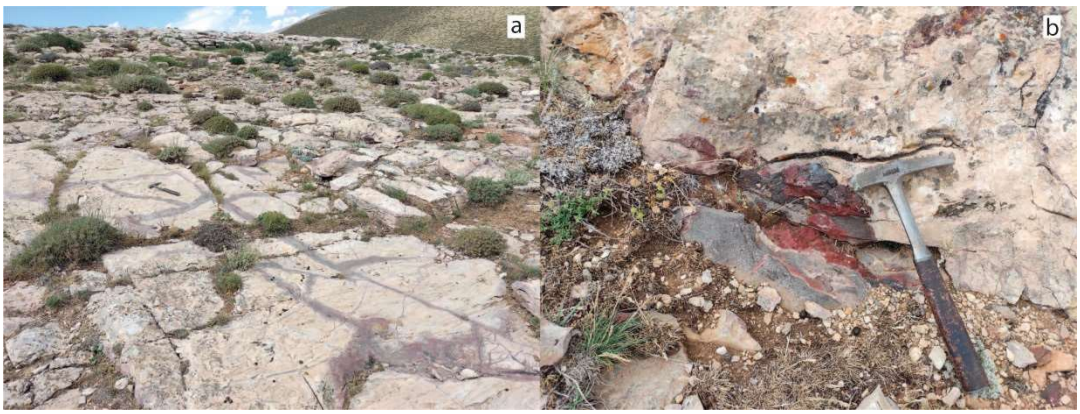

Figure 2.14. (a) General view of hematite veins in the marbles, (b) hematite coating on marble (37.945440, 34.852485).

Karstic breccias are divided into two groups according to their clast assemblages as monomictic and polymictic karstic breccias. They are either grain-supported or matrix-supported according to their karstification degree. Weakly karstified marbles tend to show grain-supported texture whereas strongly karstified marbles show matrix-supported textures (Figure 2.15).

Monomictic karstic breccias (MKBX) contain only marble clasts within a clay-oxide matrix filled in the cavities (Figure 2.15). Sometimes the matrix is composed of pink

to reddish carbonate-hematite assemblage. They are commonly not linked with gold mineralization and are found below polymictic karstic breccias.

Figure 2.15. Field view of: (a) clast-supported monomictic karstic breccias (37.935513, 34.841512), (b) matrix-supported monomictic karstic breccias (37.949560, 34,844354).

Polymictic karstic breccias (PKBX) are composed of both schist and marble clasts. They are commonly hosted in a reddish clay-oxide matrix. Polymictic karstic breccias generally have a higher oxidation state than monomictic karstic breccias. They are located at the schist-marble contacts and along fault zones. Polymictic karstic breccias generally overlie monomictic karstic breccias but are also observed in between the monomictic karstic breccia levels, especially at fault zones (Figure 2.16).

Figure 2.16. MKBX (interval within blue brackets) and PKBX (interval within red brackets) in two different drillholes. (a) PKBX interval is highly oxidized and composed of small fragments of both schist and marble. MKBX intervals consist only marble clasts within less oxidized clayey matrix. (b) PKBX interval has coarse schist clasts with marbles whereas MKBX has marble clasts in a clayey matrix.

2.2.2 Copper Mineralization

Copper mineralization was observed where quartz schists are exposed along a high-angle fault in the north of the study area. Malachite and possible chrysocolla mineralization are observed as stains along fractures in the schist outcrops (Figure 2.17). An old iron mine is present near copper mineralized outcrops.

Figure 2.17. Malachite±chrysocolla stained along the fractures in schist (37.941550, 34.845745).

A similar feature is also observed in the drillholes. In sulfide zones of a drillholes, carbonate-sulfide fracture fill is seen. Chalcopyrite and pyrite are observed in the fracture (Figure 2.18).

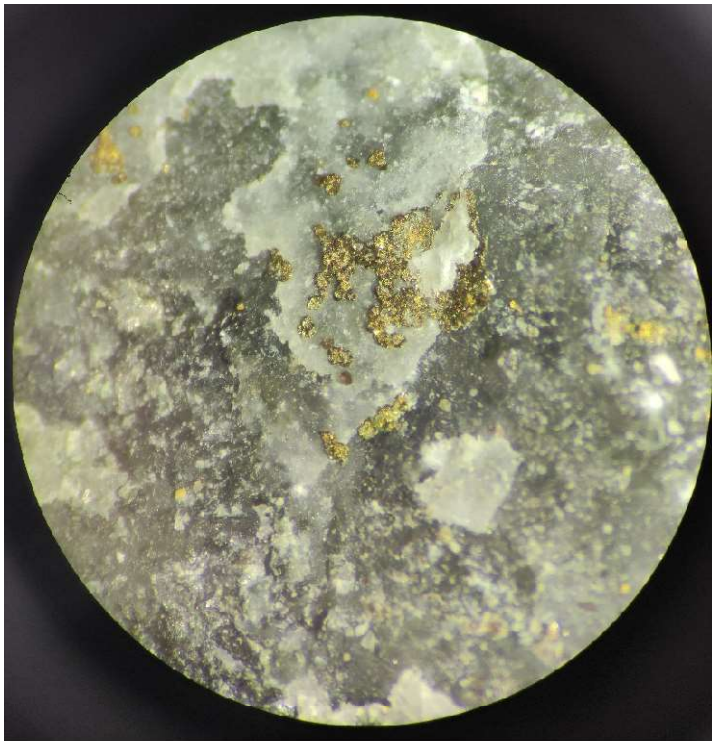

Figure 2.18. Carbonate-sulfide fracture fill. Chalcopyrite at the center and pyrite mineralization at the periphery. x10 magnification with a hand lens (OZD90- 155 m).

In addition, a few azurite-coated marble floats are observed at about 50 m to the south of the main mineralization area; however, no associated in-situ outcrops were identified to this mineralization.

2.2.3 Cataclastic Breccias

Cataclastic breccias are occur in schists as brecciated schist clasts in a gouge-like, comminuted matrix (Figure 2.19). They are often moderate to strongly oxidized. Cataclastic breccias are dominantly found along high-angle faults but also occur along low-angle faults. Generally, increasing oxidation degree of cataclastic breccias is positively correlated with gold grades. In the fault zones, they resemble polymictic karstic breccias; nevertheless, polymictic karstic breccias contain marble clasts, differently.

Figure 2.19. Highly-oxidized cataclastic breccias (intervals within orange brackets) and underlying MKBX (intervals within blue brackets) in a drillhole.

2.2.4 Gossans

Gossans mostly occur within marbles or at the contact of the marbles. They cover relatively small areas with a maximum surface extent of 3m x 3m. This mineralization can be recognized with the change of soil color in the field. Soil color is generally brownish to reddish. Iron ore which is composed of goethite-hematite completely fills karstic cavities in the marble. Therefore, it can be considered as the gossanized parts of the sulfide ore but also contains considerable gold mineralization. In the drillholes, they are encountered within marbles with an oxidation halo (Figure 2.20).

Figure 2.20. Gossans (interval within yellow brackets) in marble (interval within blue brackets).

2.3 Structural Geology

2.3.1 Foliations

The foliation measurements are mostly determined from marble levels since schists are easily weathered and show scarce outcrops. The foliations are sometimes crenulated, especially in schists (Figure 2.21). The general dip is to the SE.

Figure 2.21. Crenulated quartz-sericite schist (37.941599, 34.845614).

2.3.2 Folds

Folds are often hard to distinguish in the surface since the alternating lithologies are very similar and most of the time covered by soil. The foliation measurements over an area might sometimes indicate a fold; however, the crenulated nature of metamorphics or possible higher order folds may be considered. Thus, the main foliation direction should be determined to avoid false interpretations.

A small-scale plunging fold with 300°N trending fold axis is observed in the north of the study area (Figure 2.22). The fold has an antiformal geometry recognized due to oppositely dipping marble beds.

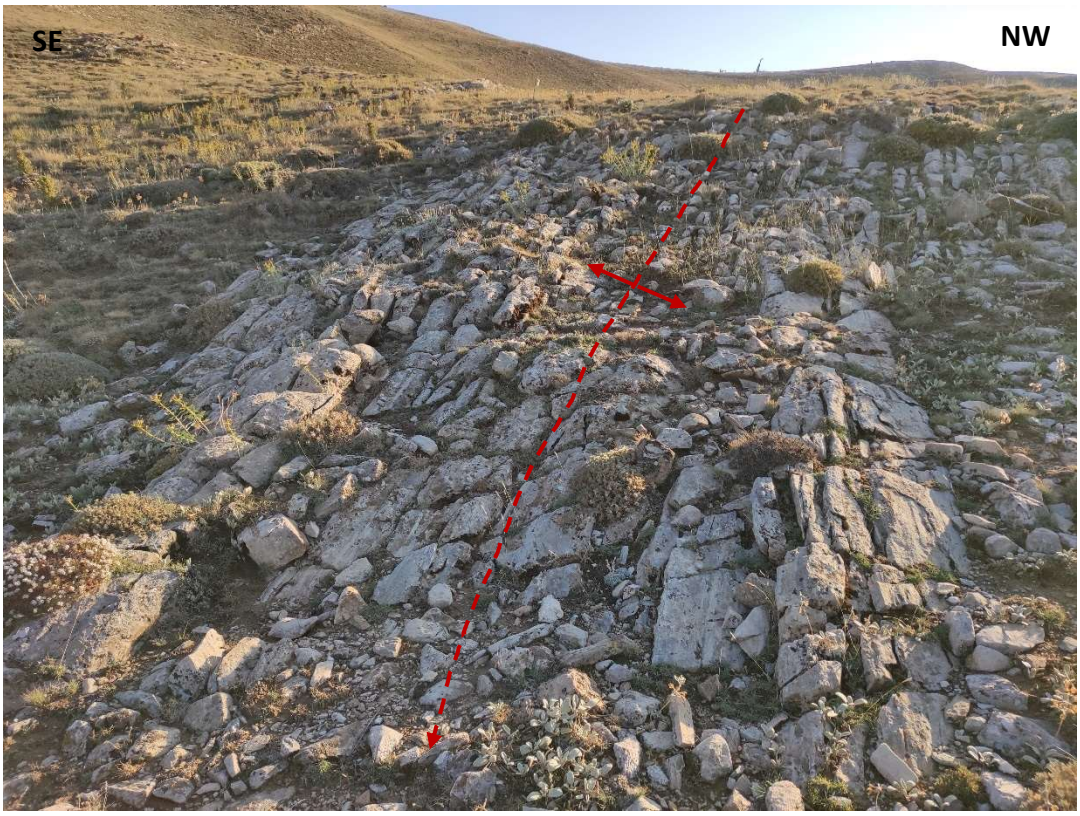

Figure 2.22. An anticline extending along the N60E direction (37.938956, 34.851707).

There is also an antiformal, dome-like structure, at the top of the Aşılık Tepe. The foliation measurements taken from the different sides of the hill show that foliations are radially dipping outwards.

2.3.3 Faults

Faults are interpreted by lineament analysis using satellite imagery. Any lineament with an appreciable off-set of units is drawn as a possible fault on the map. These lineaments are then checked on the ground to test if they can be proven by any fault feature or not. Many lineaments interpreted as possible faults could not be proved the karstification of marbles and limited outcrop exposures of schists on the surface. However, lineaments showing features like fault rocks or planes are classified as faults and indicated with a solid black line on the map (Figure 2.2).

Faults in the study area can be grouped into two different groups according to their dip angles: (i) low-angle faults if the angle between fault and foliation is lower than 30°and (ii) high-angle faults if the angle is between 30-90°.

2.3.3.1 Low-angle Faults

Low-angle faults are often observed in between foliation planes but are also recognized by cross-cutting relationship with the foliation, with dips lower than 30°. Although most structures within these faults are ductile, they are sometimes overprinted by progressive brittle deformational structures.

In some resistant outcrops, layer-parallel shears and associated kinematic sense indicators are observed. In Figure 2.23, both dismembered and stacked quartz lenses form “S fabrics” at the center and the clockwise rotation of a quartz lens at the right implies top to ENE shear sense. In Figure 2.24, C-C’-S fabrics formed in low-angle shear zone within schists show top to SE shear sense.

Figure 2.23. Layer-parallel shears along foliations of quartz schists. Top to the ENE shear sense determined by C-S fabrics (center) or clockwise rotated quartz lens (right) (37.931838, 34.845087).

Figure 2.24. A low-angle shear zone within quartz-sericite schist. C-C'-S structures show top to SE shear senses (37.929276, 34.847344).

Between the foliation planes of schists in some outcrops, slickenlines are observed which shows that more brittle conditions operated and possibly overprinted earlier ductile structures during the exhumation (Figure 2.24 and Figure 2.25).

Figure 2.25. Slickenlines formed at the foliations of schists (37.934516, 34.844556).

2.3.3.2 High-angle Faults

High-angle faults are generally E-W-striking. They are best observed in the west of the study area where faulting caused deformation of the units. Most high-angle faults are brittle structures and show evidence of cataclasis. The best example is observed in the main mineralization area. In Figure 2.26, a cataclastic fault zone with strong oxidation is observed at a drill site. The footwall of the fault has moderate to strong oxidation along foliation planes. Oxidation continues about 4 m into the footwall and then ends abruptly. Also, in the same locality, next to the high-angle fault, there is clay-carbonate altered dike (also slightly silicified) intruding into karstic breccias and schists (Figure 2.26).

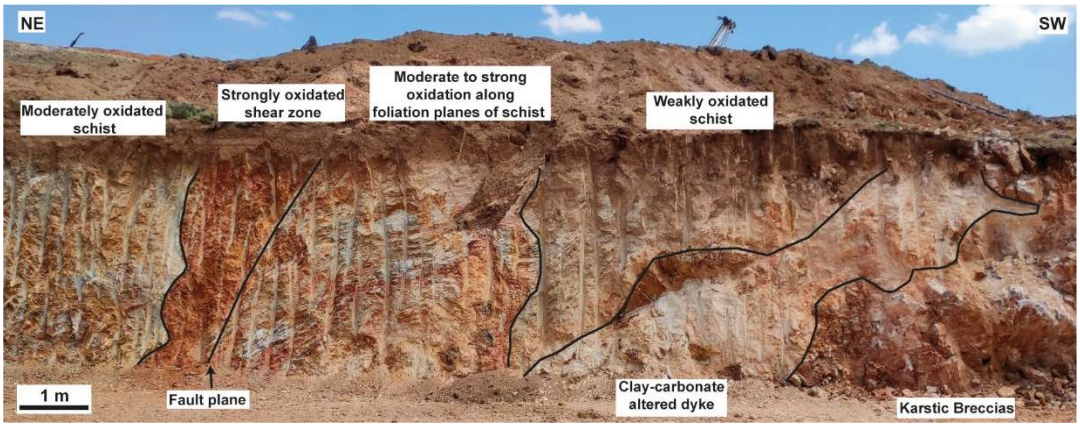

Figure 2.26. Strongly-oxidized high-angle fault, dike, and karstic breccias exposed at a drillhole location. (37.934700, 34.842582).

In another drill site, a fault zone of 60° is present within schists (Figure 2.27). Similarly, the fault zone and adjacent rocks are more oxidized than the distal rocks.

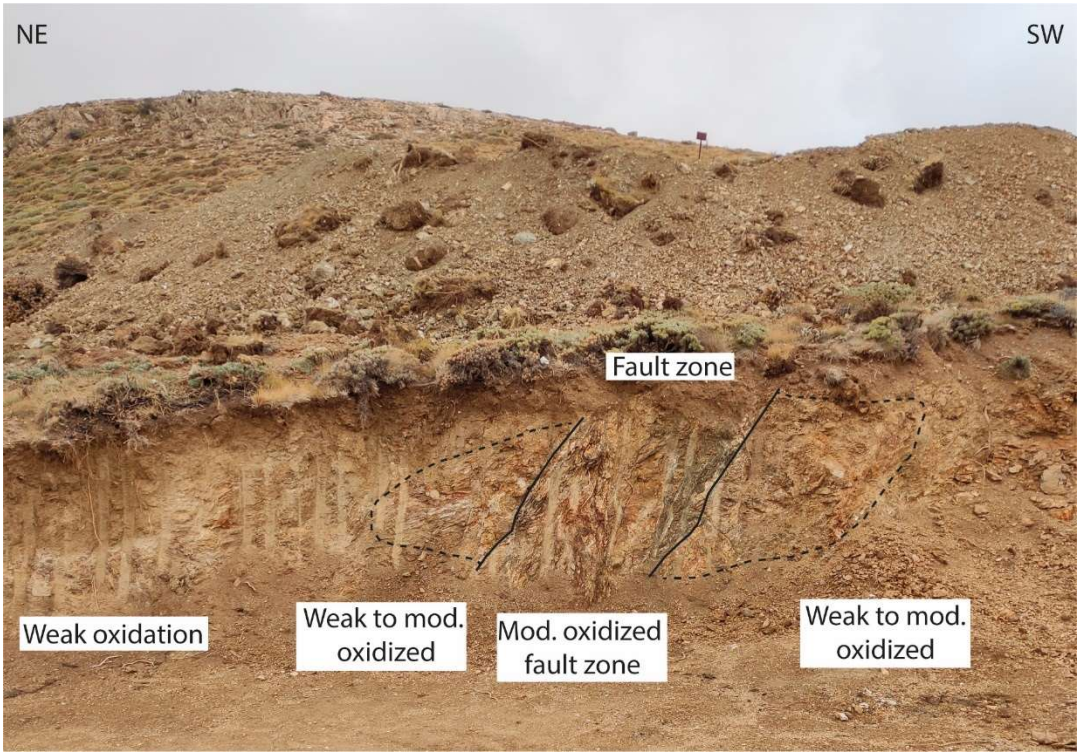

Figure 2.27. Photograph showing a high-angle fault and considerable oxidation in the surrounding rocks. The intensity of oxidation decreases away from the fault plane (37.934696, 34.843232).

In the same location as the old iron mine and copper mineralization, a brittle fault with slickenlines is observed (Figure 2.28). The fault surface is coated with hematite mineralization. Chatter marks from the fault indicate normal movement with a minor dextral component.

Figure 2.28. Slickenlines on hematite-coated fault surface (37.941550, 34.84567).

Lastly, in the west of the study area, a fault with an attitude of N78°W, 45°NE, 30°SE is observed (Figure 2.29). The fault is filled with silica and has slickenlines on silica coating.

Figure 2.29. Fault with silica infill (37.931320, 34.835522).

2.3.4 Veins

In the study area, two types of veins are recognized as carbonate veins and milky quartz veins. Carbonate veins typically occur within high-angle shear zones and as fracture fillings. On the other hand, milky quartz veins are vertical to sub-vertical structures, cross-cutting the foliation with 80-90°, and have a strike of N10°-30°W. Their thicknesses can vary from 1-2 cm to 1-2 m. These veins are also observed in Gökkuyu Tepe, located in the south of the study area.

In Figure 2.30, a vertical quartz vein with goethite coating crosscuts the marbles of the lower Kaleboynu metamorphics. The strike of the vein is measured as N10°W.

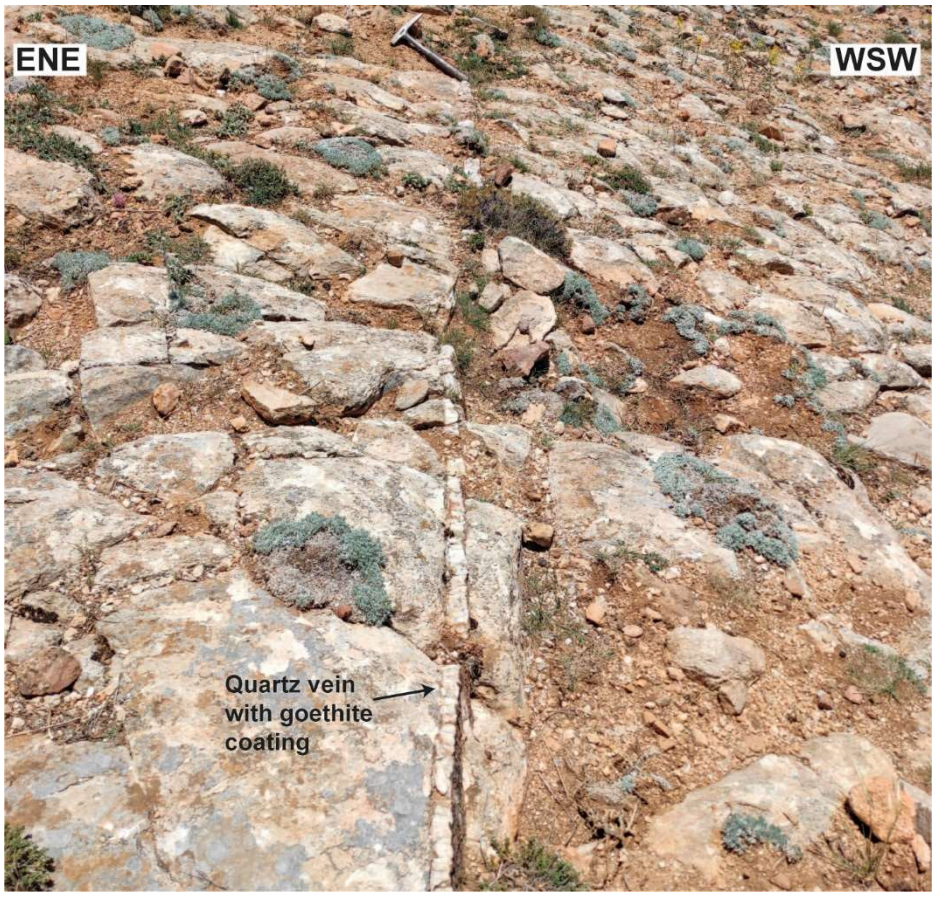

Figure 2.30. Vertical quartz vein with goethite coating, cross-cutting the marbles (37.931584, 34837358).

CHAPTER 3

3D SOLID MODEL OF ÖZYURT GOLD DEPOSIT

Geological models are essential to combine a great number of data collected from the surface, including the geologic map, foliation and faults measurements and drillhole data and to synthesize them into a 3D output to visualize the geology. Lithologic and numerical models are extensively used for decision-making processes for exploration activities and resource estimations.

In this study, an implicit model is created using the Leapfrog Geo software. In an implicit model, geologic surfaces are constructed using an automated radial basis function (RBF). On the other hand, an explicit model is a more traditional method, where one manually creates wireframes to generate surfaces on a CAD-based program. Although it is not entirely possible to eliminate the human effect even in implicit modeling, implicit modeling requires specific inputs and parameters to control the model. Therefore, implicit modeling is more reliable than explicit modeling since it reduces the uncertainty or operational risks caused by the subjectiveness of the modeler.

Within this chapter, modeling procedures are reported stage wisely and the resulting geologic model is evaluated in terms of findings and shortcomings.

3.1 Modeling Procedure

The modeling procedure consists of four different hierarchical stages as shown in Figure 3.1. The first three stages indicated with blue boxes are done by importing preliminary data of topography, surface geology and drillhole data (collar, survey and geology). The stage with yellow boxes means the extraction of data from the geologic map, into a digitized GIS format. The next stage shown with purple boxes

consists of interpretation of drillhole intervals, and faults, acquired by using the geologic map and drillholes, and generation of form interpolant surfaces, acquired by using foliation measurements. Unit boundaries, interpreted fault and unit intervals, and form interpolants are then combined to produce a 3D lithologic model. Also, a quantitative oxidation model based on a rating system out of five is produced. These two models together illustrate the 3D geologic model Özyurt gold deposit.

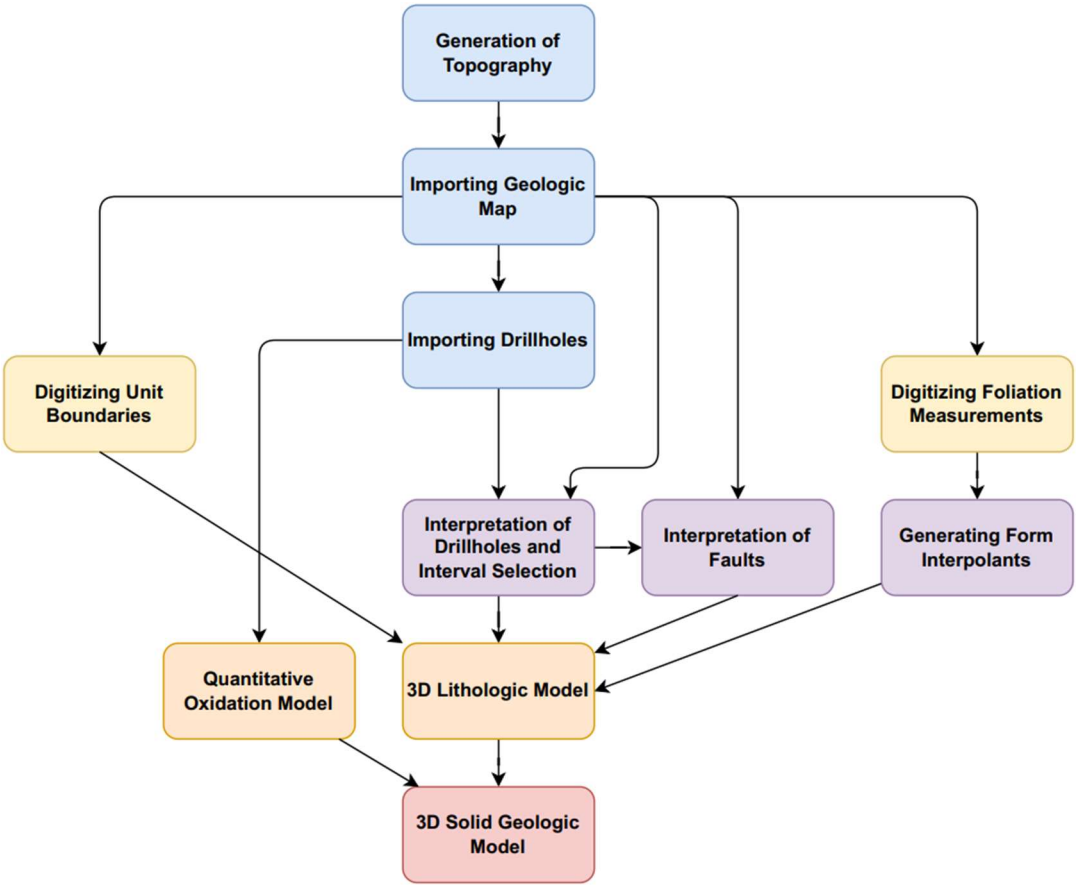

Figure 3.1. Diagram showing modeling procedure.

3.1.1 Generating Topography

The topography of the study area is generated by using spatial point data (Figure 3.2). This data is gathered by a drone survey conducted by ESAN. The gathered data consists of coordinates of each point as in the x, y and z axes. The data sampling is denser in the center of the study area where most of the drillholes are located. The

point data is used to generate a mesh surface and then used as a topography for the project (Figure 3.3).

For the project, the coordinate system is chosen as UTM 36N and the reference datum is selected as ED50 to be in accordance with the drillhole data.

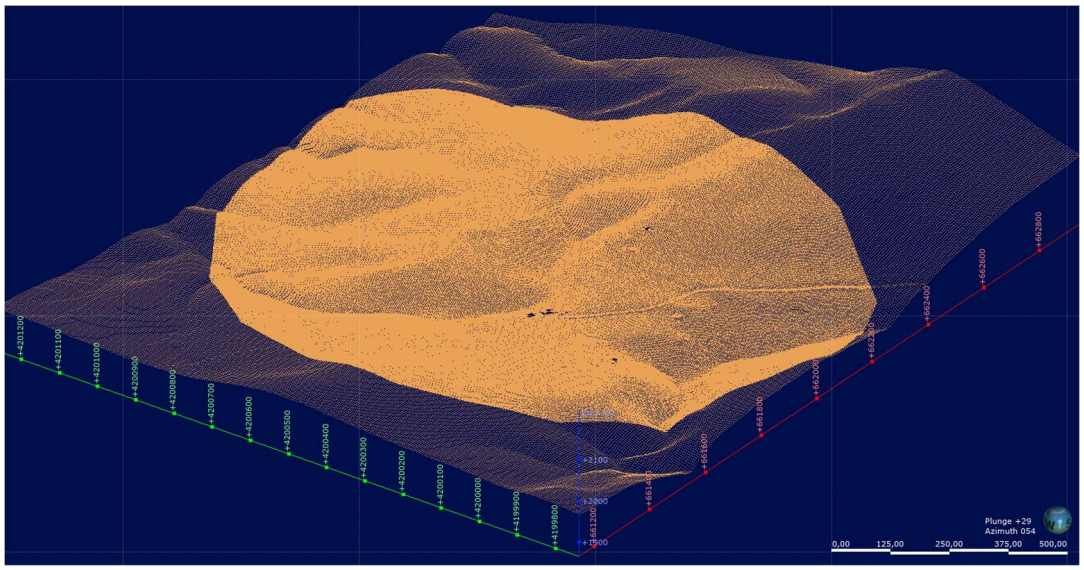

Figure 3.2. Coordinate point data of the study area.

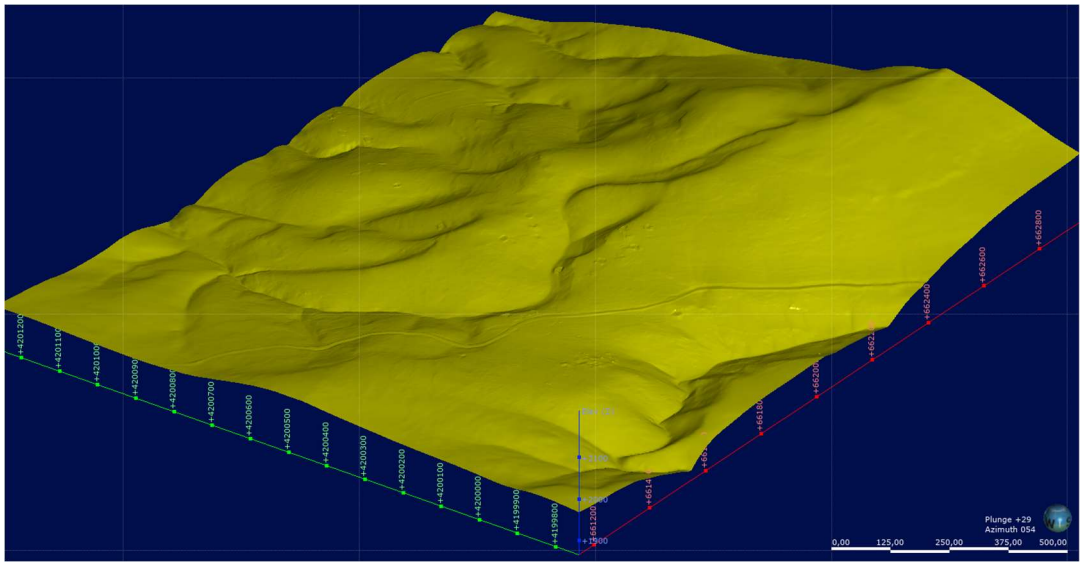

Figure 3.3. Topography generated from the point data shown in Figure 3.2.

3.1.2 Importing Geologic Map and Digitizing GIS Features

The geologic map produced from the field studies is imported to the Leapfrog Geo. The foliation measurements and unit boundaries are digitized as planar structural data and GIS line data (Figure 3.4).

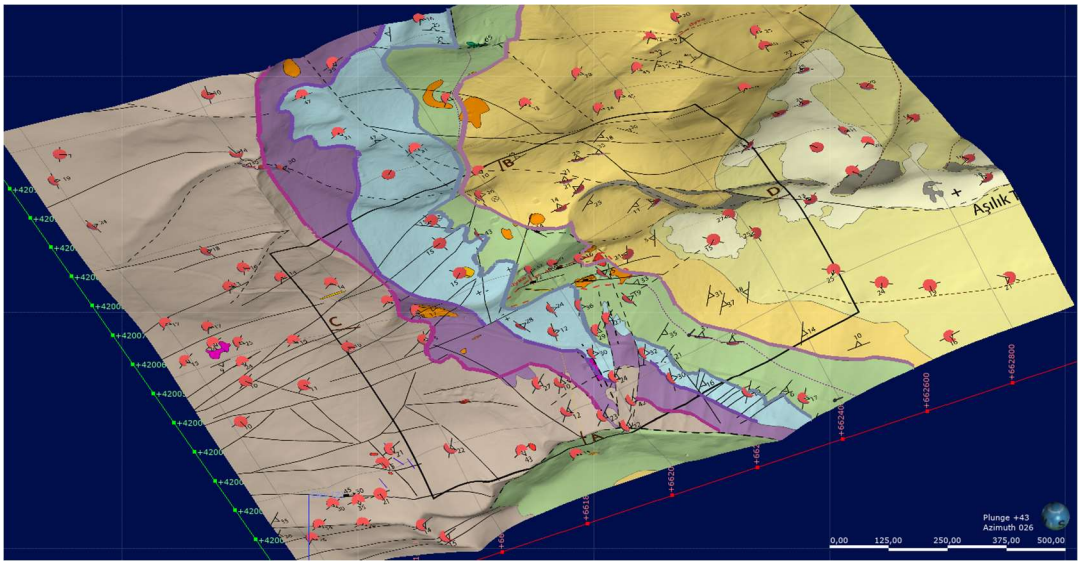

Figure 3.4. The geologic map with digitized unit boundaries and foliation measurements are shown with disks.

3.1.3 Importing Drillholes

The drillhole data includes collar, survey, and geology files. The collar data shows the location of a drillhole on the surface. The survey data was acquired by the measurement of dip and azimuth values in certain depths and depicts the traces of drillholes in the subsurface. The geology data consists of any geologic data including lithology, alteration, oxidation state and intensity and definition interpreted by the geologist as intervals.

3.1.4 Form Interpolants and Structural Modeling

A structural model was obtained by generating form interpolants by using digitized foliation measurement in Leapfrog Geo (Figure 3.5). Form interpolants are reference surfaces with off-sets generated by the RBF function to visualize structural trends in the study area. In this stage, foliation measurements are not attained to any units but evaluated as a bulk.

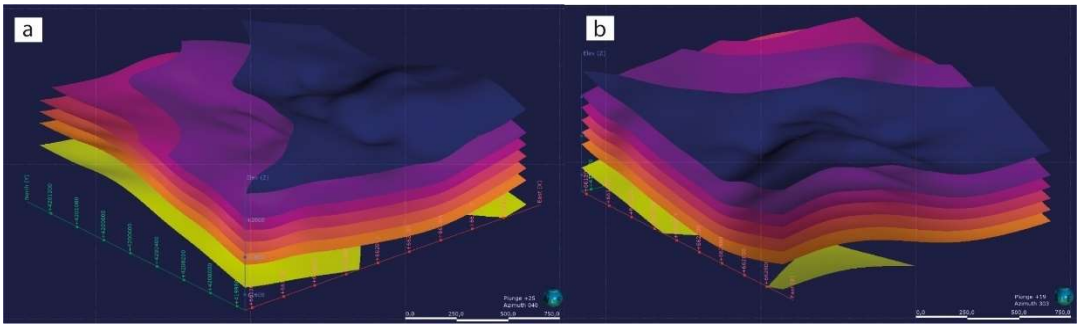

Figure 3.5. Form interpolant surfaces, (a) looking NE, (b) looking NW

3.1.5 Interpretation of Drillholes and Interval Selection Procedure

The lithologies in drillholes are logged as the following codes as indicated in Table 3.1. For modeling purposes, the lithologies are grouped to be in accordance with the geologic map.

Table 3.1. Lithology codes and simplified lithology groups used for modeling.

Code	Description	Code	Group
AMPSCH	Amphibole schist	TAL	Overburden
APL	Aplite	OVB	
CATBX	Cataclastic Breccia	SCV	
CSST	Calc-Schist	SMRB	Marble
FIR	Felsic Intrusive	MRB	
IFM	Fe-oxides	MKBX	
INT	Intrusion	PKBX	
MARBND	Banded marble	MARBX	
MARBX	Brecciated marble	MARBND	
METAGM	Meta-granite	SCH	Schist
MKBX	Monomictic karstic breccia	CATBX	
MRB	Marble	CSST	
NOC	No core; Gallery or karstic cavities	AMPSCH	
OVB	Overburden	PGM	Dike
PGM	Pegmatite	APL	
PKBX	Polymictic karstic breccia	INT	Granite
QTV	Quartz vein	FIR	
QZT	Quartzite	METAGM	
SCH	Schist	QZT	Quartzite
SMRB	Spotty Marble	IFM	Fe-oxides
TAL	Talus	QTV	Omitted
SCV	Sedimentary Cover	NOC	

Since the dominant lithologies in the study area are mostly schists and marbles, the contacts of these two lithologies are carefully examined. The main contacts of marble dominant and schist-dominant intervals are accepted as the unit boundaries.

Although the units are similarly interpreted in accordance with the units of the geologic map (Figure 3.6 and Figure 3.7), the Aşıgediği metamorphics are grouped into a single unit since marble-schist alternation, beige and white marble sub-units cannot be identified clearly in drillholes.

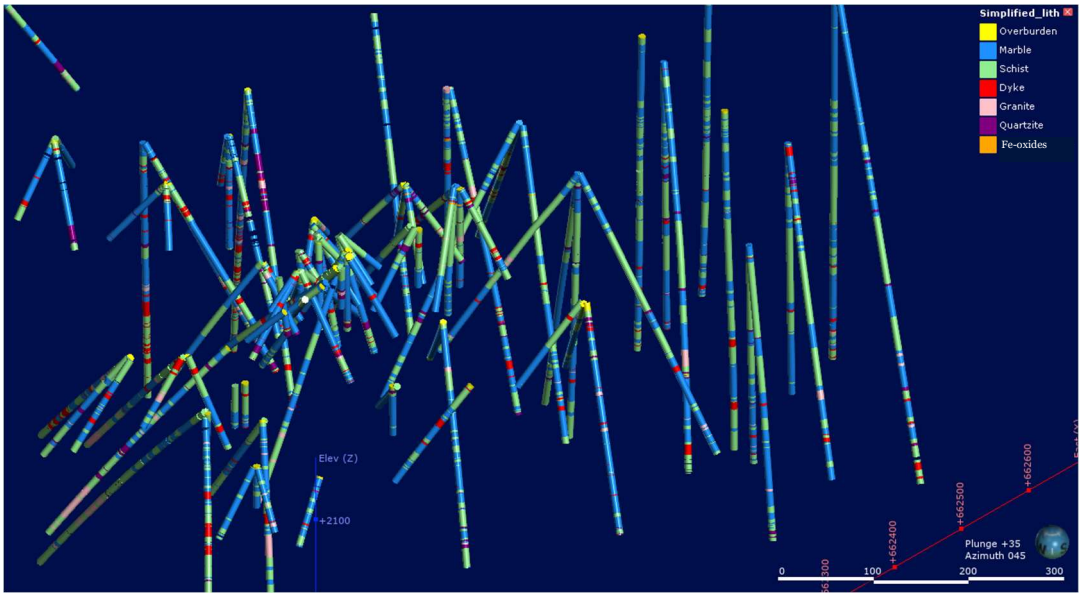

Figure 3.6. Drillholes with simplified lithologies (looking NE).

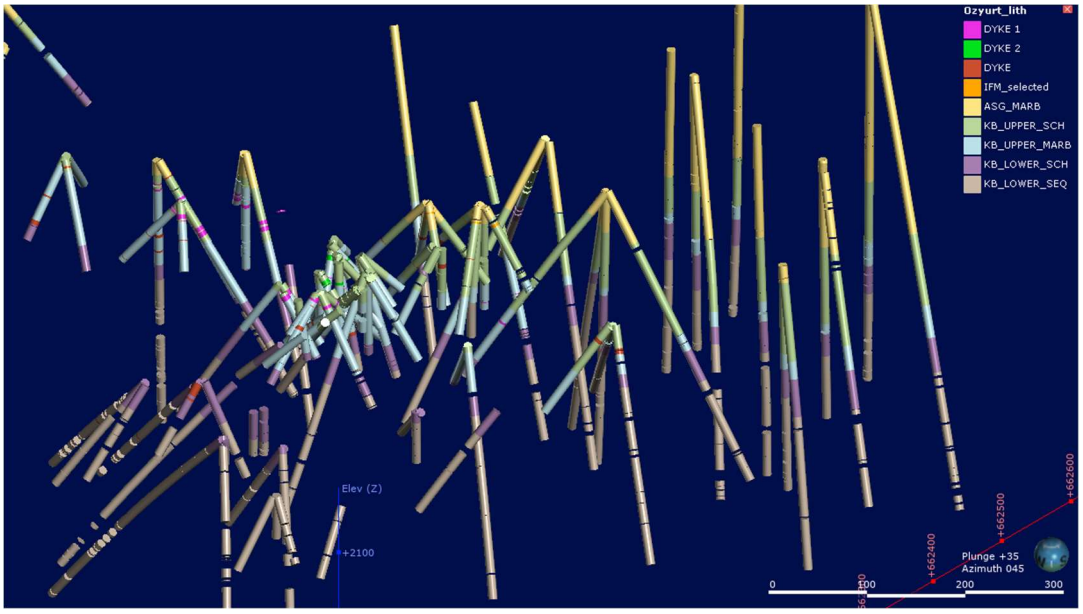

Figure 3.7. Interpreted drillholes in accordance with the units in the geologic map (looking NE).

Aplite and pegmatite intervals are often hard to distinguish when the deformation and alteration are strong. Therefore, they are merged into dike group. Although dike intervals show scattered distribution within drillholes, possible continuous planar intrusives are subgrouped as “Dike_1” and “Dike_2” after being checked from

drillhole photographs whether the lithologies show resemblance with each other (Figure 3.8). Both dikes crosscut the units with a low angle.

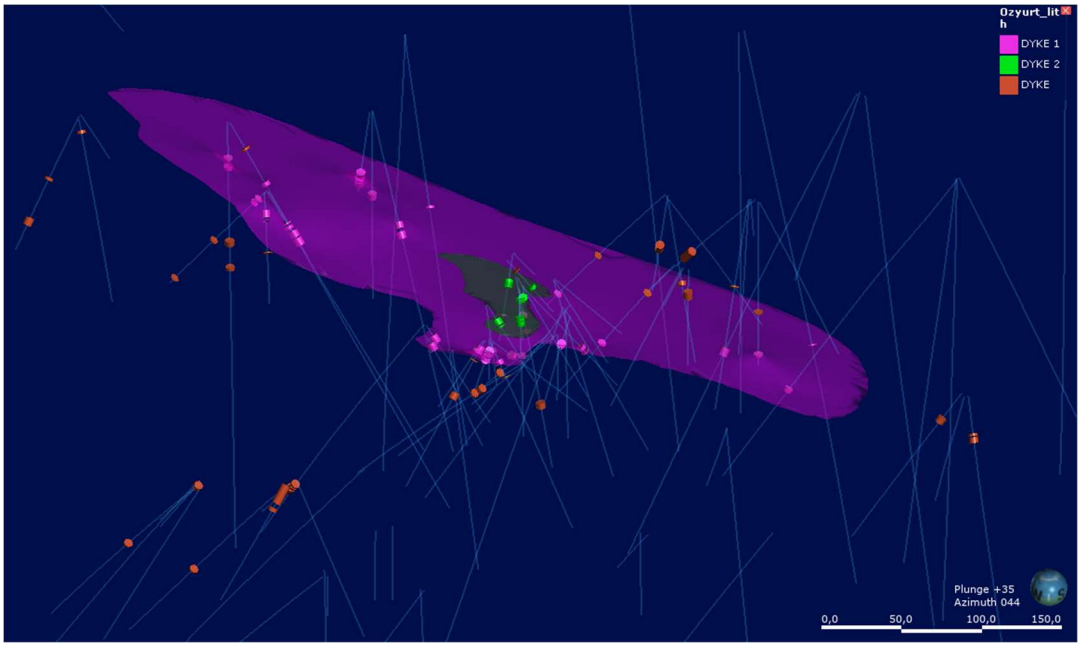

Figure 3.8. Distribution of dike intervals. Dike_1 and Dike_2 as two parallel structures on different levels (looking NE).

Granite intervals are similarly scattered in the drillholes, but thicker intervals are observed in the west of the study area (Figure 3.9).

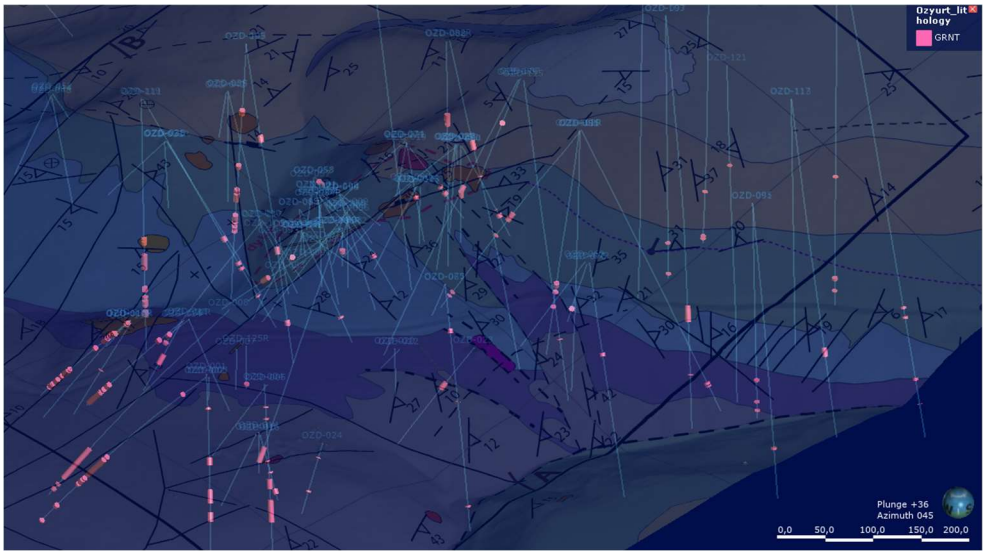

Figure 3.9. Granite intervals in the drillholes (looking NE).

Quartzites in the drillholes are generally observed as discontinuous and scattered intervals. They are often located in schist dominant units and alternate with the schists (Figure 3.10). Schists are generally metamorphosed from mudstone, whereas quartzite is from sandstones. Sandstones may be present as lenses in mudstones as in many clastic stratigraphic environments. Therefore, quartzites are included in schist units and regarded as a metaclastic unit for modeling purposes.

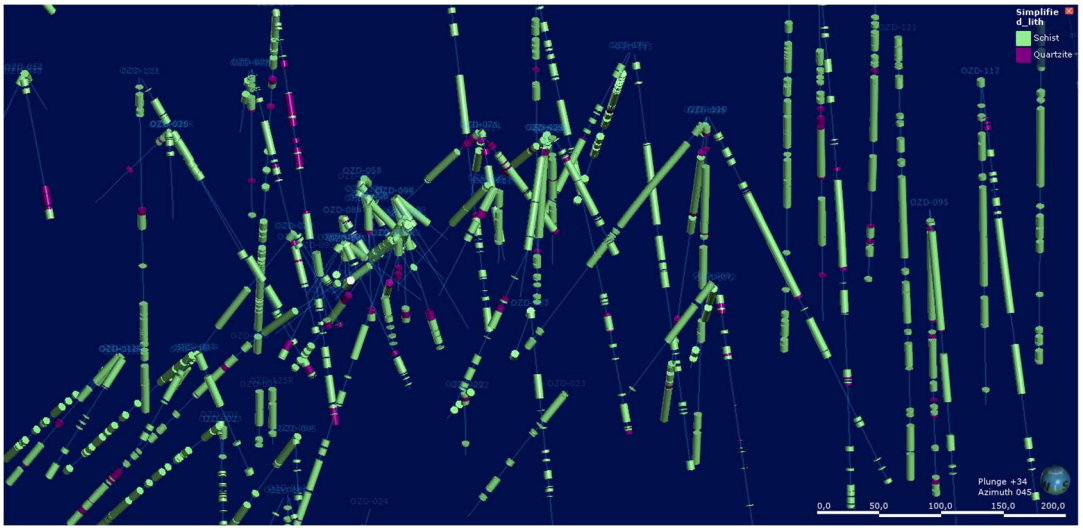

Figure 3.10. Quartzite and schists intervals in drillholes (looking NE).

The Fe-oxides (IFM) is located within the marbles, close to the schist marble contacts (Figure 3.11). They are rarely observed both in the drillholes and on the field. In the east of the main mineralization area, a discontinuous planar IFM distribution is observed.

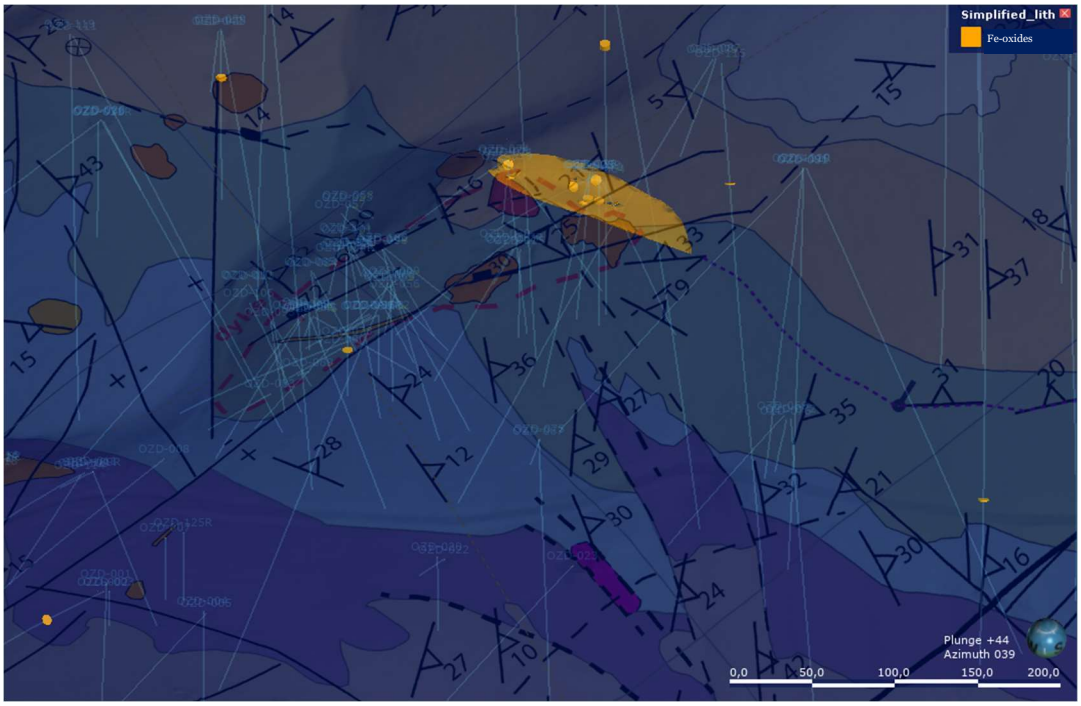

Figure 3.11. Fe-oxides (IFM) group intervals in the drillholes. A discontinuous planar distribution can be observed in the east of the main mineralization area (looking NE).

The overburden group is included in the other units since they do not have any importance related to the mineralization and they are mostly weathering products. Similarly, no core and quartz vein intervals are omitted and included in the other units.

3.1.6 Interpretation of Faults

Most faults in the study area show cataclastic deformation and fault planes are commonly rich in Fe-oxides and clays.as stated in the Chapter 2. The faults in the main mineralization area are prominent since they are related with gold mineralization. Therefore, the geometries of the faults are interpreted by using their surface exposures on the map and by the fault rocks encountered in drillholes which cross-cut these faults (Figure 3.12).

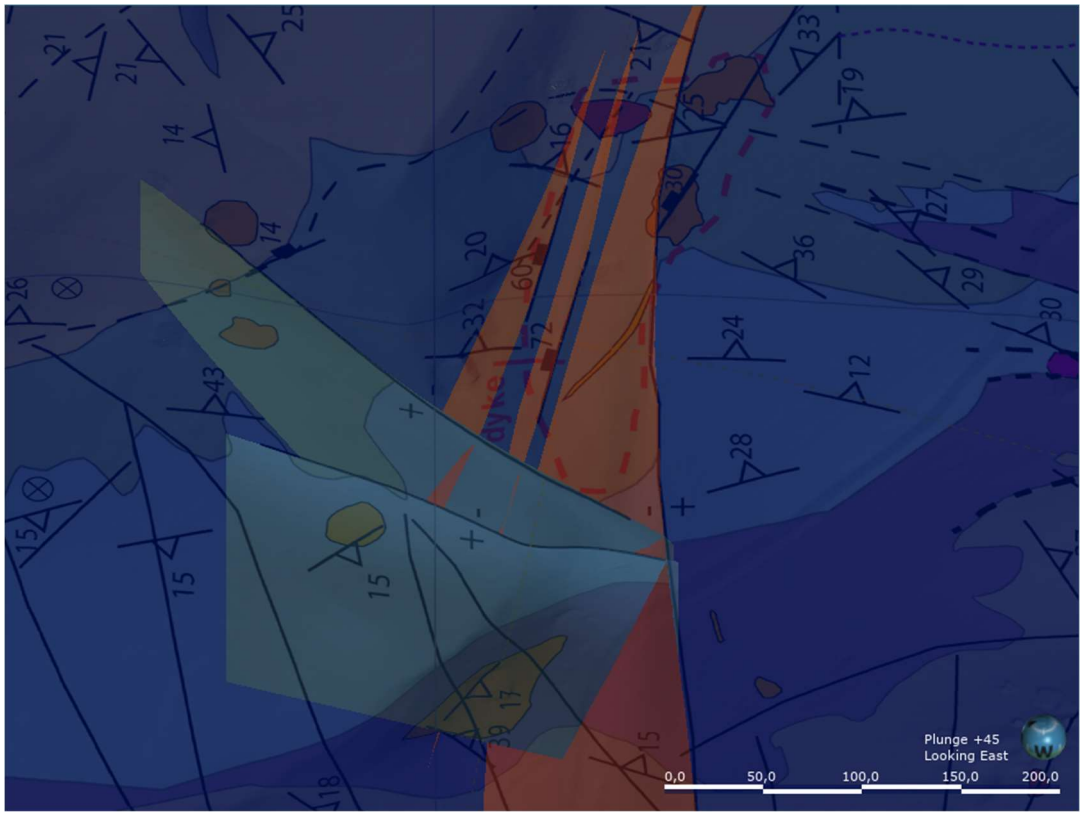

Figure 3.12. General view of the faults in the main mineralization area. Red surfaces indicate hanging wall and blue surfaces indicate footwall (looking east).

For instance, the fault in the mineralization area with 72° dip is shown in Figure 3.13. The fault is drawn by a polyline on the surface. The subsurface continuation of the fault is determined by the fault intercepts shown with disks. The fault intercepts are determined by the presence of the fault rocks with high oxidation within the expected fault continuance intervals of the drillholes. The cataclastic breccias and underlying karstic breccias shown in Figure 2.19 represent a fault intercept interval that crosscuts this fault. Polyline and fault intercept disks together form the fault planes and show the subsurface continuation of these structures.

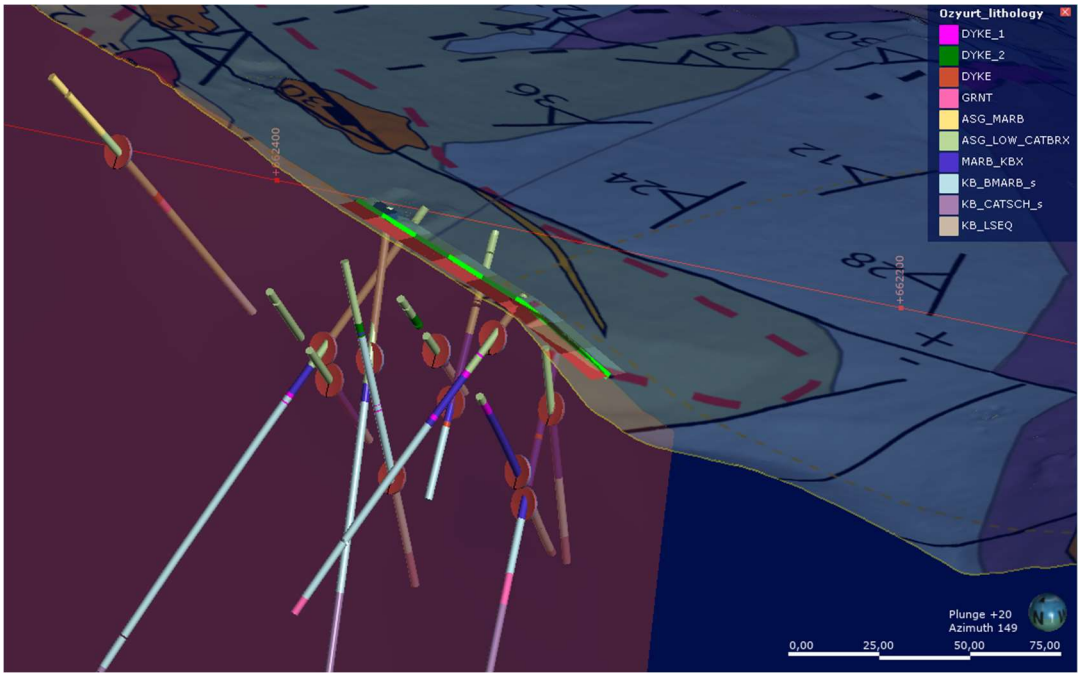

Figure 3.13. Fault interpretation elements. Polyline on the surface, fault intercept disks, and related drillholes (looking SE).

3.1.7 Construction of the 3D Lithologic Model

Building a 3D lithologic model is an iterative process of integrating the available data and interpreted findings within a geological framework obtained in the field. Therefore, the consistency and reliability of a model highly depend on the data quality and the insights of the field geologist.

The modeling is started by adopting the units of the geologic map of the area. The lithologies are grouped and then interpreted as the units of the geologic map after being checked from drillhole photographs and collar locations (Figure 3.14).

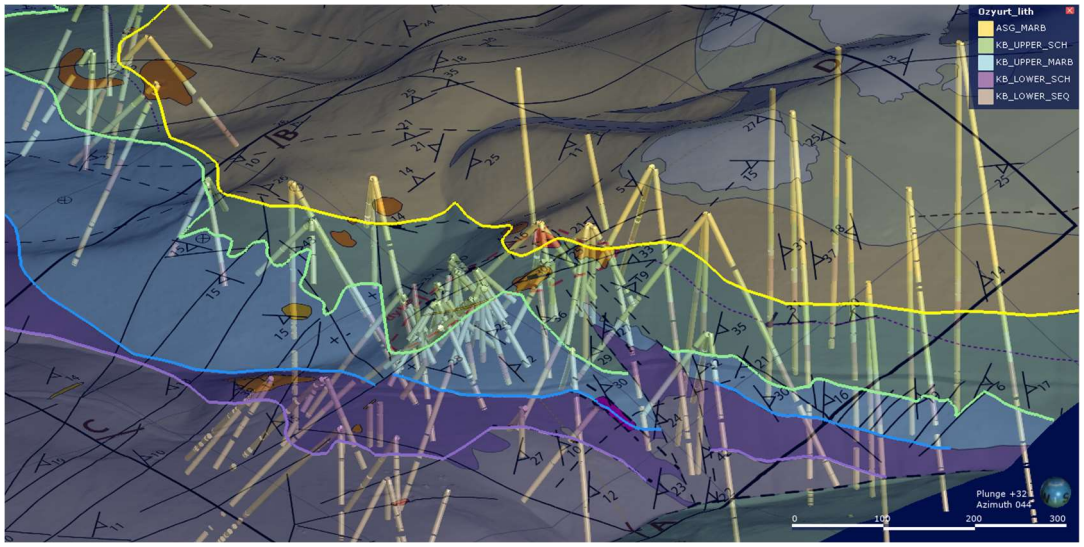

Figure 3.14. Interpreted drillholes in accordance with the geologic map (looking NE).

Leapfrog Geo requires contacting units to define surfaces. For modeling, the metamorphic rocks are considered as stratigraphic units since they were likely derived from stratified sedimentary protoliths. Also, to reflect the structural trends in the study area, reference surfaces from the form interpolants are used. To obtain this configuration, “Lithologic Model>Surface Chronology>New Deposit>From Offset Surface” directory is followed to add new units.

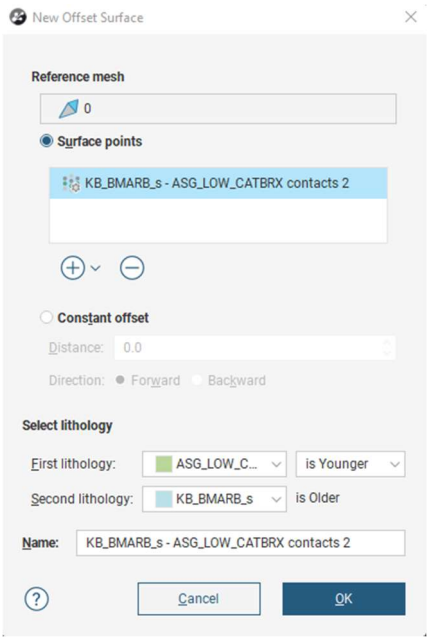

Figure 3.15. New offset surface menu showing the selection of reference mesh and selected surface points.

As shown in Figure 3.15, by this menu, both reference form interpolant mesh and contact points of the units are accounted to create a boundary surface between two units (Figure 3.16).

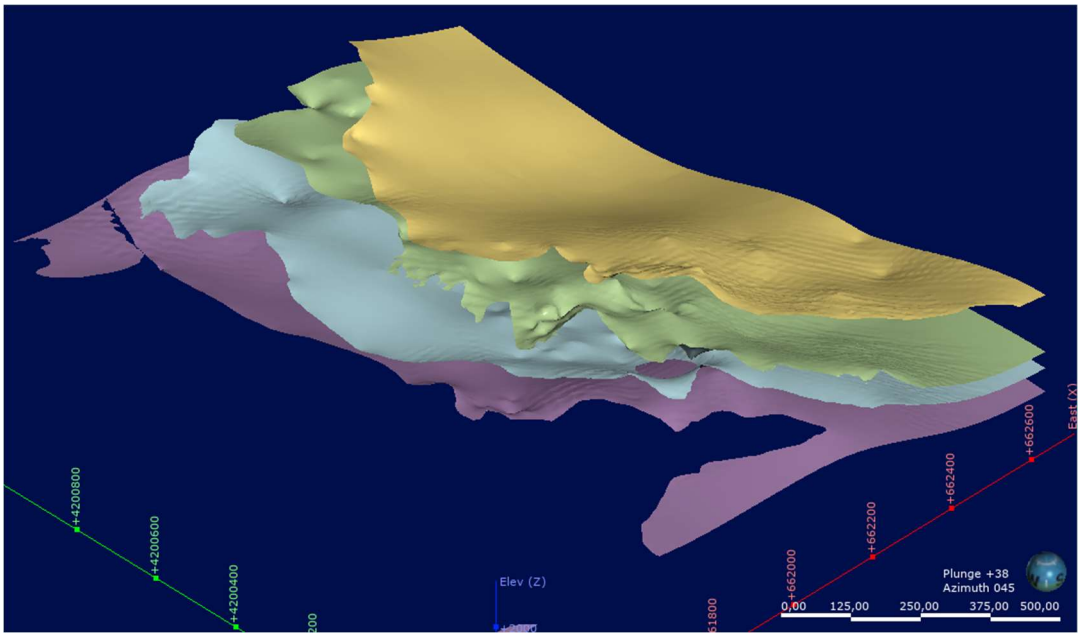

Figure 3.16. The boundary surfaces of the units.

Dike_1, Dike_2 and IFM_selected units were depicted as pinch-out veins in the interpretation stage. These units are also added to the model. From the surface chronology option, units are selected according to their chronological order and activated for the generation of a preliminary model.

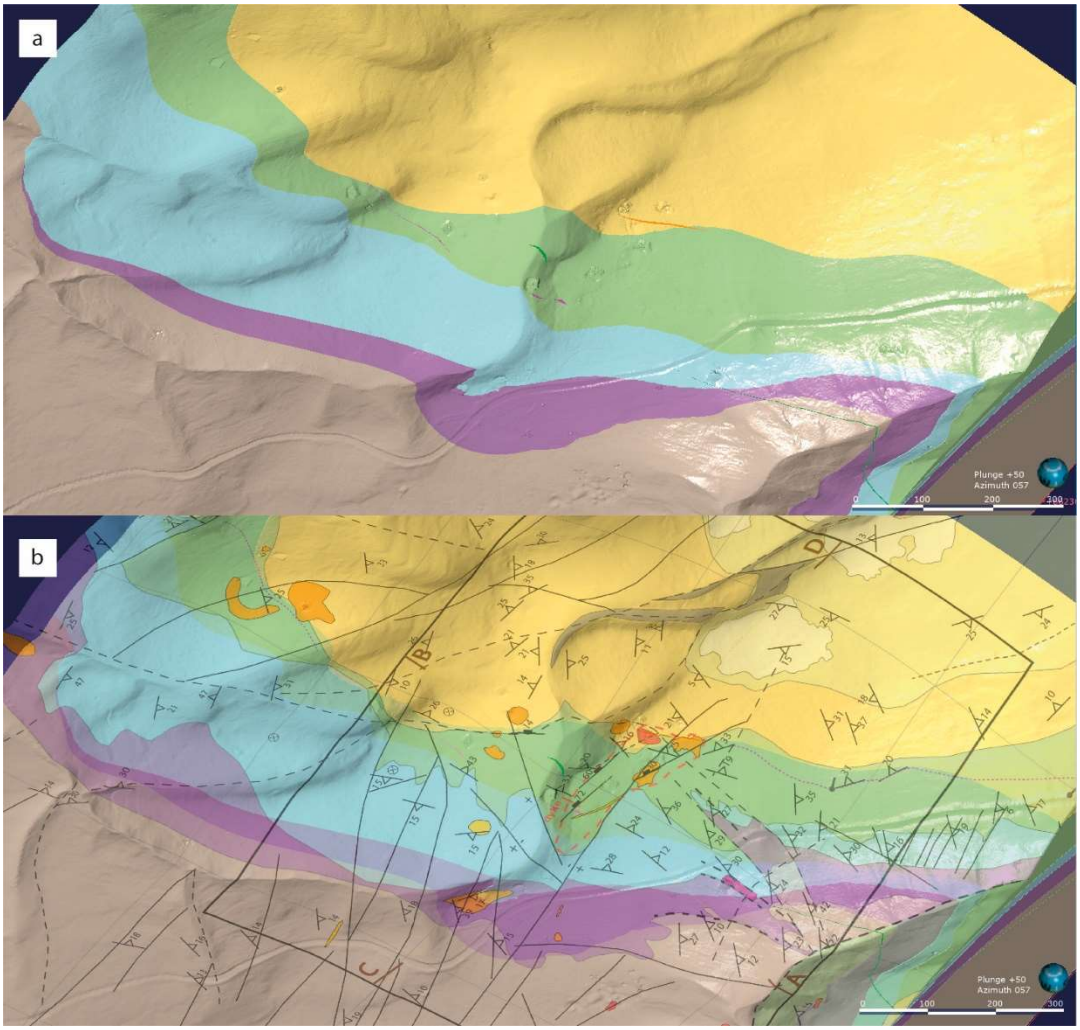

Figure 3.17. (a) The preliminary model formed accounting form interpolants and unit contacts, (b) resemblance of the preliminary model with geologic map (looking NE).

The preliminary model (Figure 3.17) shows similar boundaries and outcrop areas to the geologic map. The digitized unit boundaries determined on the field are also added as GIS vector data to modify the boundary surfaces. In Figure 3.18, the geologic model is highly matching the geologic map after boundaries are added.

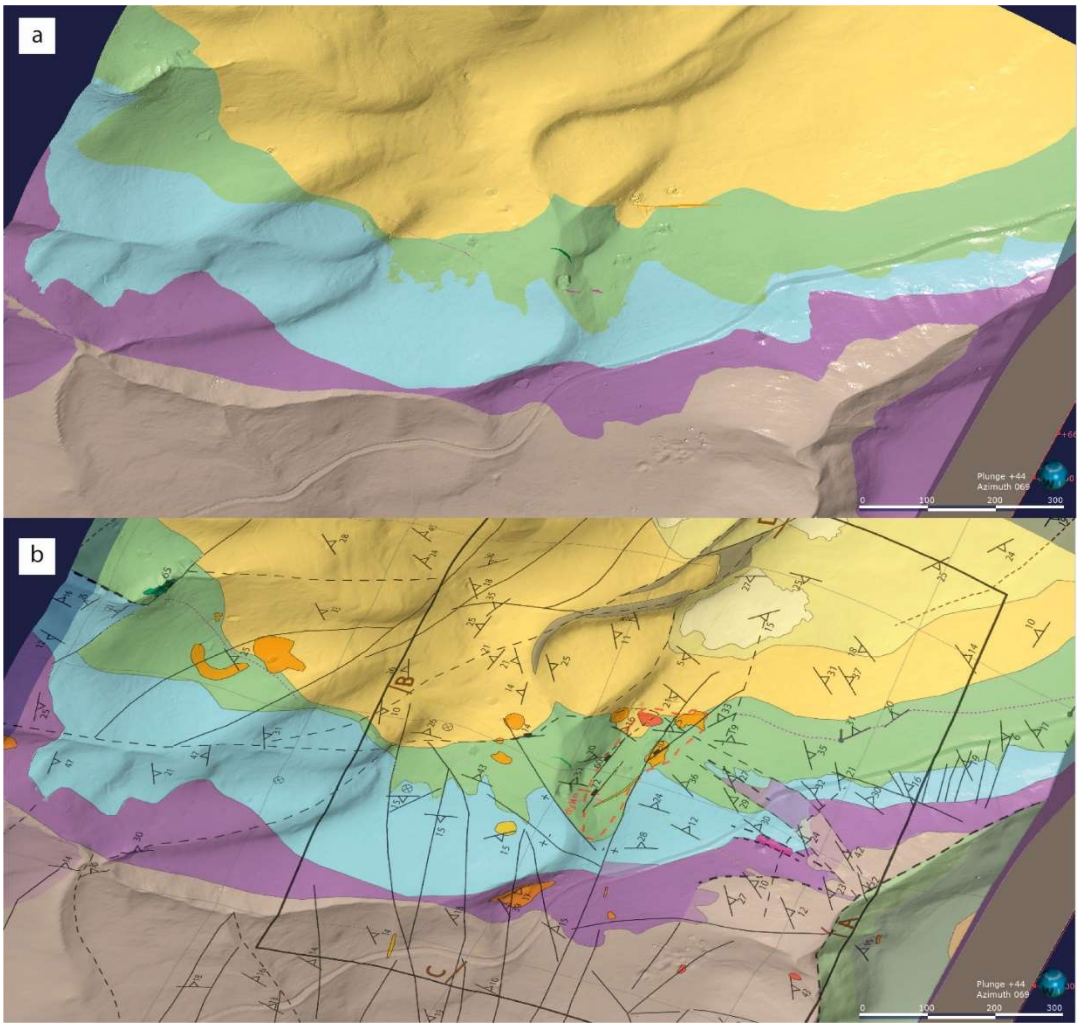

Figure 3.18. (a) Model with modified boundaries, (b) resemblance of the modified model with geologic map (looking NE).

The resulting lithologic model with drillholes is shown in Figure 3.19. Each assigned interval of drillholes is contained within the relevant unit's output volume in the model.

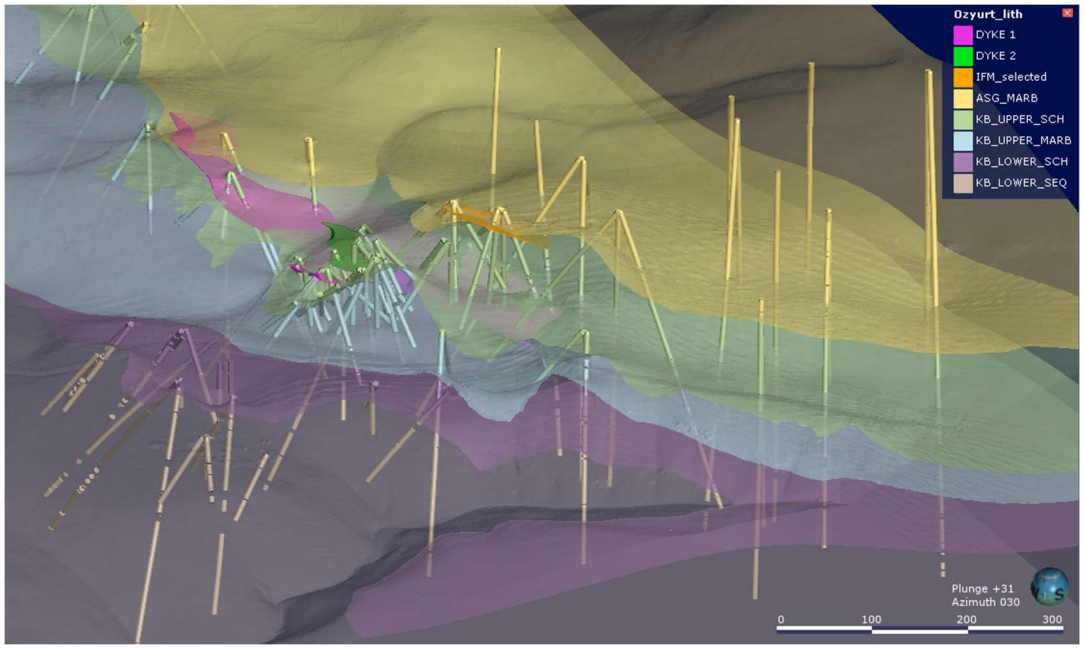

Figure 3.19. General view of resulting lithologic model with drillholes (looking NE).

A closer view of the main mineralization area shows the close relationship between faults and dikes (Figure 3.20). Dike_1 (magenta) and dike_2 (green) crosscut the faults in the main mineralization area. The boundary of KB_UPPER_MARB (blue) and KB_UPPER_SCH (light green) units is disrupted due to E-W-striking faults in the north of the main mineralization area.

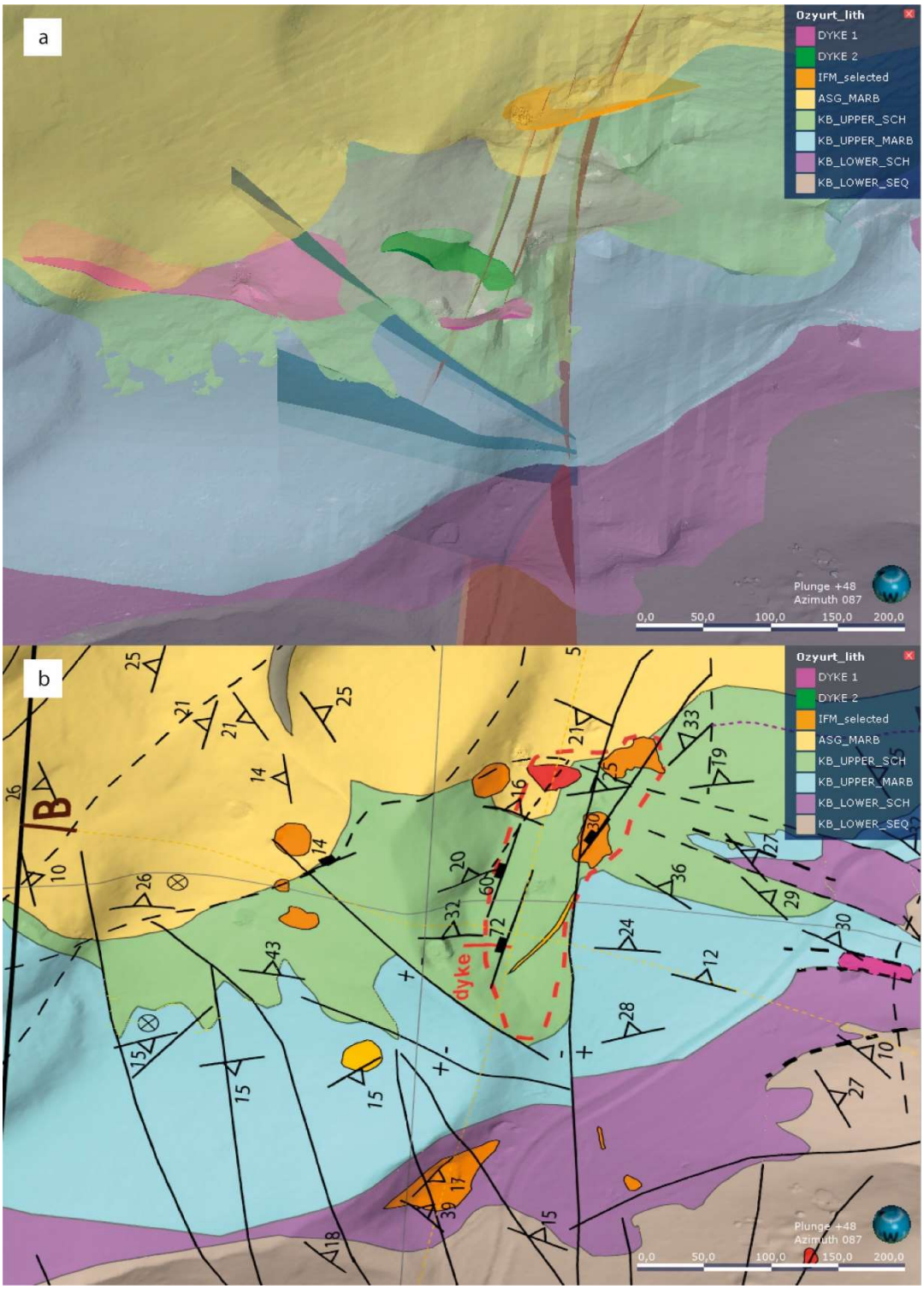

Figure 3.20. Close-up view of the mineralization area, (a) from the resulting lithologic model, (b) from the geologic map (looking east).

3.1.8 Quantitative Oxidation Model

A quantitative oxidation model is generated by using the oxidation ratings attained by ESAN geologists in drill logs. Oxidation ratings are selected from zero to five, where a rating of 0 indicates intervals with no visible weathering and oxidation (i.e., sulfides are fresh, if any) and a rating of 5 indicates intervals that are strongly weathered and oxidized (all sulfides are weathered). Considering the oxide gold mineralization is correlated with oxidation, especially in the main mineralization area, the oxidation model roughly illustrates the higher-grade oxide gold model. Since the gold is located in the schists and is enriched in shear zones a structural trend is created for this model.

The structural trend used for the oxidation model accounts for the effects of faults and regional geologic trends of the units. This is obtained by blending option, where each element is rated with strength in the selected range.

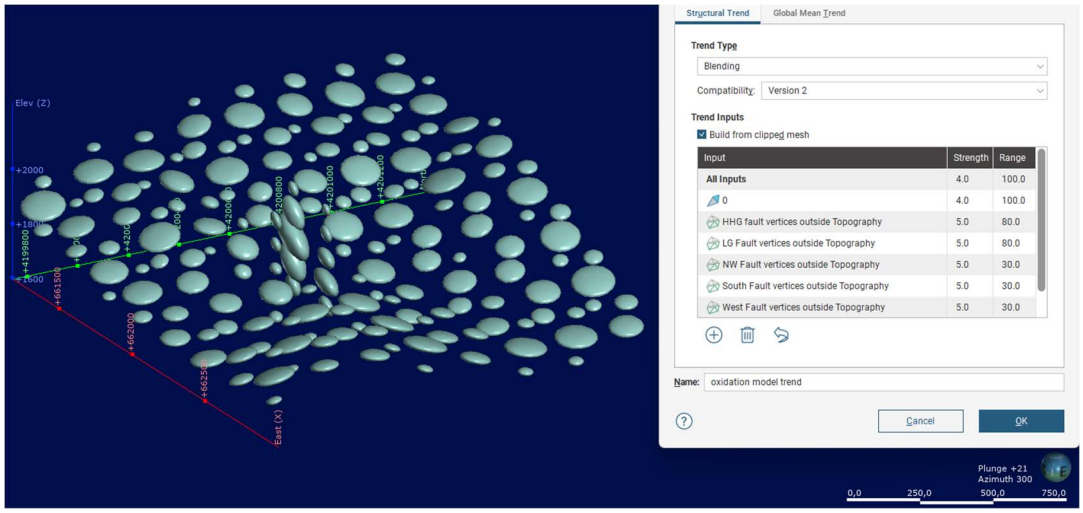

Figure 3.21. The blending structural trend used for the oxidation model and selected strength and range values of each element (looking NW).

The oxidation model is generated after implementing the structural trend and oxidation ratings (Figure 3.21). In Figure 3.22, the correlation between oxidation and gold mineralization can be observed. However, it should be noted that the size of the

oxidation shells in the model does not necessarily reflect the amount of mineralization.

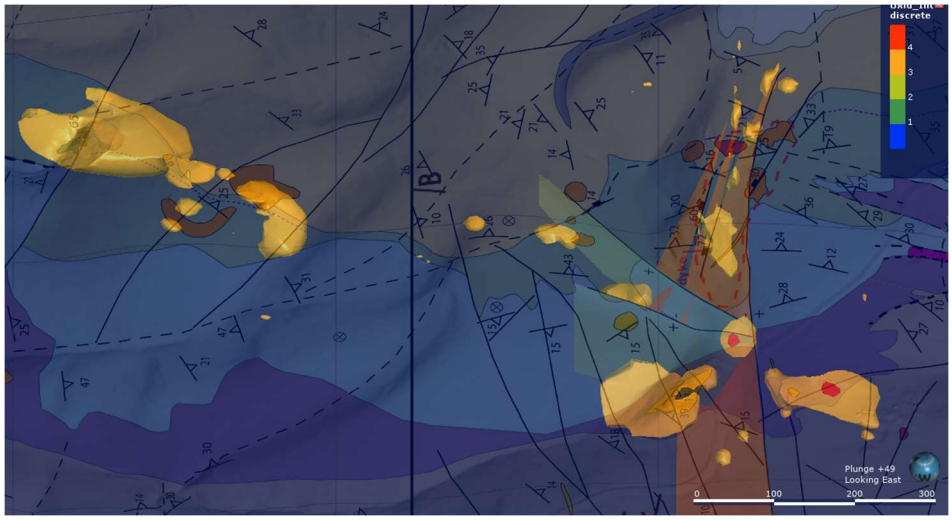

Figure 3.22. Correlation of oxidation ratings with mineralization on the map (looking down).

3.1.9 Construction of 3D Solid Geologic Model

After both the lithologic and oxidation model is merged, the resultant 3D solid geologic model is shown in Figure 3.23. Oxidation is generally higher in the schist units rather than in marbles. The oxidized cataclastic breccia localities marked on the map are also observed with high oxidation localities in the model.

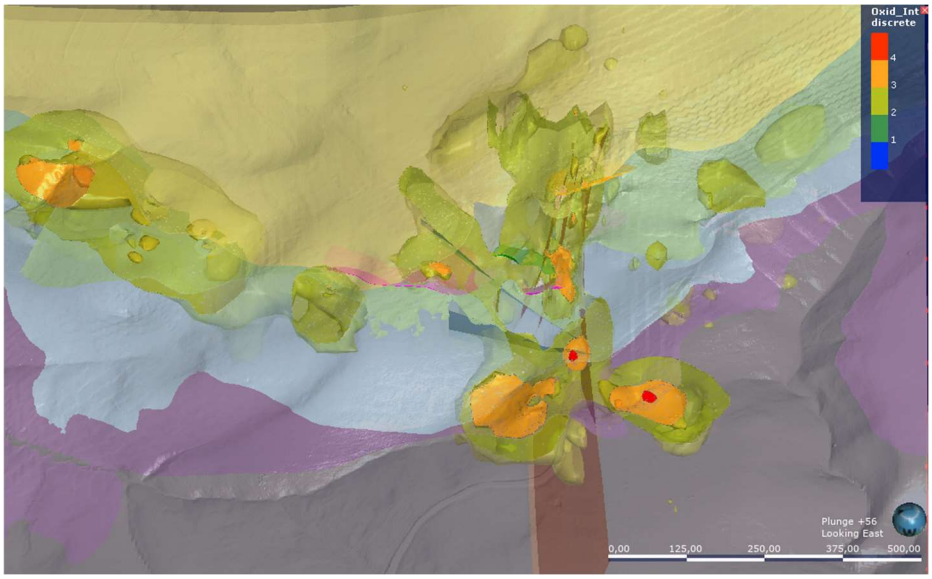

Figure 3.23. The general view of the 3D solid geologic model (looking east).

An ENE-WSW cross-section (Figure 3.24) shows that the oxidation is more continuous in the schist lithologies. Also, the faults are closely associated with oxidation.

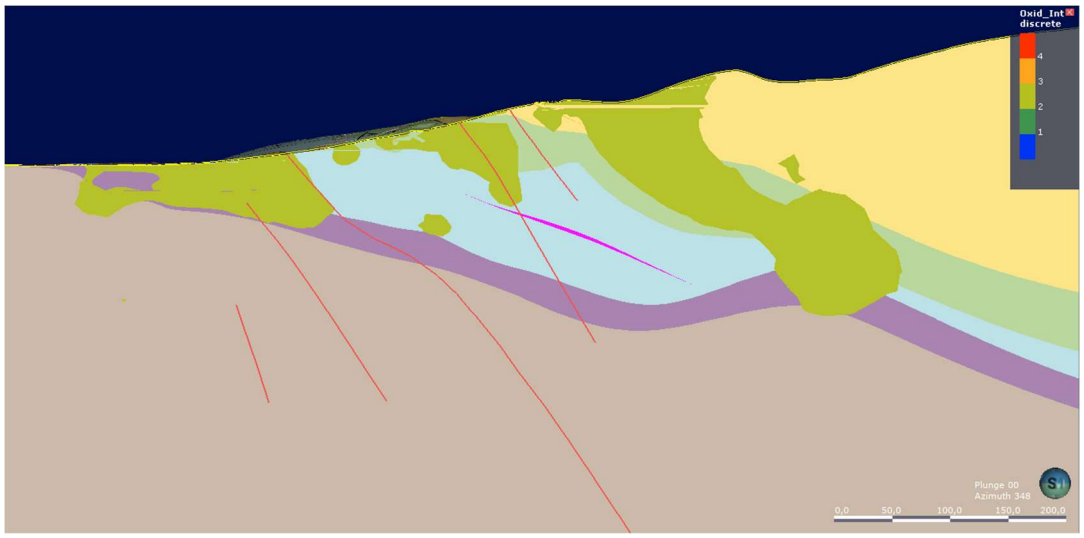

Figure 3.24. ENE-WSW cross-section showing the oxidation distribution in units and faults (looking NNW).

3.2 Evaluation of 3D Solid Geologic Model

This study demonstrated that the geological map of the area and the model are highly matched in terms of units and boundaries. Even though there are some disrupted boundary segments, it is probably caused by ambiguous continuation of boundaries that could not be observed well in the field, or unknown faults which could not be implemented into the model.

The modeling is also useful for revising the geologic map. In Figure 3.25, the different outcrop area of the purple unit in both north and south of the study area is observable. In the south, although both green and purple units are schists; however, differentiating these units in the field was not possible when the overlying blue unit is not present. Thus, modeling is useful to determine the continuation of the planes even in mapping practices.

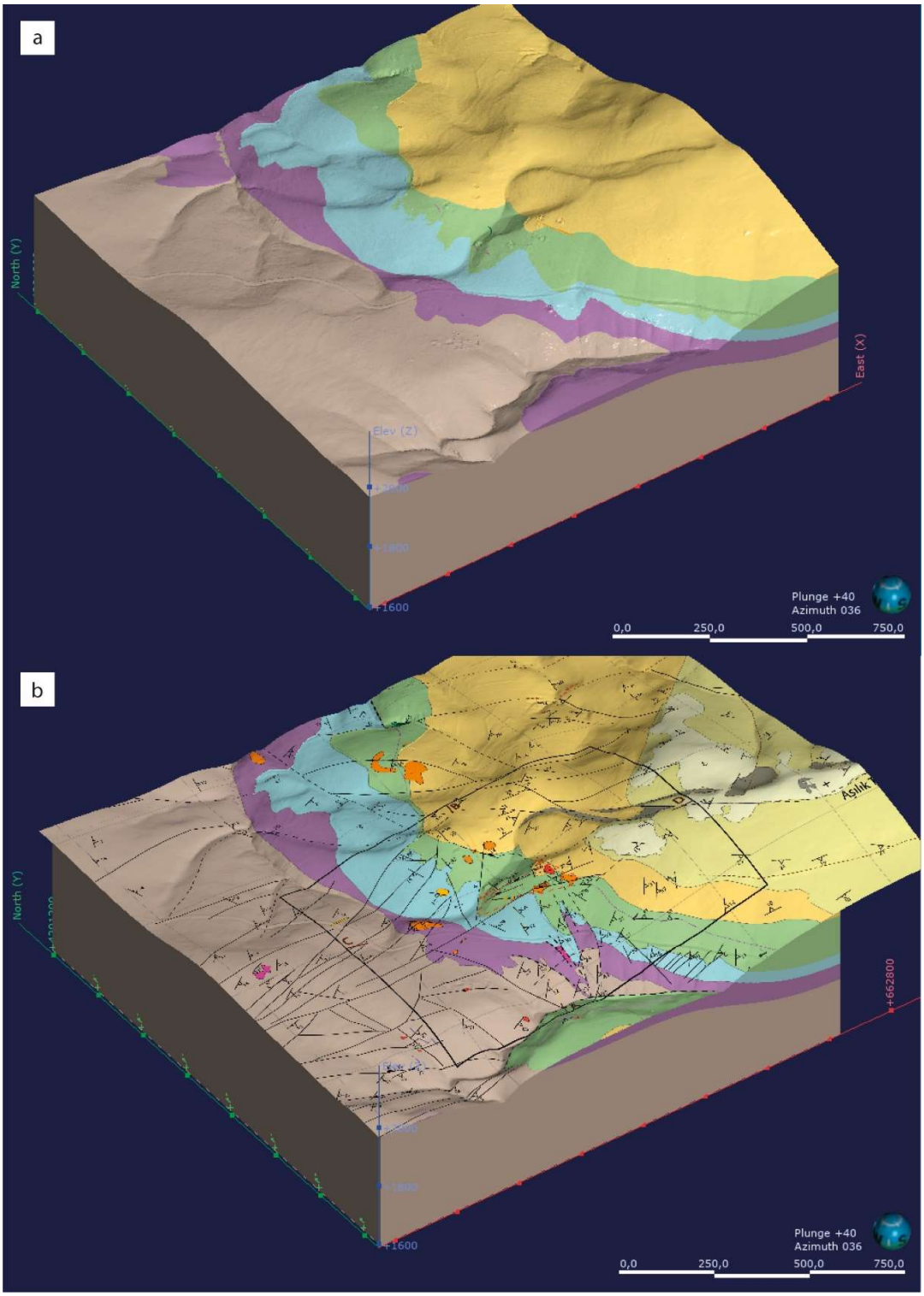

Figure 3.25 The outcrop differences between (a) the resulting model and (b) the geologic map (looking NE).

The slip amounts of the faults in the main mineralization area are neglected since they do not have significant slip amounts at the modeling scale. Therefore, they are depicted as discrete mesh surfaces. Also, Leapfrog Geo requires a fault to divide the model into two domains as hanging wall block and footwall block. To do so, faults should extend to all models from one end to the other. Hence, forming faults as mesh surfaces within their extents is preferred.

Granite could not be modeled properly since its intervals are dispersed all over the model. This is probably because the granitic body in the study area is composed of many small intrusive bodies rather than forming a large single stock. The main intrusion level is thought to be Kaleboynu metamorphics in the study area (Figure 3.26). Dense dike arrays also corroborate this hypothesis.

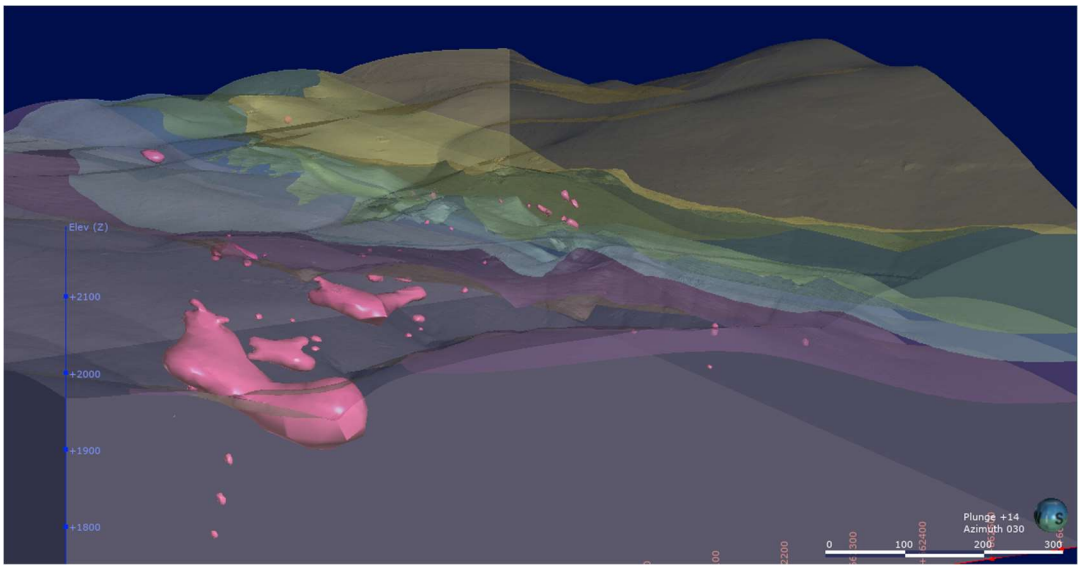

Figure 3.26. The granite bodies in the study area (looking NE).

Two dikes modeled in the main mineralization area are crosscutting the foliation planes with a shallow angle. Also, Fe-oxides is a planar structure located at the marble-schist boundary on the top of the main mineralization area (Figure 3.27).

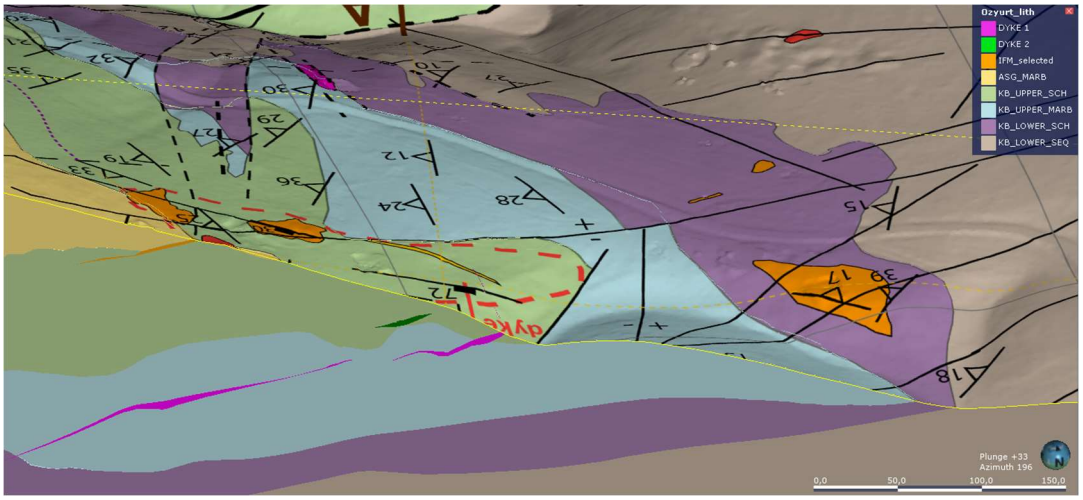

Figure 3.27. Dike_1, Dike_2 and IFM_selected in NW-SE cross-section (looking SE).

The cross-sections produced in the field studies resemble the model. In cross-section AB, besides the fault with the high-slip amount and thickness of the purple unit the section is consistent with the model (Figure 3.28).

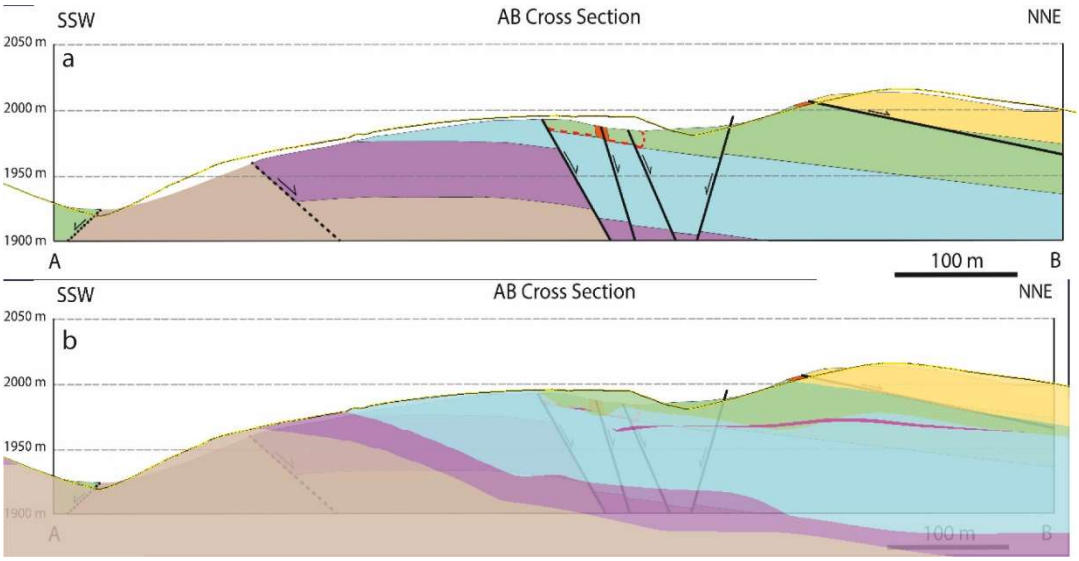

Figure 3.28. Comparison of (a) cross-section AB and (b) cross-section AB in the model.

In section CD, the unit thickness of the Aşıgediği metamorphics (yellow) and the dip of the units beneath the Aşılık Tepe in the ESE side vary greatly in two sections (Figure 3.29). This is primarily caused by the difference between surface foliation measurements and the continuation of the foliation beneath the Aşılık Tepe. There is

also an odd folding observed in the purple and blue units in the model. Such a disturbance in the model can be explained with a possibility of a fault.

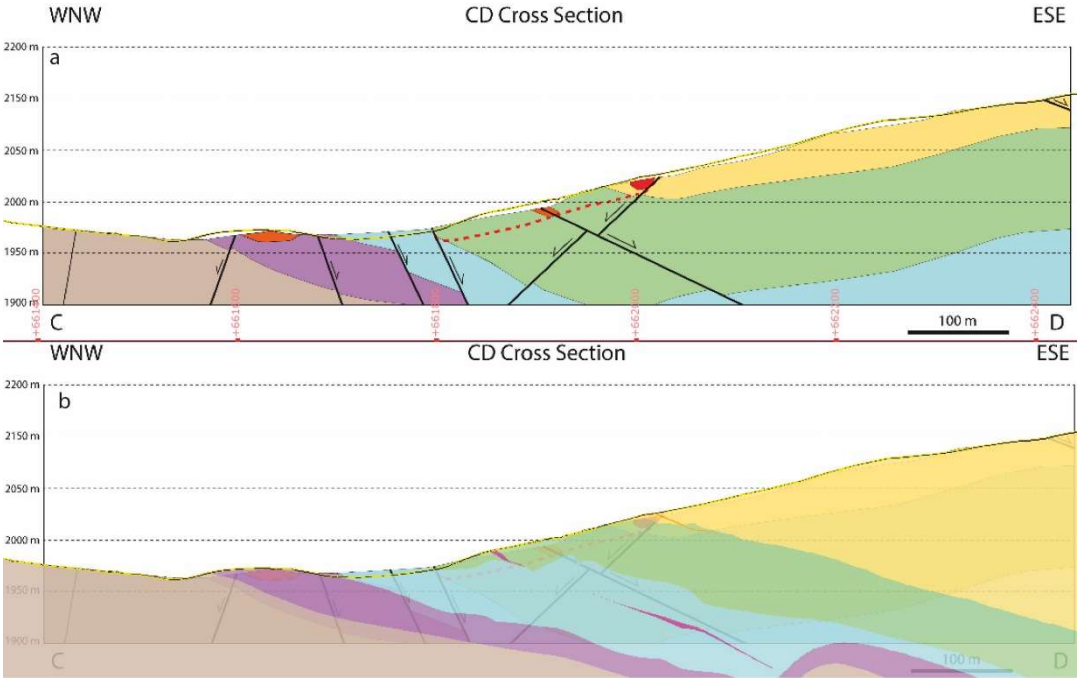

Figure 3.29. Comparison of (a) cross-section CD and (b) cross-section CD in the model.

Overall, the solid model generated is consistent with the geologic map produced in the field studies. The modeling is useful to reveal the geometry of structures that could not be observed in the field. The oxidation intensity and gold mineralization relationship are constrained in the solid model. The model is quite accurate to show the temporal relationships between structures and units; however, the data quality greatly affects precision errors observed partially.

CHAPTER 4

PETROGRAPHY AND ORE MINERALIZATION

A total of 19 polished thin sections are prepared to define host rock lithologies, dominant alteration types and ore mineral assemblages of the Özyurt gold deposit. 18 of these are taken from mineralized intervals of three different drillholes (OZD91, OZD97 and OZD103) and one is taken from a cataclastically deformed schist outcrop at the field.

The analyses of polished thin sections are evaluated in two parts. The first part describes the various lithologies intersected during drilling and also hydrothermal alteration types observed in these rocks . Suitable host rocks and mineralization related alterations are presented. The second part deals with the paragenesis of the Özyurt gold deposit. According to this study, at least 3 different stages of mineralization, a subsequent post-mineralization stage and a supergene stage were identified.

4.1 Petrography and Alteration

Niğde Massif contains a variety of foliated metamorphic rocks with alternating clastic-chemical sedimentary protoliths. The alternating nature of the metamorphic rocks observed at the outcrop scale is also consistent with the micro-scale observations. In general, the schistose rocks in the study area were determined as quartz-sericite± carbonate±biotite schists. For instance, in sample OZD-97, 172.80 m (Figure 4.1 a-b), alternating quartz domain and sericite-feldspar-carbonate dominated domain are observed. K-feldspar and plagioclase (possible albite) commonly show clay and sericite alteration. In the sericite-feldspar-carbonate domain, disseminated iron oxides and pyrite are present within the foliation. On the other hand, the quartz domain has no sulfide or iron oxide content. A late carbonate

vein crosscutting primary foliation as well as disseminated iron oxide and pyrite. Quartz shows grain boundary migration indicating high-temperature conditions (Passchier and Trouw, 2005). Although banding in the quartz domain is present, the foliation at the rest of the rock can be defined as a schistosity.

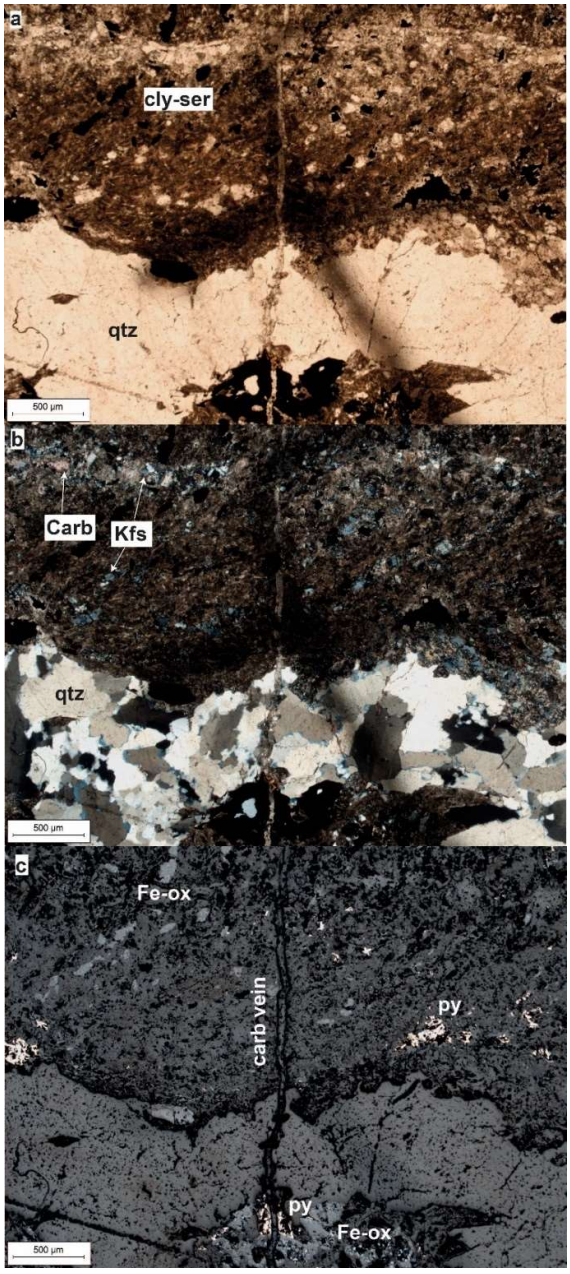

Figure 4.1. Altered schist showing alternating layers of quartz and K-feldspar-carbonate-sericite crosscut by a barren carbonate vein. Clay alteration is commonly observed. Pyrite and iron oxides are disseminated within foliation from OZD97-172.80 m under (a) PPL, (b) XPL, (c) reflected PPL.

Most schist samples show cataclastic deformation. The deformations generally occur along the foliation as anastomosing cataclastic zones. In some samples, quartz-sericite±carbonate schists intensely brecciated or completely turn into cataclasite with fault gouge. In each case, the samples are rich in terms of sulfide content. The sulfide minerals are often oxidized to iron oxide minerals like hematite. Native gold and electrum are also present due to the breakdown of sulfides and subsequent liberation. Rutile±ilmenite alteration is frequently observed as disseminations in sericitic layers of schists.

The marbles in the study area consist of calcite-albite-epidote±quartz as mineral assemblage (Figure 4.2 a). Calcite amount in the samples is approximately 90-95% with interlocking, anhedral to subhedral crystals Quartz is only observed in brecciated marbles near schist contact; therefore, it can be interpreted as an inclusion in the marbles. Well-developed kink bands can be observed in calcite (Figure 4.2 b). There are carbonate veins within these rocks, yet they don't have any sulfide. There is very low sulfide content (lower than 1%) throughout the marble compared to schists. Karstic cavities in brecciated marbles have been commonly coated with hematite. (Figure 4.2 c).

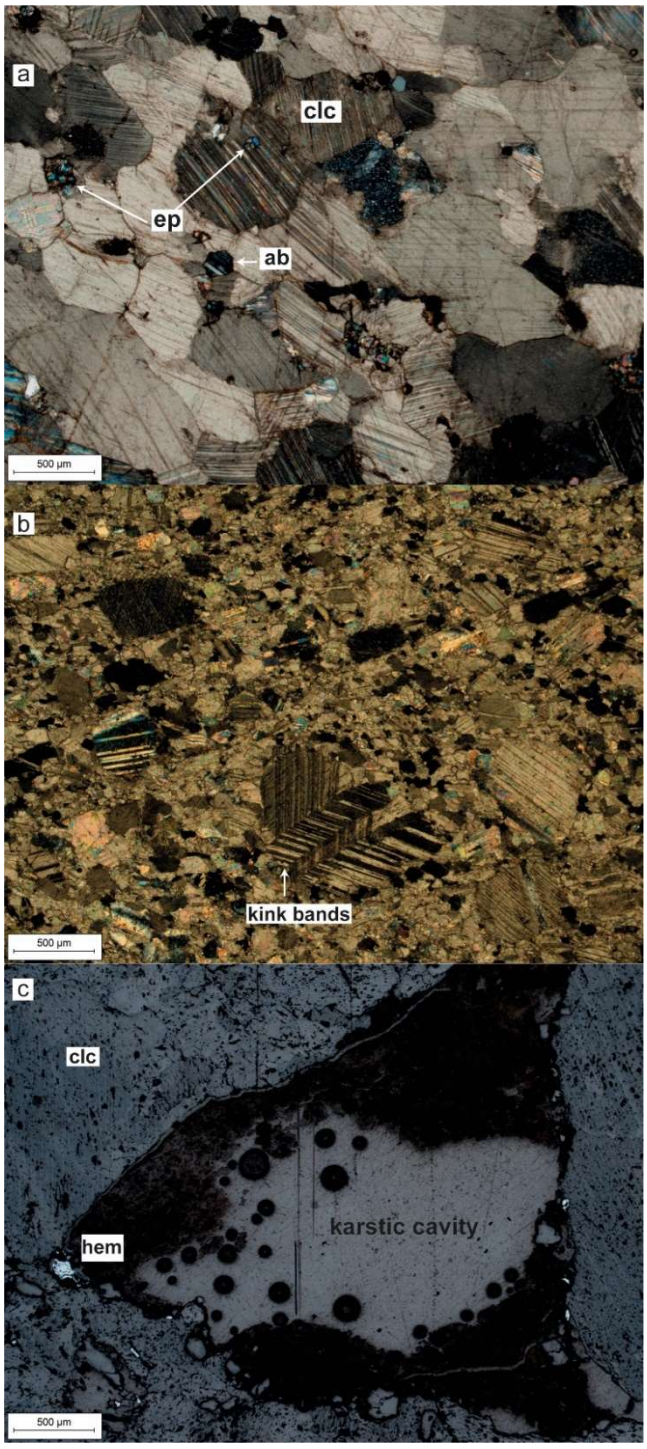

Figure 4.2. General view of a marble samples. (a) calcite-albite-epidote assemblages in the marble from OZD103-264.40 m under XPL, (b) kink bands observed in twinning of calcites from OZD103-272.80 m under XPL, (c) hematite mineralization in a karstic cavity from OZD103-270.20 m, reflected PPL.

In the deeper levels, corresponding to the boundary between Gümüşler and Kaleboynu metamorphics, well-developed quartz and muscovite-biotite bands with garnet are observed (see OZD97, 423.30 m in Figure 4.3 a-b). Sigmoidal-clasts and boudinages are very common. Quartz shows grain boundary migration indicating dynamic recrystallization. Muscovite-biotite bands show mylonitic textures along their domains and are filled with very fine pyrite and chalcopyrite (Figure 4.3 c). Generally, sulfide assemblages are observed in the muscovite-biotite mylonitic shear zones; however, quartz contains minor sulfides. Furthermore, a possible gold/electrum grain was spotted inside quartz. The sample also exhibits top-offsetting of a vertical, foliation cutting, late carbonate vein along the muscovite-biotite mylonitic shear zones in top-to-right motion sense. The late carbonate vein is devoid of any sulfides. Since these structures are all over the section, a stitched image was created to show the relationship between them. (See Appendix A).

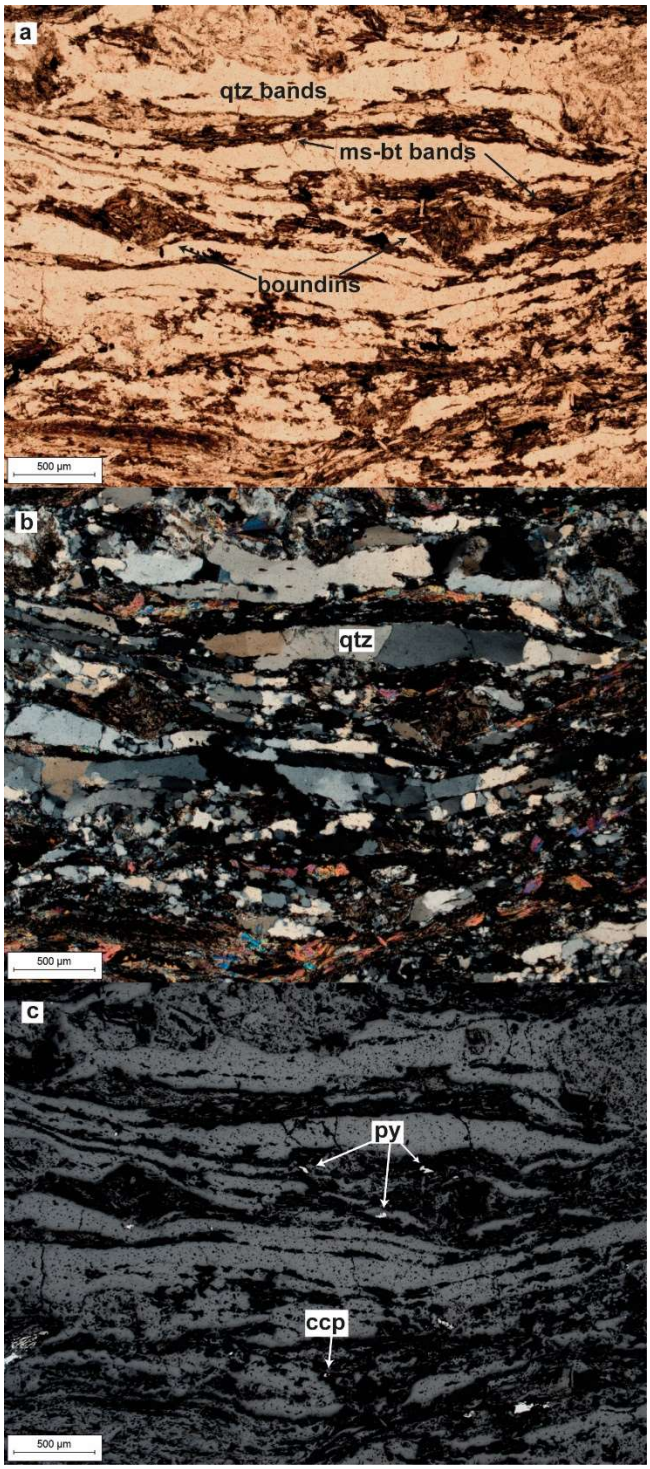

Figure 4.3. Quartz-muscovite-biotite gneiss contains pyrite-chalcopyrite disseminations from OZD-97, 423.30 (gneiss) under (a) PPL, (b) XPL and (c) reflected PPL.

In some intervals, unusually pyroxene-rich domains are spotted (Figure 4.4 a, b, c). These domains are usually composed of pyroxene-sericite-albite-carbonate mineral assemblages (Figure 4.4 a). In some of the samples (OZD97-423.30 m), clinopyroxenes dominate the section; however, in others (OZD91-296.20 m) clinopyroxenes are accompanied by actinolite-tremolite-white mica-biotite-albite-calcite. This mineral likely indicates a mafic protolith for this part of the schist unit. The spatial distribution of sulfides in the studied samples are highly variable. In sample OZD97-423.30m, nearly all sulfide minerals are in the clinopyroxene-rich domain rather than contacting the quartz domain. However, in samples OZD91-295.90m and 296.20m, there is only a small amount of pyrite-pyrrhotite-chalcopyrite in micas within clinopyroxene-rich zones. Pyroxenes are also locally boudinaged between quartz (Figure 4.4 b).

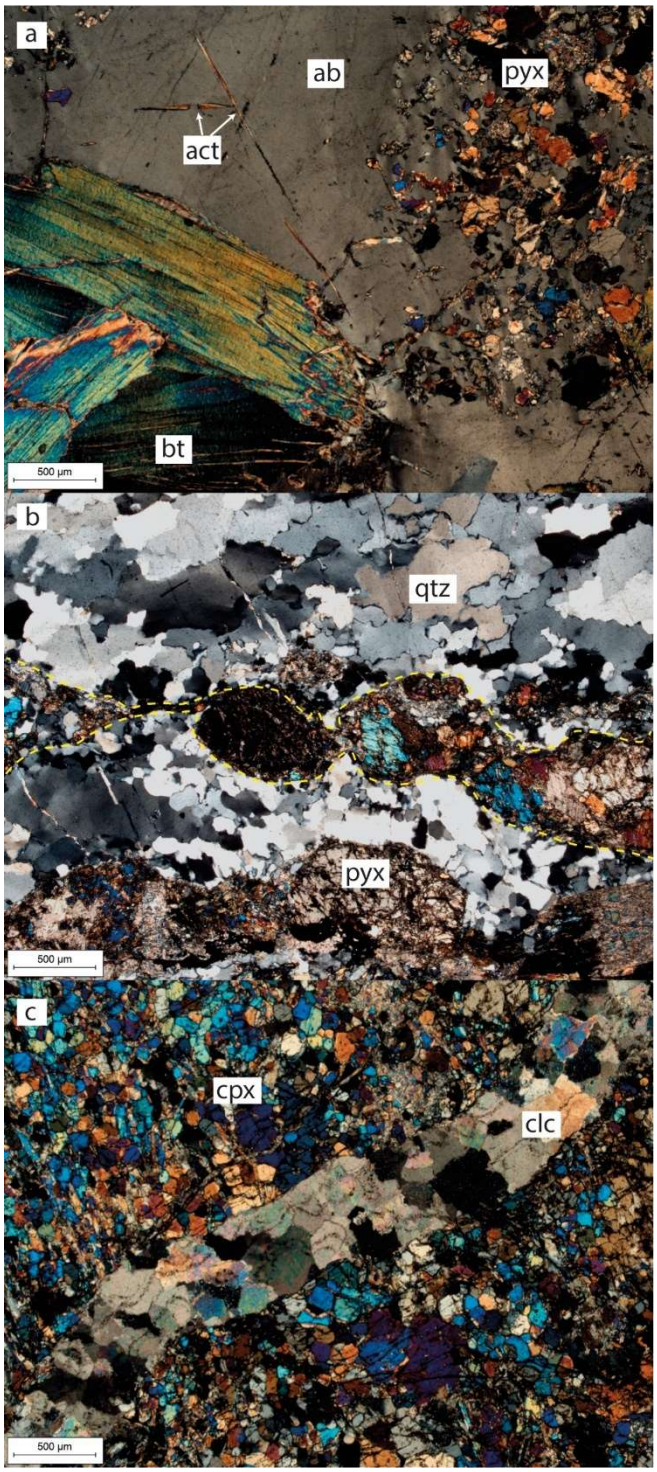

Figure 4.4 (a) Pyroxene clusters within albite, also coarse biotites. Actinolite as spikes developed in albite, from OZD91-296.20 m, XPL, (b) pyroxene boudins between quartz from OZD97-423.30 m, XPL, (c) Clinopyroxenes and open-space filling, botryoidal textured calcite vein from OZD91-295.90 m, XPL.

4.2 Paragenesis

At least three different stages (Stage 1-2-3) related to hydrothermal ore mineralization were identified during petrographic studies. Following that, a post-mineralization stage with widespread carbonate veins is recognized. Also, there is a supergene stage associated with the breakdown of previously mineralized sulfide minerals and the formation of oxide minerals in deformed zones. The main criteria while determining the stages are spatial distributions of minerals, cross-cutting relationship of structures, and replacement textures. Rutile-clay±ilmenite alterations are commonly observed along foliation planes. Rutile±ilmenite minerals are commonly found in close spatial association with micas in sericitic rock.

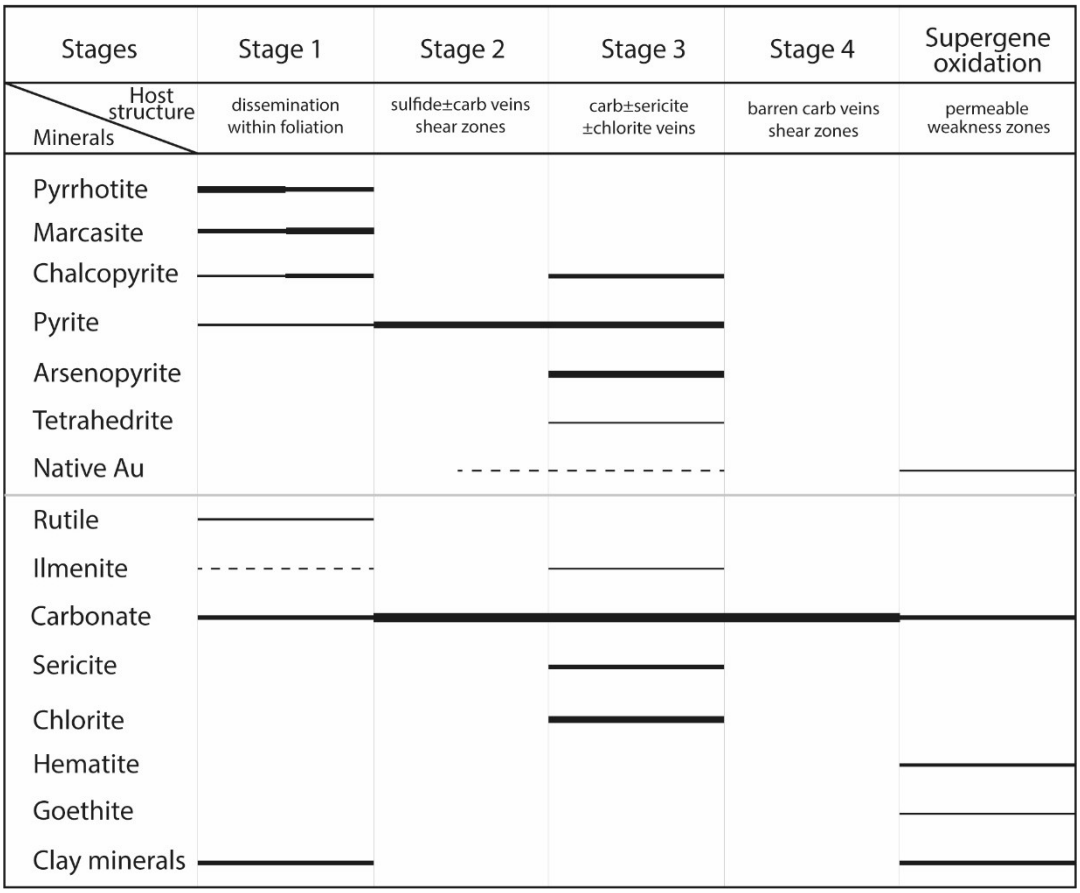

Figure 4.5. The paragenetic sequence of the Özyurt gold deposit.

4.2.1 Stage 1

In stage 1, marcasite-pyrrhotite-chalcopyrite±pyrite mineral assemblages are recognized. The minerals are commonly found together as clusters at the contacts of pyroxene-sericite-carbonate-albite layers (Figure 4.6, a-b) or as disseminations within the foliation of quartz-sericite-carbonate schists and gneisses (Figure 4.7, e-f). In some instances, ore minerals enclose chloritized mica minerals (Figure 4.6, d-f). They are also observed in a clay-carbonate vein oblique to foliation (Figure 4.7, a-c), at the contacts of pyroxene-sericite-carbonate layers and foliation parallel veinlets. The intergrowth texture is seen in the marcasite-chalcopyrite pair which is showing the co-occurrence of these minerals (Figure 4.7, c). Marcasite growths are observed in pyrrhotite. These growths are as spikes from the periphery to the center of pyrrhotite minerals, indicating pyrrhotite is partially replaced by marcasite (Figure 4.6c). The minerals formed at this stage are commonly anhedral and have a sooty appearance.

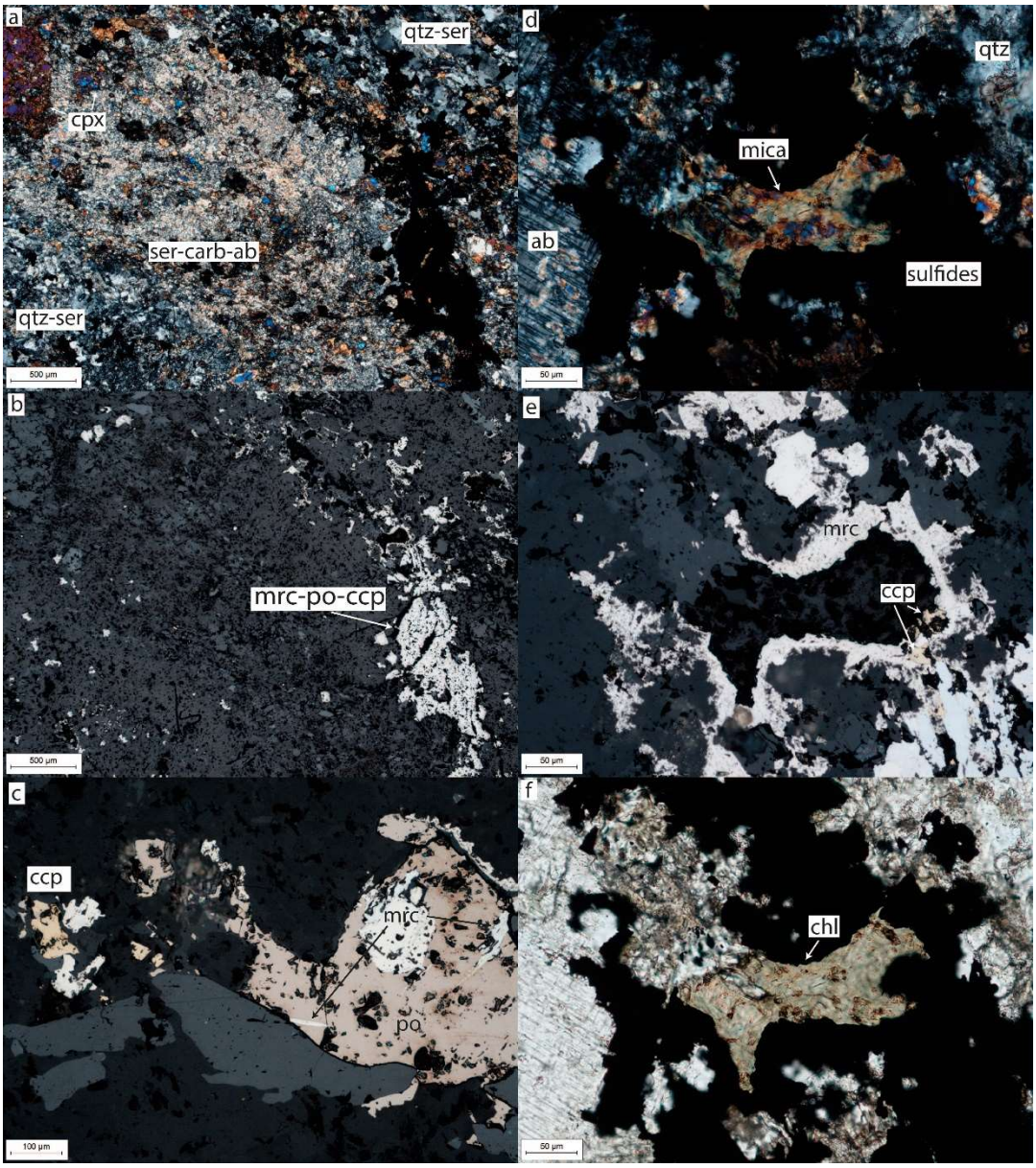

Figure 4.6. Stage 1 mineralization in OZD97-143.70 m. (a) General view of the ore minerals (black) in the contact of the clinopyroxene-sericite-albite bearing layer with quartz-sericite schist, XPL, (b) general view of the ore minerals, reflected PPL, (c) Pyrrhotite-marcasite-chalcopyrite association. Marcasite is replacing the pyrrhotite with spikes from the periphery, reflected PPL, (d) Mica enclosed by ore minerals in the contact of clinopyroxene-sericite-albite bearing layer, XPL, (e) Mica enclosed by marcasite and chalcopyrite, reflected PPL, (f) pleochroic greenish chlorite replacing mica, PPL.

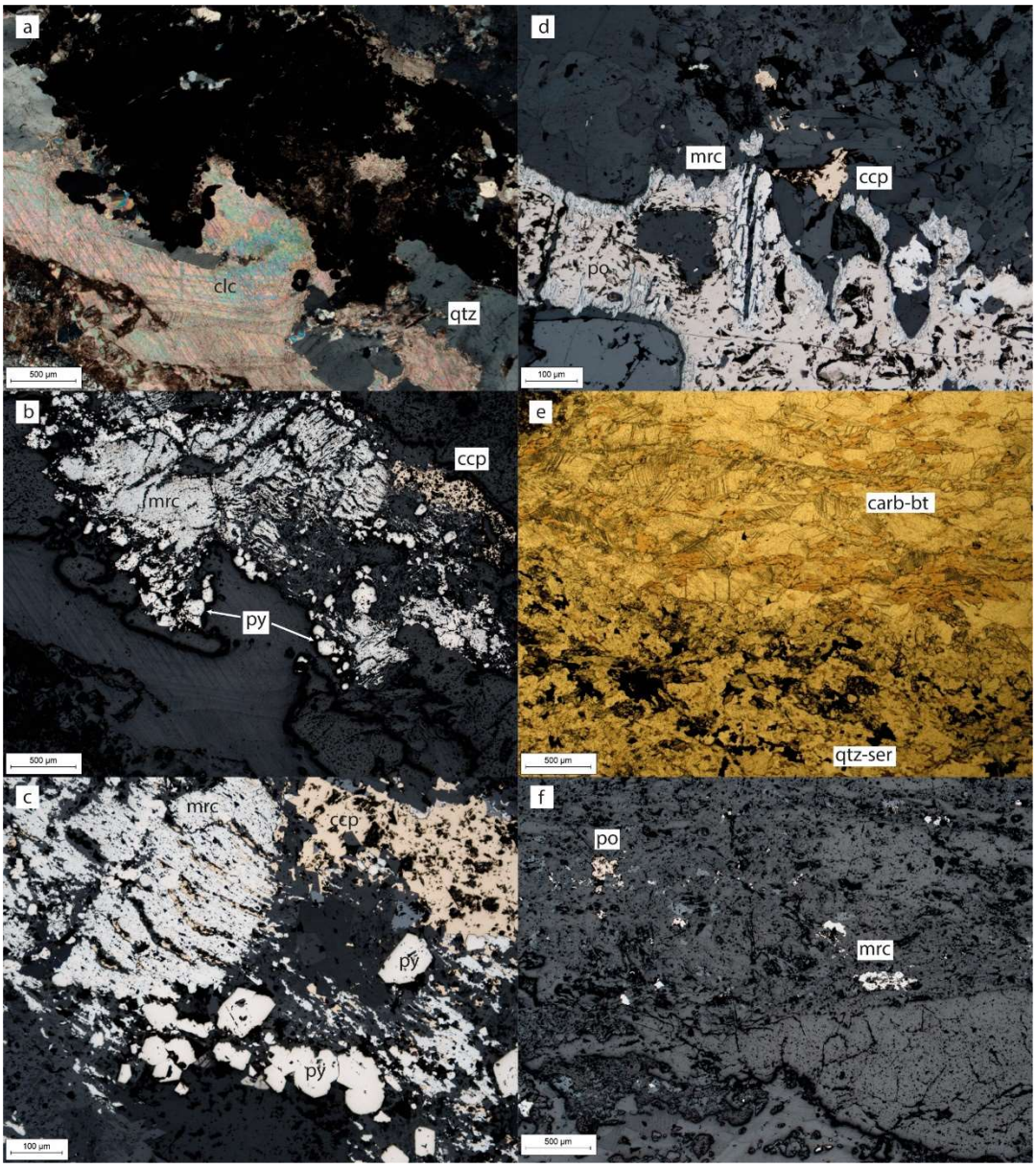

Figure 4.7. Stage 1 mineralization (a), (b), (c), (d) in OZD97-168.10 and (e), (f) in OZD97-143.70 m. (a) Stage 1 mineralization in clay-carbonate vein cross-cutting a big quartz vein, XPL, (b) Stage 1 marcasite and chalcopyrite with sooty texture replaced by stage 2 pyrite at the periphery of the clay-carbonate vein, reflected PPL, (c) a close-up view to the clay-carbonate vein. Stage 1 marcasite-chalcopyrite intergrowth is observed. Stage 2 pyrites replacing stage 1 minerals, reflected PPL, (d) pyrrhotite-marcasite-chalcopyrite cluster in the foliation. Marcasite is replacing the pyrrhotite, reflected PPL, (e) quartz-sericite layer contains ore minerals whereas carbonate-biotite layer does not, PPL, (f) pyrrhotite and marcasite within the foliation of quartz-sericite schist, reflected PPL.

4.2.2 Stage 2

This stage is characterized as pyrite±carbonate veins and veinlets filled fractures orthogonal to the foliation and pyrite mineralization occurred within cataclastic shear zones (Figure 4.8 a-d). Stage 1 minerals are often associated with stage 2 pyrite which was observed in subhedral to euhedral shaped (Figure 4.7 c). Unlike stage 1, the pyrite minerals formed in this stage is clean looking. The well-developed appearance of stage 2 pyrite and their nearby association with stage 1 minerals in some samples suggests that stage 1 minerals might be partly recrystallized to stage 2 pyrite. The textural similarity of pyrites and foliation cross-cutting distribution of them are common properties of this stage.

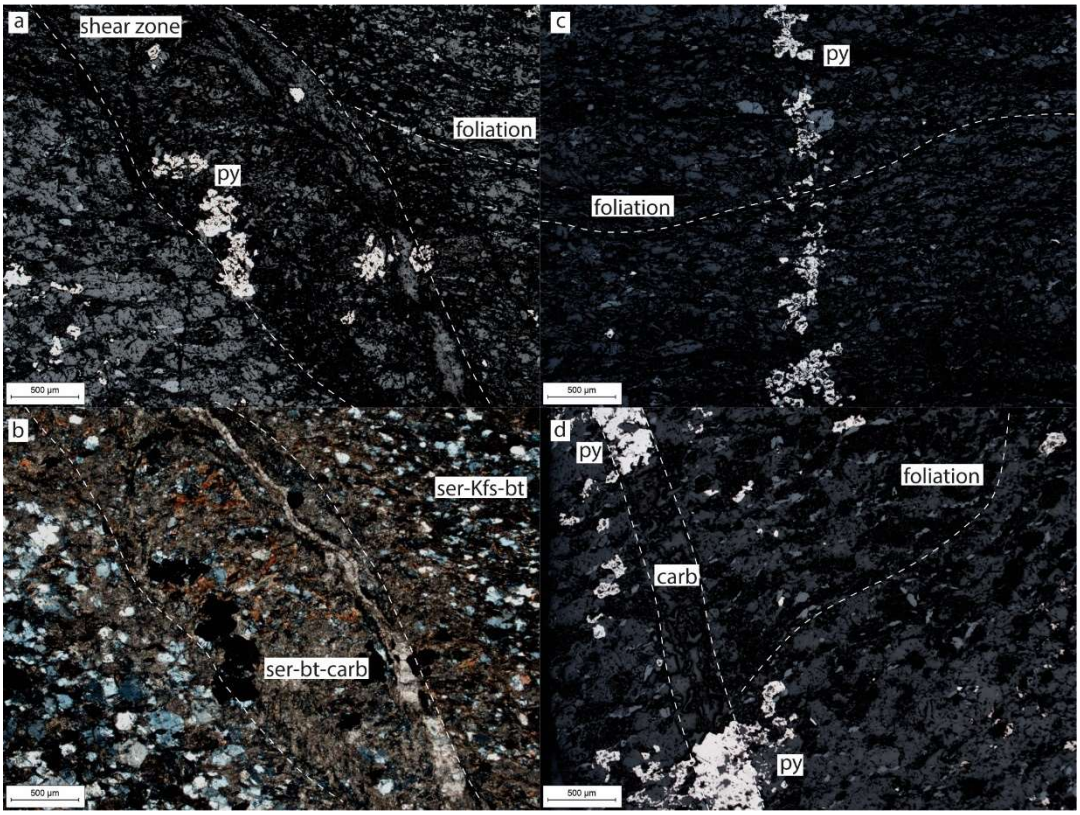

Figure 4.8. Stage 2 mineralization in OZD97-414.30m. (a) Pyrite mineralization within a shear zone cross-cutting foliation obliquely, reflected PPL, (b) ore-bearing shear zone consists of sericite-biotite-carbonate while the rock contains sericite-K-feldspar-biotite, XPL, (c) pyrite vein formed in a fracture orthogonal to the foliation, reflected PPL, (d) carbonate-pyrite vein cross-cutting the foliation, reflected PPL.

4.2.3 Stage 3

Stage 3 is represented by thearsenopyrite-pyrite-chalcopyrite±tetrahedrite mineral assemblages and is hosted in carbonate±chlorite±sericite veins (Figure 4.9 b-c). Chalcopyrite is commonly found as small aggregates with possible tetrahedrite (Figure 4.9 d-e). Although tetrahedrite is quite difficult to distinguish from only its optical properties, it was interpreted in polished thin sections due to its close association with chalcopyrite Ilmenite is also observed in some carbonate-chlorite veins. In several instances, newly formed euhedral arsenopyrite replace stage 2 pyrite (Figure 4.9 a). Fan-shaped chlorites and sericite with carbonates with their different ore mineral assemblages are typically distinctive features of this stage.

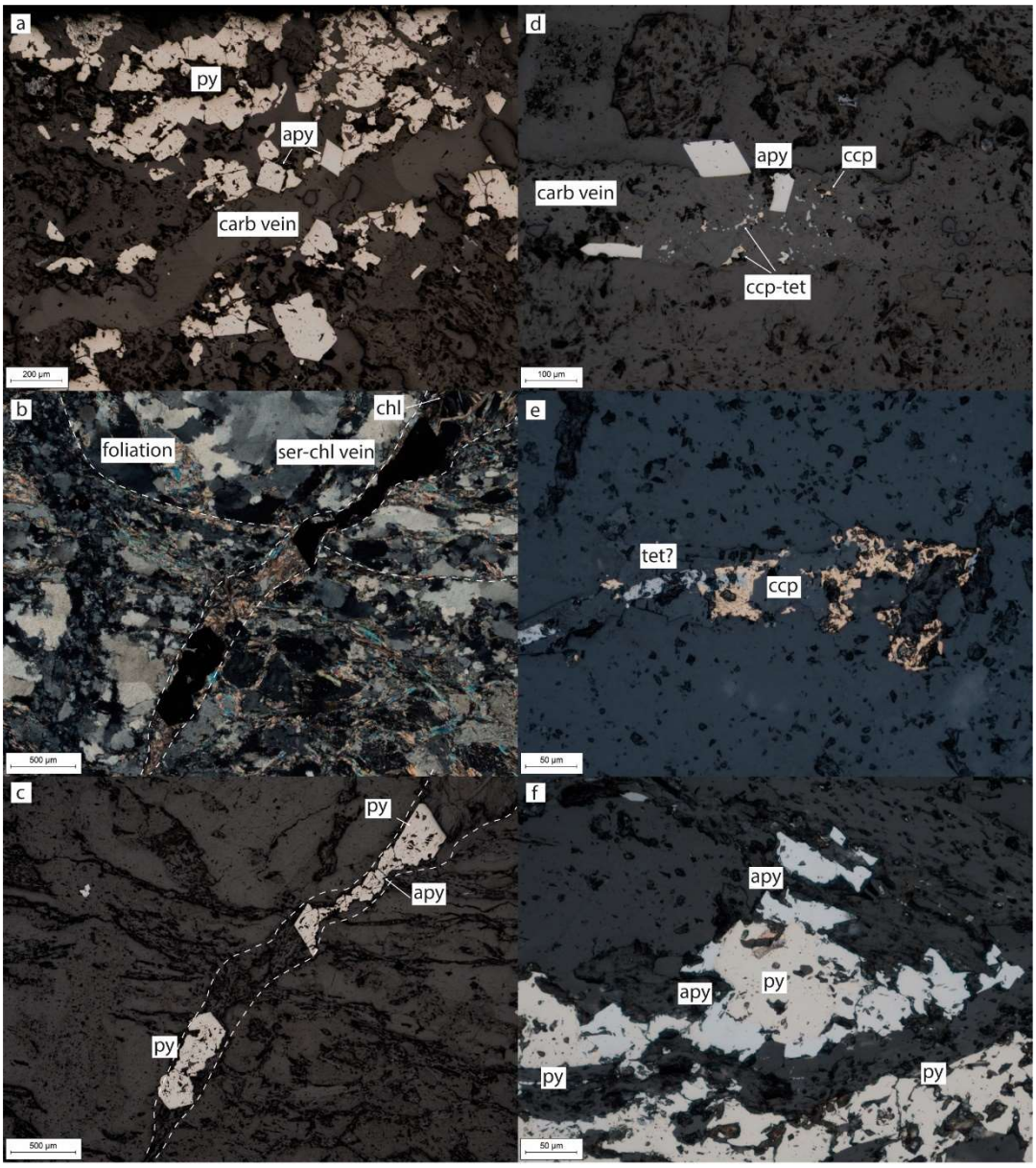

Figure 4.9. Stage 3 mineralization (a), (d) from OZD97-172.80 m and (b), (c), (e), (f) from OZD103-175.30 m. (a) Arsenopyrite-carbonate vein cross-cutting stage 2 pyrite, reflected PPL, (b) ore-bearing sericite-chlorite vein cross-cutting the foliation of quartz-sericite schists, XPL, (c) pyrite and arsenopyrite within the sericite-chlorite vein, reflected PPL, (d) arsenopyrite-chalcopyrite-tetrahedrite within carbonate vein, reflected PPL, (e)chalcopyrite and possible tetrahedrite aggregate, reflected PPL, (f) arsenopyrite and pyrite found together, reflected PPL.

4.2.4 Stage 4

Stage 4 is composed of post-mineralization, barren, carbonate veins, mainly composed of calcite. Orientation of these veins is usually oblique to orthogonal with respect to the foliation (Figure 4.10, a-d). The veins are sometimes developed in shear zones, which are recognizable due to deformational textures and drag folds formed by the foliation planes (Figure 4.10, b-d). Also, cataclastic deformation and microfaulting of stage 2 pyrite are commonly observed near fault-fill carbonate veins indicating brittle conditions were dominant at stage 4 (Figure 4.10, c-f). There is no direct cross-cutting relationship between stage 3 and stage 4; however, increasing brittle deformation, diminish of ore minerals, and field observation of fracture and shear zone fill carbonate veins cross-cutting ore-bearing zones suggest barren carbonate veins of stage 4 probably outdated stage 3.

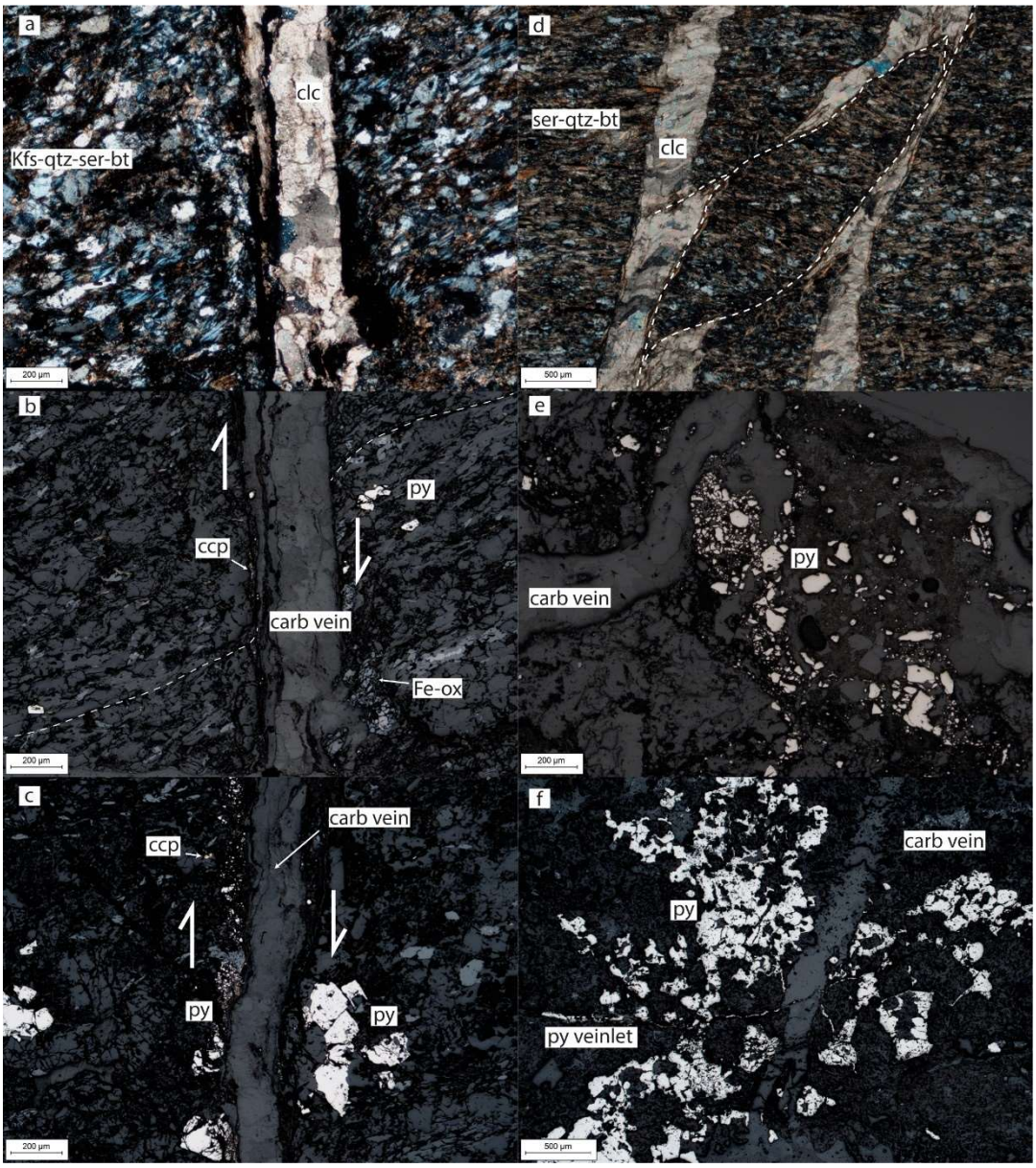

Figure 4.10. Stage 4 mineralization (a), (b), (c) from OZD97-414.30 m, (d) from OZD103-158.50 m, (e) from OZD103-157.80 m, (f) from OZD103-172.80 m. (a) Carbonate vein cross-cutting the foliation of K-feldspar-quartz-sericite-biotite schist, XPL, (b) Fe-ox(?), pyrite and chalcopyrite near the carbonate vein, carbonate vein filled a fault, drag folds are visible, reflected PPL, (c) carbonate vein hosted a fault. On the left, pyrite undergone cataclasis. On the right, a brittle microfault cuts pyrite, reflected light (d) carbonate veins crosscutting sericite-quartz-biotite schist, faults rotate a slice of the foliation, XPL, (e) pyrites were cataclastically deformed and were cross-cut by a late carbonate vein, reflected PPL, (f) pyrite cluster was cross-cut by a carbonate vein which is also cross-cut by a pyrite veinlet, reflected PPL.

4.2.5 Supergene Oxidation

The supergene oxidation is best observed in cataclastically deformed, brecciated zones (Figure 4.11 a, f). The mineral assemblage of this stage consists of native gold-hematite±goethite. Widespread clay alteration and late carbonate veins are present in shear zones. Native gold and sometimes possible electrum are typically observed in those shear zones (Figure 4.11 b-e). The intensity of oxidation and gold association is typically observed. Since sulfide minerals cannot be distinguished due to intense oxidation, the affiliated mineralization stage with gold could not be determined precisely. However, it is likely that the gold may be related with arsenopyrite since a gold grain is observed within the traces of a possible arsenopyrite (Figure 4.11 b, c).

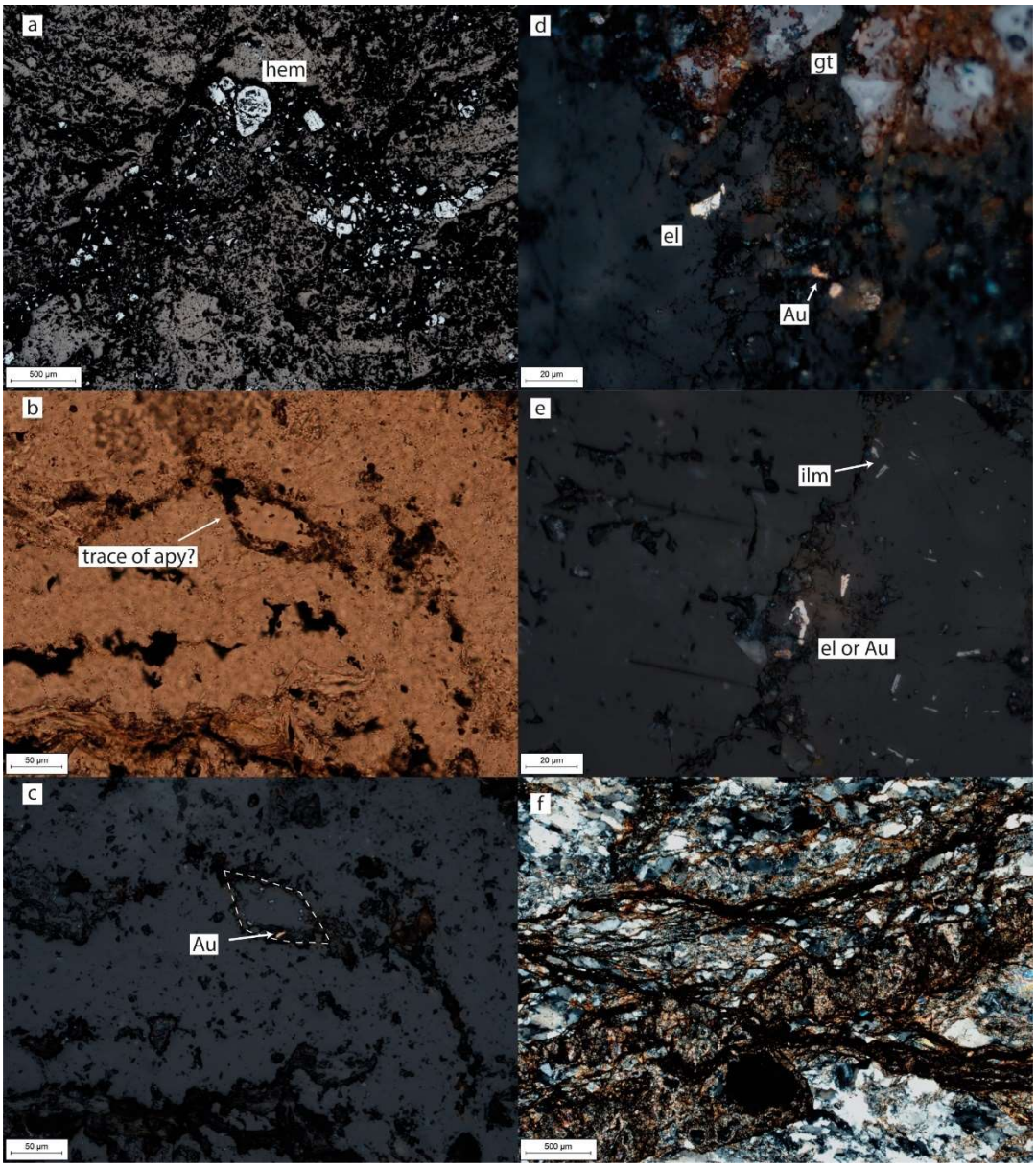

Figure 4.11. Supergene stage in cataclastic breccias (a), (b), (c), (d), (e) from OZD103-299.20 m, (f) from OZP-14. (a) Hematite within cataclastic zones, reflected PPL, (b) possible trace of an arsenopyrite, PPL, (c) native gold is observed within the possible arsenopyrite, reflected PPL, (d) electrum and native gold near goethite cluster of cataclastic breccia, reflected PPL, (e) possible electrum or native gold with ilmenite dissemination, reflected PPL, (g) oxidized anastomosing shear zones within quartz-sericite schist, XPL.

CHAPTER 5

DISCUSSION

5.1 The Competence Difference and Exhumation of the Niğde Massif

The exhumation of the massif requires significant of displacement to unroof it from burial. Layer-parallel shears and low-angle faults are observed in many levels of schists suggesting that foliation planes played an important role as pre-existing weakness surfaces to develop shear zones. During the exhumation of the massif, firstly, ductile shears are formed along foliation planes due to flattening foliation, and then these shears are overprinted by cataclastic deformation due to increasing brittle conditions over time. In the study area, low-angle faults in schists show some ductile features; however, cataclasites and slickensides between the schist foliations and cataclastic breccias in wider deformation zones show progressive brittle overprint.

The Niğde Massif is buried to 16-20 km depths at peak metamorphic conditions (Whitney and Dilek, 1997). The experimental rheology profiles of schist, marble and quartzite lithologies are determined by several studies as illustrated in Figure 5.1 (Schmit et al., 1980; Shea and Kronenberg, 1993; Rutter and Brodie, 2004; Chen and Nabelek, 2017). The results show that the strength profile of the schist is significantly weaker than marble and quartzite lithologies between 6 to 13 km depths. This relationship is coherent with the observation of highly deformed and decoupled schists found in between relatively competent marbles and quartzites at the Niğde Massif. While schists cannot preserve their foliations and are deformed intensely, thick marbles in the study area are less deformed and maintain their foliation planes. However, it should be noted that healing and recrystallization processes would also help marbles to sustain a higher strength compared to schists. Quartzites in the study

area, are observed as thin discontinuous lenses within the schists and can be neglected since they are not mappable.

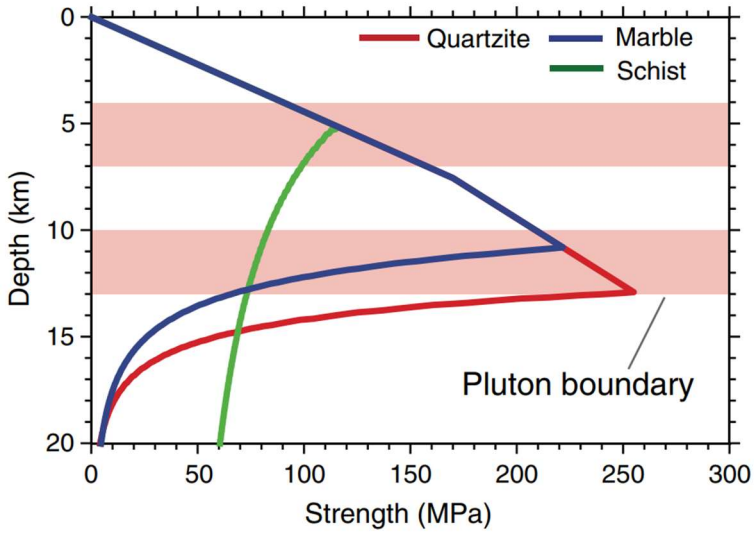

Figure 5.1: Strength profiles of quartzite (Rutter and Brodie 2004), schist (Shea and Kronenberg 1993) and marble (Schmit et al., 1980) lithologies with respect to increasing depth. The strain rate is taken as 10^{-15} s^{-1} (from Chen and Nabelek, 2017).

At 16-20 km depths, marble and quartzite deform plastically, whereas schists relatively have more strength in this interval. During the exhumation, after 11-13 km which is corresponding roughly to brittle-ductile transition depth, schists are becoming significantly weaker than marbles and quartzites. This implies that most of the deformation after brittle-ductile transition should be accommodated by schists, during later phases of exhumation. It is only after 5 km, that all three lithologies share a similar strength profile.

Considering the dominant schist and marble alternation in the Niğde Massif, the competence difference between these lithologies controlled the development of the faults and fractures (Figure 5.2). Similarly, most of the main shears in the cross-section of Gautier et al. (2008) coincide with the unit boundaries where the competence difference is maximum. Therefore, schists in the Niğde Massif are more deformed than the marbles during most of the exhumation history and any weakness plane like foliations within a thick schist unit might have contributed to the total displacement.

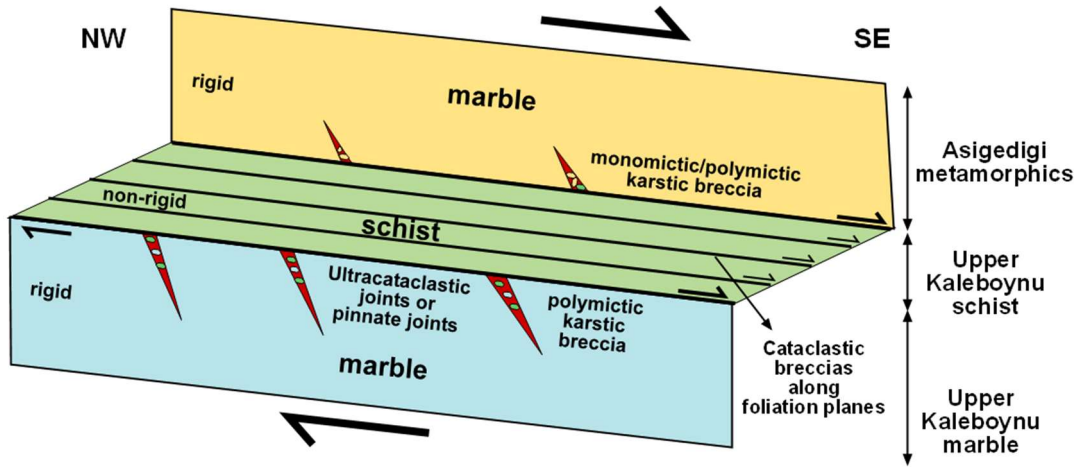

Figure 5.2. The competence difference between schists and marbles in the Niğde Massif.

Ultracataclastic joints (Gautier et al., 2008) or pinnate joints are formed at the contacts (Figure 5.2). These joints are frequently filled by monomictic or polymictic karstic breccias. Also, between the foliation planes of cataclastic breccias are formed overprinting earlier ductile deformations.

5.2 Formation of Özyurt Gold Deposit

Soil, stream and rock sampling surveys acrossdifferent parts of the Niğde Massif indicate massif-scale gold mineralization. However, the formation of an economic mineralization requires distinct elements and factors. At this point, Özyurt gold deposit presents an excellent example for defining the key elements and factors of the mineralization systems in the Niğde Massif.

Field and modeling studies have shown that there are three distinctmineralization in Özyurt gold deposit: (1) low-grade mineralization along foliations of metaclastics. (2) high-grade mineralization in cataclastic breccias along high-angle faults and (3) gossans in the contact of schist and marble or within marbles (Figure 5.3).

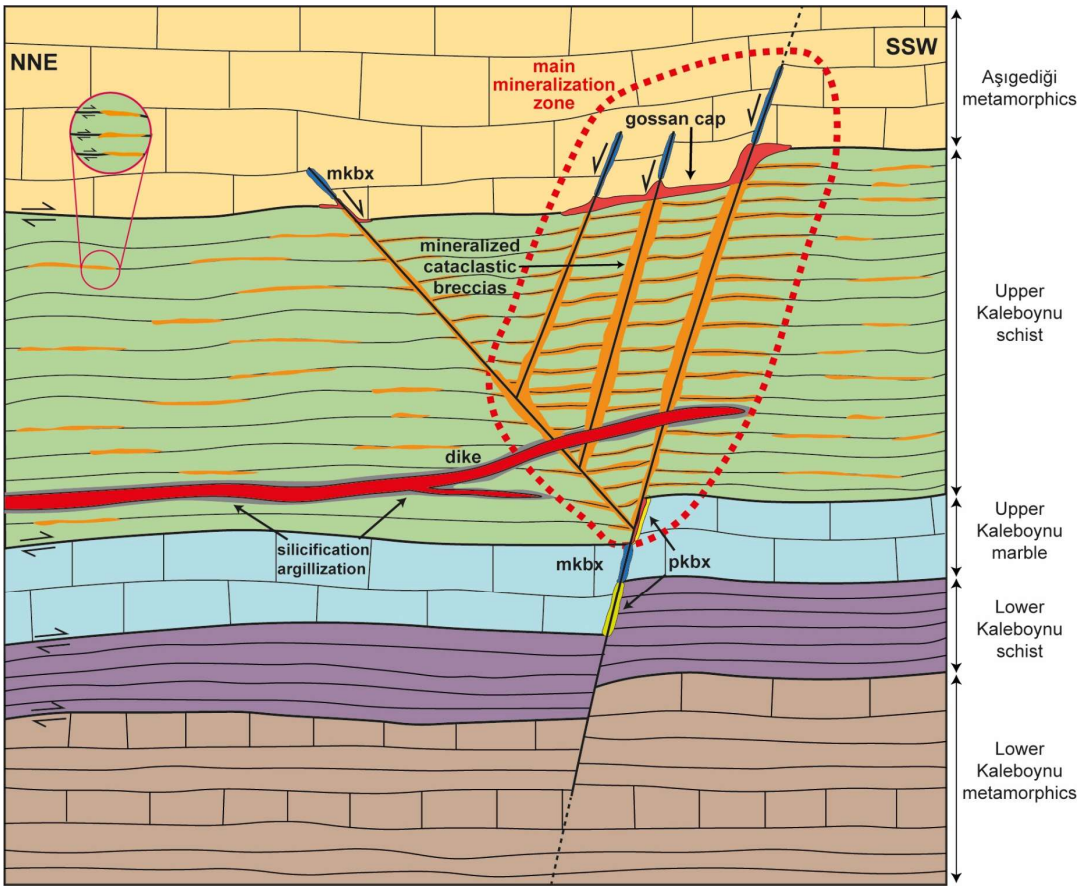

Figure 5.3. Conceptual NNE-SSW-trending cross section showing the architecture of Özyurt gold deposit. (not to scale)

5.2.1 Host Rocks

The gold mineralization is preferably hosted in schist lithologies. Schists in the Niğde Massif are formed by the metamorphism of clastic marine sedimentary rocks. Schists experienced progressive deformation during exhumation of the massif; hence, these underwent intense deformation compared to marbles or quartzite which make schists suitable host rocks for fluid circulation. On the other hand, marbles generally do not contain gold mineralization except for local gossans.

5.2.2 Structure and Geometry

There are two different gold mineralization defined according to this study. The primary mineralization is found in the massif widespread as oxidized schists within low-angle cataclastically deformed shear zones and along foliation planes. Mostly, these zones are developed between the marble and schist boundaries due to their competence difference. Since the schist is less rigid (or competent) than the marble, wide cataclastically crushed schist units provide a good fracture network for any ore-bearing fluid which percolates into these zones. Also, in the marbles, both marble and schist clast-bearing polymictic karstic breccias which contain seldom gold mineralization is observed due to low-angle faulting placed at the marble and schist contacts.

The secondary mineralization is hosted in strongly oxidized high-angle fault networks within schists (Figure 5.4). Cataclastic breccias are brecciated fragments of schists deformed under cataclastic deformation. They are developed within and nearby to the high-angle faults providing a permeable fluid pathways. Also, low-grade mineralization is present below the foliation planes of schists in the main mineralization area. Layer-parallel shear formed due to flattening foliation and subsequent reactivation during exhumation caused the formation of minor weakness zones along foliations in which meteroic fluids seeps from the high-angle fault zones. Densely spaced fault zones ensured to formation of an economic mineralization zone. The high-angle fault zones commonly show cataclastic deformation features; thus, brittle-ductile to brittle conditions should have operated to form these zones. Microscopic studies also showed that ore minerals are hosted in shear zones and fractures, mainly orthogonal to the foliation.

Figure 5.4. High-grade gold mineralization in cataclastic breccias along high-angle faults and adjacent foliation planes (37.934615, 34.842553).

Gossans were observed in the marbles and at the contacts of schist and marbles and located at a structurally higher position from the cataclastic breccias. Modeling studies showed that these structures forms as planes at the schist marble contacts. Gossans are thought to be supergene deposits and formed due progressive leaching by meteroic waters. As a result of the leaching, local but gold-bearing gossans form along the fault tips extending into marbles and at the schist marble contacts as planar bodies.

In summary, a pre-existing high-angle fault network with cataclastic breccias was present before the supergene oxidation period. The meteoric water percolated towards any permeable weakness surfaces including faults and adjacent deformed foliation planes (Figure 5.4) leached some zones and deposited secondary sullfide mineral below the water table, which is enriched in terms of grade . Gossans along schist marble contacts formed as a leached cap to the deposit.

5.2.3 Ore Mineralogy and Alteration Minerals

Two mineralization phase is recognized from the polished thin section studies as primary mineralization and secondary mineralization. The primary mineralization composed of stage 1 in the paragenetic sequence, consisting of sooty textured marcasite-pyrrhotite-chalcopyrite±pyrite disseminated within foliation of schists is interpreted as the primary mineralization. This stage is observed within most of the samples. It is commonly associated with rutile±ilmenite, and clay alteration.

The secondary mineralization which is composed of stage 2 and 3 are extensively developed as veins and veinlets. Stage 2 is composed of fracture and fault-fill carbonate-pyrite veins and pyrite veinlets and stage 3 are composed of arsenopyrite-pyrite-chalcopyrite±tetrahedrite mineral assemblages in carbonate±sericite±chlorite veins filled fractures and faults. The secondary mineralization stages crosscut and replace the primary mineralization stage. Therefore, the secondary mineralization might be formed as secondary sulfide enrichment due to meteoric water activity.

Surface exploration showed that the gold grades in the primary mineralization zones are lower than in the secondary mineralization zones. Therefore, it is interpreted that, the secondary mineralization is formed after enrichment of gold of the primary mineralization through leaching.

The native gold is observed in shear zones of strongly oxidized cataclastic breccias, but the related stage of mineralization could not be determined clearly. Considering the positive correlation of arsenic and gold grades in the massif and gold grain observed in trace of a possible arsenopyrite in thin section studies., it is believed that arsenopyrites of stage 3 might be related to gold.

5.2.4 Fluid Source and Hydrothermal Activity

The source of the gold in the Özyurt gold deposit remains enigmatic. Since the primary mineralization is observed widely in the massif, it is thought to have a relic

metamorphic or pre-metamorphic sedimentary origin. Large et al., (2011) argues that gold and arsenic may be found in diagenetically crystallized arsenian pyrites and pyrites deposited into black shale and turbidites under anoxic and reduced conditions. Since the protolith of the Niğde Massif is composed of an alternating clastic-carbonaceous alternating sedimentary sequence this would explain a pre-metamorphic origin.

According to the field and modeling studies, dikes are observed cross-cutting high-angle faults with gold mineralization. The spatial relationship of dikes and gold mineralization suggest that dikes played a role in enhancing the hydrothermal activity. During the cooling of the Üçkapılı Granite, dense dike and sill arrays are formed in the Niğde Massif. These late intrusive products are formed by the escape of pressurized volatile-rich magma. Thus, the dikes or stocks of Üçkapılı Granite could have provided heat for a prolonged hydrothermal activity period. Nevertheless, the presence of direct genetic relationship between Üçkapılı Granite products and the primary gold mineralization was not observed.

5.2.5 Supergene Stage

As the microscopic studies showed, primary mineralization is associated with sulfide veins and breccias, where there is no visible or microscopic gold. However, no sulfide zone is observed in high-angle faults zones on the surface and instead, the faults and their immediate wall-rocksare strongly oxidized. As the quantitative oxidation model and drillhole data showed high-angle fault network is completely oxidized. This can be explained by a progressive supergene stage.

Progressive groundwater fluctuation over time and continuous meteoric water percolation through the permeable fault network oxidized and breakdown all sulfide minerals and liberated the gold. Unlike other mineralization sites in the massif, arsenic values are quite low since it was washed away at the supergene stage. At the

deeper levels, meteoric waters formed the enriched high-grade secondary sulfide zone below groundwater level.

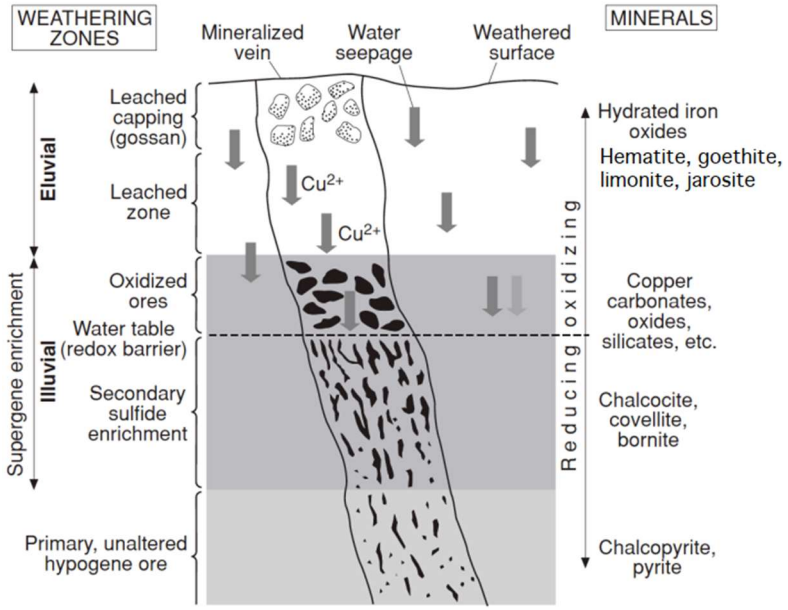

Figure 5.5. The diagram showing supergene enrichment and leaching through meteoric water activity. (from Robb, 2005)

In summary, the primary gold mineralization is formed the hypogene ore, whereas the secondary gold mineralization (stage 2 and 3) is occurred due to secondary sulfide enrichment. Gossans were developed at the top of the leached oxide zones.

5.2.6 Timing of Mineralization and Tectonic Setting

The timing of the gold mineralization is estimated by using some constraining geologic features and shown in Figure 5.6. The primary gold mineralization in the massif should have been deposited during the first exhumation. The spatial relationship of syn-tectonic dikes and the primary gold mineralization along the foliations of metamorphic rocks indicates that the hydrothermal activity occurred at a period when dikes are intruded. Geochronologic studies showed that the emplacement interval of Üçkapılı Granite is determined as 85-76 Ma (Whitney et al., 2003; Gautier et al., 2008). Since the dikes are the latest products of the cooling

granite, Gautier et al. (2008) dated 75.1 ± 0.84 Ma by using $^{40}Ar/^{39}Ar$ from biotite minerals of a syn-kinematic granitic dike. Thus, it is believed that this age data reflects the possible mineralization age of the Özyurt gold deposit.

Moreover, the presence of cataclastic deformation in the pre-existing high-angle fault network indicates brittle conditions during the hydrothermal activity period. Also, field evidence showing slickenlines along schist foliation (Figure 2.25) supports increasing brittle overprinting on ductile deformation during the exhumation.

In Figure 5.6, the first burial and exhumation cycle of the Niğde Massif is divided into four phases as D0, D1, D2 and D3. D0 phase marks the rapid burial of the Niğde Massif to peak metamorphic conditions. D1 phase starts with the exhumation of the Massif under the ductile deformation. D3 phase coincides with the latest stages of Üçkapılı Granite intrusion under brittle-ductile conditions. Finally, D4 shows the interval of brittle conditions operated during the late exhumation. Considering the youngest dike cooling age determined by Gautier et al. (2008), Özyurt Gold Deposit is thought to be formed at ~75 Ma. Therefore, the mineralization occurred approximately at a pressure of 3 kbar, depth of ~11 km and temperature of ~350 °C. This age and conditions are also consistent with observed dominant cataclastic deformation features in the field and polished thin sections. Also, during the mineralization, prehnite-pumpellyite to greenschist facies should have been present.

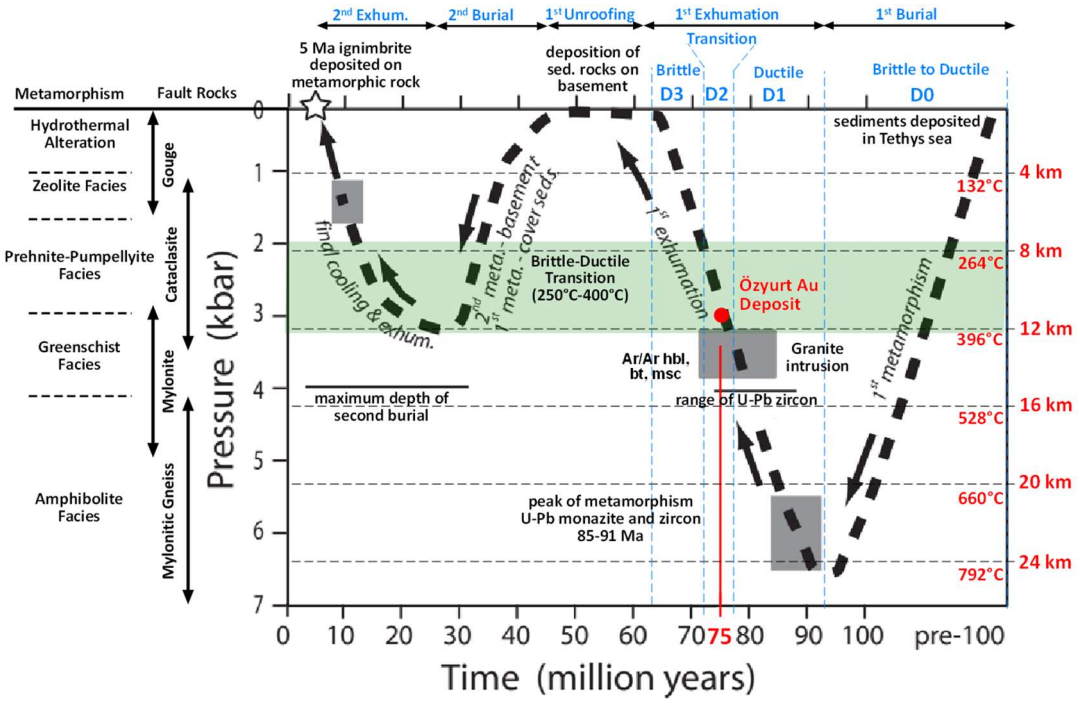

Figure 5.6. Pressure-Time-Depth diagram showing the burial and exhumation cycles of the Niğde Massif (modified from Umhoefer et al., 2007). The geothermal gradient is taken as 33 °C/km according to Gautier et al. (2008). Metamorphic facies and fault rocks depths are depicted according to temperature (adopted from Colvine et al., 1988; after Simpson 1986; Sibson, 1977, 1983).

5.3 Comparison of Özyurt Gold Deposit with Deposits within Central Anatolian Metamorphic Massifs

The Özyurt gold deposit shows the characteristics of gold mineralization within the high-grade metamorphics of the Niğde Massif. The gold mineralization along the foliation planes implies the timing of the mineralization occurred during the exhumation and coincided with the latest phases of granite intrusion. Several deposits and prospects within the Central Anatolian metamorphic massifs commonly show gold mineralization in such tectonic settings. The massifs generally host syn-tectonic intrusions emplaced during retrograde metamorphic conditions. Although, it is not proven yet; Genç and Yürür (2018) argues the possible relation of the gold mineralization with migmatites, high-grade metamorphic rocks and granitoids in Savcılıbeyit gold mineralization in the Kırşehir Massif.

Table 5.1. Comparison of several gold deposits/prospects in Central Anatolia based on their deposit-scale characteristics with proximal intrusions.

Deposit /Prospect	Tectonic Unit	Proximal Intrusion	Intrusion Age	Host rocks	Host structures and ore textures	Alteration	Ore mineralogy	Type	Reference study
Özyurt	Niğde Massif	Üçkapılı Granite	85 – 76 Ma zircon, U-Pb (Whitney et al., 2003)	mica schist dominantly, also gneiss	dissemination along the foliation, low-angle shear zones, subsequent high-angle shear zones, carbonate±sericite±chlorite veins	carbonation, sericitization, chloritization, argillization, rutile-ilmenite	pyrrhotite, marcasite, pyrite, arsenopyrite, lesser chalcopyrite, ±tetrahedrite, Supergene oxide: goethite, hematite, native Au, electrum	Orogenic Au	This study
Çimeli	Kırşehir Massif	Andesite porphry dike	No data	dominantly mica schists, lesser amphibolite	quartz veins, quartz-sulfide stockworks and brecciation within tectonic zones	silicification, quartz-sericite-carbonate±tourmaline assemblages	pyrite, galena, sphalerite, marcasite,chalcopyrite, bornite, magnetite minor chalcopyrite, bornite, magnetite, pyrrhotite, fahlerz group, secondary: scorodite, sericite, limonite, covellite	Orogenic Au	Avcı et al. 2022 Ali İlmer, personal communication
Savcılıbeyit	Kırşehir Massif	Cefalıkdağ-Baranadağ Granite	74.1±4.9 –69.3±0.4 Ma hornblende, Ar-Ar (Boztuğ et al., 2009)	migmatite, migmatitic gneiss, gneiss-schist-marble intercalation, calc-sillicate, gneiss and marble	quartz-sulifde veins, quartz-hematite limonite when oxidized	proximal: quartz-biotite-albite-calcite-chlorite-sericite±muscovite±epidote distal: chlorite-sericite-calcite	arsenopyrite, pyrite, pyrrhotite secondary hematite and limonite	Orogenic Au	Genç and Yürür, 2018
Terziali	Kırşehir Massif	Çayağzı Syenite	84.0±1.9 – 67.1±0.4 zircon, U-Pb; hornblende,Ar-Ar (Beyazpirinç et al.,2022); (Boztuğ et al., 2009)	metasedimentary rocks	breccia cements and clasts, and fine-grained grayish fracture-fill quartz veins within shear zones	Proximal: dravite, quartz, sericite/fuchsite and carbonate Distal: silicification	pyrite, Fe-oxides, lesser chalcopyrite and arsenopyrite	Orogenic Au	Sapancı et al. 2022
Kaymaz	Tavşanlı Zone	Kaymaz Granite	84.98 ± 6.27 and 33.3±2.0 – 42.5 ±2.2 zircon, U-Pb (Gautier, 1984); (Shin et al., 2013)	quartz-schists and serpentinites	quartz veins	silicification, argillization listwaenite	pyrite, arsenopyrite, marcasite, magnetite, pentlandite, millerite, nickeline, bravoite, native Au, silver	Low-sulfidation epithermal[1] Silica-listwaenite hosted[2]	Turan, 2018[1] Yavuz et al., 2022[2]
Himmetdede	Hırkadağ Massif	granitoid	No data	gneiss-marble intercalation	stockwork and disseminated sulfides, crack-joints	silicification, argillization	pyrite, arsenopyrite,enargite, galena, cassiterite, rutile	Low-sulfidation epithermal	Turan, 2018
Bakırtepe	Tauride-Göreli autochthon[3]	Kuluncak Syenite?	77.8±0.3 – 72.2±0.4 biotite and homblende,Ar-Ar (Boztuğ et al., 2009)	metasiltstone-metacarbonate-metasandstone contacts, metasandstone	quartz-hematite/magnetite±pyrite±gold veins within thrust zones	silicification, carbonatization[3] quartz-sericite-carbonate±tourmaline alteration [4] quartz-carbonate-clay alteration[4]	pyrite, hematite, magnetite, native Au	Orogenic Au	Uçurum et al. 2007[3] Dumanlılar et al. 2019[4]
Gümüşler	Niğde Massif	Üçkapılı Granite	85 – 76 Ma zircon, U-Pb (Whitney et al., 2003)	dominantly gneiss, rarely marble-gneiss contacts	stibnite-wolframite-cinnabar veins, cinnabar and stibnite disseminations and veinlets within breccia zones, tectonic zones[5] concordant and discordant cataclasites along foliation planes, low-angle faults juxtaposing marbles, schists [6]	silicification, dolomitization, kaolinitization, sericitization, chloritization, tourmalinitization, epidotization	stibnite, cinnabar, wolframite, lesser native Au[5] native gold, cinnabar, galena, marcasite, orpiment-realgar[6]	Orogenic Au[6]	Akçay, 1995[5] Tokoğlu et al. 2016[6]
Akçataş	Kırşehir Massif	Akçataş Granite	No data	granite	gold and silver in quartz matrix of breccias withing granite, uraninite in antimonite veins	kaolinitization, sericitization, silicification,	native Au, silver, arsenopyrite, pyrite, zeunerite, and stibnite with lesser sphalerite-pyrite	Low sulfidation epithermal	Turan, 2011

In Table 5.1, some of the prominent gold deposits and prospects in the Central Anatolia is given with their deposit characteristics and proximal intrusions. They are mutually associated with metamorphic host rocks. The host structures are generally veins or breccias formed along the tectonic zones and mostly have a similar alteration and ore mineralogy. Eventhough, Kaymaz, Himmetdede, and Akçataş are classified as low-sulfidation epithermal gold deposits, they share similar features with the orogenic gold deposits in the Central Anatolia which indicate that they can be also orogenic gold deposits as well. Another important feature is they commonly have a proximal intrusion. The available geochronology shows that Late Cretaceous intrusions are present near those deposits. This close association suggests that intrusions might have played a role on gold mineralization.

5.4 Comparison of Özyurt Gold Deposit with Orogenic Gold Deposits

Orogenic gold deposits (Böhlke, 1982; Groves et al., 1998) or mesothermal gold deposits (Lindgren, 1933), are hosted in metamorphic rocks and formed at depth of 5 to 15 km, at brittle-ductile to brittle conditions and at temperatures between 250°C-450°C (Kerrich and Cassidy, 1994), mostly under compressional tectonic settings like collisional and accretionary orogens (Tomkins, 2013). The gold is often transported via regional shear zones by the rapid rise of fluid due to fault-valve action caused by seismic activity (Sibson et al., 1988) and deposited into the higher order faults and veins (Figure 5.7) (Groves et al., 1998). The gold may be hosted in a variety of structures like brittle to ductile shear zones, fracture arrays, stockwork networks, breccia zones, foliated zones and the fold axes in turbidites (Groves et al., 1998). The gold is commonly associated with quartz veins or breccias and carbonation, sericitization and sulfidation alterations in the wall rock are observed (Groves et al., 1998). Hydrothermal fluids are characterized by low salinity, reducing, near neutral pH and have CO_2-H_2O±CH_4±N_2 (Groves et al., 1998, 2020).

Orogenic gold deposits in the world are generally restricted to three periods: (1) Neoarchean (2700 - 2400 Ma), (2) Paleoproterozoic (2100 - 1800 Ma) and (3) from 650 Ma to Phanerozoic (Goldfarb et al., 2001)

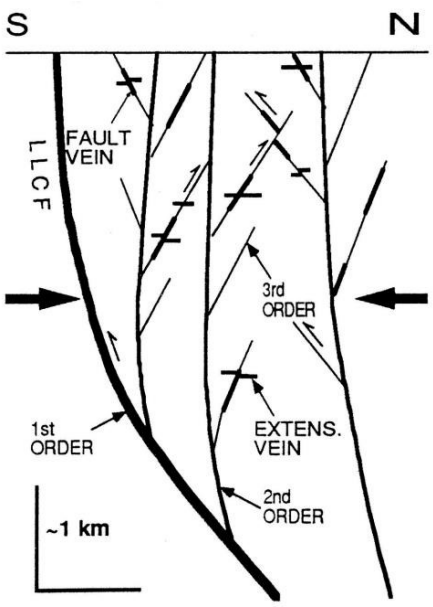

Figure 5.7. Fault order hierarchy in Val d'Or district (Robert, 1990).

The source of these deposits is not well-known but there are two candidates: (1) metamorphic rocks and (2) felsic to intermediate magmas (Tomkins, 2013). Magmatic-hydrothermal deposits are enriched in a variety of elements like S, Cu, Mo, Sb, Bi, W, Pb, Zn, Te, Hg, As, and Ag (Goldfarb et al., 2005; Richards, 2009). However, in many orogenic gold deposits, only S and As are enriched significantly. Therefore, the metamorphic source is the widely accepted model currently. (Goldfarb et al., 2005; Philips and Powell, 2010).

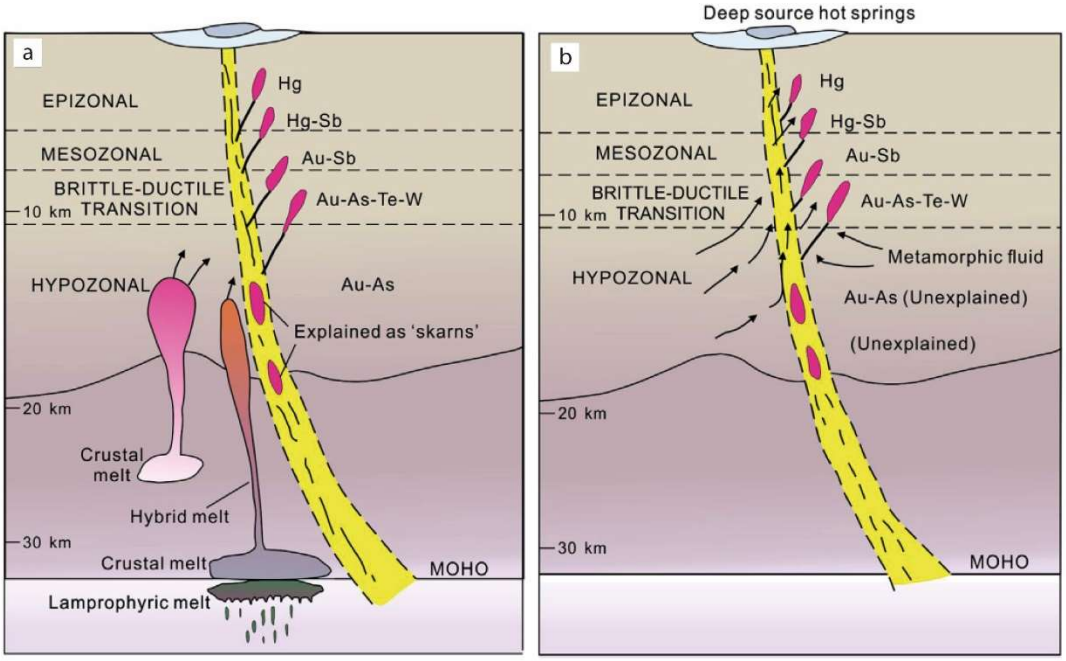

Figure 5.8. Proposed orogenic gold models according to different sources: (a) Magmatic-hydrothermal source model, (b) metamorphic source model (Groves and Santosh, 2016; Groves et al., 2020).

The Özyurt gold deposit resembles orogenic gold deposits in terms of its pyrrhotite-pyrite-arsenopyrite bearing relatively low-sulfidation ore mineralogy. By the formation of setting, it is formed at approximately 11 km depth and 350°C temperature coinciding with brittle to the brittle-ductile transition zone. The gold is hosted in the metamorphic rocks within the fault zones. Extensive carbonation and sericitization are observed in the Niğde Massif. Although vein alteration assemblages similarly include carbonate±sericite ±chlorite, the mineralization is not observed in quartz veins. Yet, late milky quartz veins with copper mineralization are also present in the massif. The mineralization age of the Özyurt gold deposit greatly differs from the classical orogenic gold deposits.

The proven presence of S, Cu, Sb, Pb, Zn, Hg, As, and Ag at some localities in the Niğde Massif and Üçkapılı Granite favors the magmatic-hydrothermal source model. Üçkapılı Granite is a crustal-derived melt formed by the partial melting of metamorphics; thus, it is believed that the granite may play an important role in the remobilization of the primary mineralization. The primary mineralization is

characterized as disseminated ore minerals within the foliation and observed widespread in the massif. The gold within this mineralization may be inherited from the protoliths of metamorphics. Lithologies like turbidites or black shales contain gold and arsenic within the diagenetic pyrite-arsenian pyrite and pyrrhotite, deposited under anoxic-euxinic reducing conditions (Large et al., 2011). Therefore, the mineralization at the Niğde Massif might have a metamorphic source inherited from protolith and remobilized and enriched with the granitic intrusion.

Özyurt gold deposit resembles an orogenic gold deposit considering its host rocks, structure, ore and alteration mineralogy and tectonic setting. The deposit is dominantly controlled by a fault network, it is classified as a shear-hosted gold deposit.

CHAPTER 6

CONCLUSIONS

The geology of the Özyurt gold deposit was studied at outcrop, deposit and micro scales by conducting fieldwork, 3D solid modeling and polished thin section studies. Concluding remarks regarding the deposit characteristic within a regional geological perspective can be summed as follows:

1. The competence between schist, marble and quartzite suggests that schist is a weaker lithology than the others for a significant depth range. Therefore, decoupled schists in between relatively competent marble and quartzite levels of the Niğde Massif are progressively deformed by layer-parallel shears while accommodating the exhumation and generating a permeable fault and fracture network.
2. The gold mineralization is controlled by structural and lithologic features. The architecture of the deposit consists of a series of high-angle fault networks with cataclastic breccias and foliation planes nearby to the faults. Gold is dominantly hosted within schists but also found at the schist and marble contacts as planar gossans which forms the cap of the system.
3. Both syn-tectonic dikes and the primary low-grade gold mineralization formed along foliation surfaces. This spatial relationship of indicates that hydrothermal activity and intrusion might have occurred coeval during the exhumation. Although, the direct relationship between intrusion and gold mineralization is not proven, the enriched element assemblages in the Niğde Massif suggest a magmatic-hydrothermal fluid source model may be valid for the massif.
4. Two mineralization phases were recognized by the polished thin section studies. The low-grade primary mineralization consists of disseminated marcasite-pyrrhotite-chalcopyrite±pyrite assemblages within the foliation

planes of schists interpreted as the massif-scaled main mineralization at the Niğde Massif. The high-grade secondary mineralization is composed of fracture and fault fill carbonate-pyrite and pyrite veinlets crosscut by arsenopyrite-pyrite-chalcopyrite±tetrahedrite mineral assemblages in carbonate±sericite±chlorite veins orthogonal to the foliation planes. The higher-grade gold mineralization is thought to be related with arsenopyrites of second mineralization phase.

5. Considering the gold should have been deposited as sulfide mineral assemblages and since the deposit is entirely oxidized, a late supergene stage should be present. Groundwater fluctuations and meteoric water percolation through time caused the breakdown of sulfides and liberated the gold to the fault zones. Moreover, low arsenic values in the Özyurt Gold Deposit unlike other mineralized sites in the massif may be washed away at the supergene stage. The low-grade primary mineralization is the hypogene ore while the high-grade secondary mineralization is enriched sulfide zone due to supergene enrichment.
6. The timing of the mineralization of Özyurt Gold Deposit is interpreted as ~75 Ma considering the youngest cooling age determined from dikes in the massif. Considering the burial and exhumation history of the Niğde Massif, the mineralization might have occurred at ~11 km depth and ~350°C temperature indicating brittle-ductile transition.
7. Özyurt Gold Deposit is an orogenic gold deposit considering its host rocks, structure, ore and alteration mineralogy and tectonic setting. Since the deposit is majorly controlled by a fault network, it is classified as a shear-hosted gold deposit.

REFERENCES

Advokaat, E. L. (2011). Tectono-stratigraphic evolution of the Ayhan Basin, Central Anatolia, Turkey: A Late Cretaceous to Early-Eocene supra detachment basin that underwent post-Lutetian compression and tilting (Master's thesis).

Advokaat, E. L., van Hinsbergen, D. J., Kaymakcı, N., Vissers, R. L., & Hendriks, B. W. (2014). Late Cretaceous extension and Palaeogene rotation-related contraction in Central Anatolia recorded in the Ayhan-Büyükkışla basin. International Geology Review, 56(15), 1813-1836.

Akçay, M. (1994). Genesis of the stibnite-cinnabar-scheelite deposits of the Gümüsler area, Nigde, central Turkey and implications on their gold potential. University of Leicester (United Kingdom).

Akçay, M., Moon, C. J., & Scott, B. C. (1995). Fluid inclusions and chemistry of tourmalines from the Gümüşler Sb-Hg+/-W deposits of the Niğde Massif (Central Turkey). Chemie Der Erde-Geochemistry, 55(3).

Akıman, O., Erler, A., Göncüoğlu, M. C., Güleç, N., Geven, A., Türeli, T. K., & Kadioğlu, Y. K. (1993). Geochemical characteristics of granitoids along the western margin of the Central Anatolian Crystalline Complex and their tectonic implications. Geological Journal, 28(3-4), 371-382.

Altuncu, S., Tümüklü, A., & Özgür, F. Z. (2018). Niğde Masifi Metalik Cevherleşmelerinin Mineralojisi ve Jeokimyasi. Niğde Ömer Halisdemir Üniversitesi Mühendislik Bilimleri Dergisi, 7(3), 1101-1106.

Andrew, T., & Robertson, A. H. (2002). The Beyşehir–Hoyran–Hadim Nappes: genesis and emplacement of Mesozoic marginal and oceanic units of the northern Neotethys in southern Turkey. Journal of the Geological Society, 159(5), 529-543.

Atabey, E., Göncüoğlu, M. C., & Turhan, N. (1990). Türkiye Jeoloji Haritaları Serisi, Kozan-J19 paftası, 1: 100 000. Maden Tetkik ve Arama, Ankara.

Avcı, S. A., Cengiz, İ., Önal, K., Cihan, İ., Seferoğlu, Ş., Kanaat, G., Kuşcu, E., Yıldız, A., Demirci, B., Ersoy, G. B., Çeli, A. E., Ergili, H., Düz, K., & Kesim, İ. B. (2022). Kırşehir Masifi'nde keşfedilen orojenik tip bir altın cevherleşmesinin özellikleri: Çimeli (Boztepe-Kırşehir) (Paper presentation). 74th Geological Congress of Turkey with international participation.

Aydın, N. S., Göncüoğlu, M. C., & Erler, A. (1998). Latest Cretaceous magmatism in the Central Anatolian Crystalline Complex: Review of field,

petrographic and geochemical features. Turkish Journal of Earth Sciences, 7(3), 259-268.

Ballı, F. (2017). Niğde yerleşim alanı güney ve doğu kesimlerinin jeolojik ve tektonik özellikleri (Master's thesis, Niğde Ömer Halisdemir Üniversitesi/Fen Bilimleri Enstitüsü).

Beyazpirinç, M., Akçay, A. E., Özkan, M. K., Sönmez, M. K., & Dönmez, M. The new age data and pre-Tertiary stratigraphy of the Kırşehir Massif, Central Anatolia. Bulletin of The Mineral Research and Exploration, 1-31.

Blumenthal, M. (1952). Das taurische Hochgebirge des Aladag: Neuere Forschungen zu seiner Geographie, Stratigraphie und Tektonik.

Blumenthal, M. M. (1941). Un aperçu de la géologie du Taurus dans les vilayets de Nigde et d'Adana. Verlag nicht ermittelbar.

Boztuğ, D. (1998). Post-collisional central Anatolian alkaline plutonism, Turkey. Turkish Journal of Earth Sciences, 7(3), 145-166.

Boztuğ, D. (2000). S-I-A-type intrusive associations: geodynamic significance of synchronism between metamorphism and magmatism in Central Anatolia, Turkey. Geological Society, London, Special Publications, 173(1), 441-458.

Boztuğ, D., Jonckheere, R. C., Heizler, M., Ratschbacher, L., Harlavan, Y., & Tichomirova, M. (2009). Timing of post-obduction granitoids from intrusion through cooling to exhumation in central Anatolia, Turkey. Tectonophysics, 473(1-2), 223-233.

Çağatay, A., & Pehlivan, R. (1988). Celaller (Niğde-Çamardı) Kalay Cevherleşmesinin Mineralojisi. Jeoloji Mühendisleri, 32-33.

Çemen, İ., Göncüoğlu, M. C., & Dirik, K. (1999). Structural evolution of the Tuzgölü basin in Central Anatolia, Turkey. The Journal of geology, 107(6), 693-706.

Chen, Y., & Nabelek, P. I. (2017). The influences of incremental pluton growth on magma crystallinity and aureole rheology: numerical modeling of growth of the Papoose Flat pluton, California. Contributions to Mineralogy and Petrology, 172(10), 1-16.

Colvine, A. C., Fyon, J. A., Heather, K. B., Marmont, S., Smith, O. M., & Troop, D. G. (1988). Archean lode gold deposits in Ontario (Vol. 139). Ontario Ministry of Northern Development and Mines.

Demircioğlu, R. & Coşkuner, B. (2020). Gümüşler- Özyurt (Niğde) Arasının Yapısal Özellikleri. ALKÜ Fen Bilimleri Dergisi, 2 (3), 125-138. Retrieved from https://dergipark.org.tr/en/pub/alku/issue/57701/763169

Demircioğlu, R., & Eren, Y. (2017). 'Çamardı (Niğde) Yöresinde Niğde Masifinin Yapısal Özellikleri. MTA Dergisi, 154, 15-26.

Dumanlılar, Ö., Cihan, İ., Ekmekçi, M., Kanaat, G., Aydoğan, C., & Turunç, O. Bakırtepe (Sivas-Kangal) altın cevherleşmelerinin oluşum ve zenginleşme evrelerinin kavramsal modeli. Yerbilimleri, 40(2), 136-167.

Düzgören-Aydin, N. S., Malpas, J., Göncüoğlu, M. C., & Erler, A. (2001). A review of the nature of magmatism in central Anatolia during the Mesozoic post-collisional period. International Geology Review, 43(8), 695-710.

Erdoğan, B., Akay, E., & Ugur, M. S. (1996). Geology of the Yozgat region and evolution of the collisional Çankırı basin. *International Geology Review*, *38*(9), 788-806.

Erler, A., & Göncüoglu, M. C. (1996). Geologic and tectonic setting of the Yozgat batholith, northern Central Anatolian Crystalline Complex, Turkey. International Geology Review, 38(8), 714-726.

Fayon, A. K., & Whitney, D. L. (2007). Interpretation of tectonic versus magmatic processes for resetting apatite fission track ages in the Niğde Massif, Turkey. Tectonophysics, 434(1-4), 1-13.

Fayon, A. K., Whitney, D. L., Teyssier, C., Garver, J. I., & Dilek, Y. (2001). Effects of plate convergence obliquity on timing and mechanisms of exhumation of a mid-crustal terrain, the Central Anatolian Crystalline Complex. Earth and Planetary Science Letters, 192(2), 191-205.

Gautier, P., Bozkurt, E., Bosse, V., Hallot, E., & Dirik, K. (2008). Coeval extensional shearing and lateral underflow during Late Cretaceous core complex development in the Niğde Massif, Central Anatolia, Turkey. Tectonics, 27(1).

Gautier, P., Bozkurt, E., Hallot, E., & Dirik, K. (2002). Dating the exhumation of a metamorphic dome: geological evidence for pre-Eocene unroofing of the Niğde Massif (Central Anatolia, Turkey). Geological Magazine, 139(5), 559-576.

Gautier, Y. (1984). Déformations et métamorphismes associés à la fermeture téthysienne en Anatolie centrale (région de Sivrihisar, Turquie) (Doctoral dissertation).

Gizaw, A. T. (1992). Geology and mineral deposits of Gümüsler area (Niğde, Türkiye) (Master's thesis, Middle East Technical University).

Goldfarb, R. J., Baker, T., Dube, B., Groves, D., Hart, C., & Gosslein, P. (2005). Distribution, character and genesis of gold deposits in metamorphic

terranes. In Economic Geology One Hundredth Anniversary Volume (pp. 407-450). Society of Economic Geologists.

Goldfarb, R. J., Groves, D. I., & Gardoll, S. (2001). Orogenic gold and geologic time: a global synthesis. Ore geology reviews, 18(1-2), 1-75.

Göncüoğlu, M. C. (1977). Geologie des Westlichen Nigde-Massivs. Ph. D. Thesis, Bonn Univ.

Göncüoğlu, M. C. (1981). Niğde masifinin jeolojisi. İç Anadolu'nun Jeolojisi Sempozyumu, Türkiye Jeoloji Kurultayı, 35, 16-19.

Göncüoğlu, M. C. (1986). Geochronological data from the southern part (Niğde area) of the Central Anatolian Massif. Mineral Research and Exploration Institute of Turkey (MTA) Bulletin, 105(106), 111-124.

Göncüoglu, M. C. (1992). Structural and stratigraphic framework of the Central Anatolian tertiary basins. Introduction to the Early Paleogene of the Haymana-Polatlı basin, Field-trip book IGCP Project, (286).

Göncüoğlu, M. C., & Türeli, K. (1993). Petrology and geodynamic interpretation of plagiogranites from central Anatolian ophiolites (Aksaray-Turkey). Turkish Journal of Earth Sciences, 2, 195-203.

Göncüoğlu, M. C., & Türeli, T. K. (1994). Alpine collision-type granitoids in the western central Anatolian crystalline complex. J Kocaeli Univ, 1, 39-46.

Göncüoğlu, M. C., Erler, A., Toprak, V., Olgun, E., Yalınız, K., Kuscu, I., ... & Dirik, K. (1993). Geology of the central part of the central Anatolian massif: part III geological evolution of the Tertiary Basin of the central Kızılırmak. Unpublished Report, 3313.

Göncüoglu, M. C., Erler, A., Toprak, V., Yaliniz, K. M., Olgun, E., & Rojay, B. (1992). Geology of the western part of the Central Anatolian Massif, Part 2: Central Section. Turkish Petroleum Corporation (TPAO) (No. 3155, p. 76). Report.

Göncüoğlu, M. C., Toprak, V., Kuşcu, İ., Erler, A., & Olgun, E. (1991). Orta Anadolu Masifinin batı bölümünün jeolojisi, Bölüm 1: Güney Kesim. Turkish Petroleum Corporation (TPAO) Report, 2909, 140.

Görür, N., Oktay, F. Y., Seymen, I., & Şengör, A. M. C. (1984). Palaeotectonic evolution of the Tuzgölü basin complex, Central Turkey: sedimentary record of a Neo-Tethyan closure. *Geological Society, London, Special Publications*, *17*(1), 467-482.

Görür, N., Tüysüz, O., & Celal Şengör, A. M. (1998). Tectonic evolution of the central Anatolian basins. *International Geology Review*, *40*(9), 831-850.

Groves, D. I., & Santosh, M. (2016). The giant Jiaodong gold province: the key to a unified model for orogenic gold deposits?. Geoscience Frontiers, 7(3), 409-417.

Groves, D. I., Santosh, M., & Zhang, L. (2020). A scale-integrated exploration model for orogenic gold deposits based on a mineral system approach. Geoscience Frontiers, 11(3), 719-738.

Gülyüz, E., Kaymakci, N., Meijers, M. J., Van Hinsbergen, D. J., Lefebvre, C., Vissers, R. L., ... & Peynircioğlu, A. A. (2013). Late Eocene evolution of the Çiçekdağı Basin (central Turkey): Syn-sedimentary compression during microcontinent–continent collision in central Anatolia. Tectonophysics, 602, 286-299.

Gürer, D., Plunder, A., Kirst, F., Corfu, F., Schmid, S. M., & van Hinsbergen, D. J. (2018). A long-lived Late Cretaceous–early Eocene extensional province in Anatolia? Structural evidence from the Ivriz Detachment, southern central Turkey. Earth and Planetary Science Letters, 481, 111-124.

Idleman, L., Cosca, M. A., Heizler, M. T., Thomson, S. N., Teyssier, C., & Whitney, D. L. (2014). Tectonic burial and exhumation cycles tracked by muscovite and K-feldspar 40Ar/39Ar thermochronology in a strike-slip fault zone, central Turkey. Tectonophysics, 612, 134-146.

İlbeyli, N. (2004). Field, petrographic and geochemical characteristics of the Hamit alkaline intrusion in the Central Anatolian Crystalline Complex, Turkey. Turkish Journal of Earth Sciences, 13(3), 269-286.

İlbeyli, N., & Pearce, J. A. (1997). Petrogenesis of the collision-related central Anatolian granitoids, Turkey. European Union Geosciences (EUG-9) Strasbourg, Abstract, 502.

İlbeyli, N., Pearce, J. A., Thirlwall, M. F., & Mitchell, J. G. (2004). Petrogenesis of collision-related plutonics in Central Anatolia, Turkey. *Lithos*, *72*(3-4), 163-182.

İleri, S. (1975). Antimuan yataklarında jeolojik konum ve jenez ilişkileri. TJK Bülteni, (18), 41-56.

İleri, S., & Köksoy, M. (1977). Türkiye antimuan yatakları oluşum ilkeleri. Yerbilimleri, 2(2), 95-114.

Kaymakcı, N., Özçelik, Y., White, S. H., & Van Dijk, P. M. (2009). Tectono-stratigraphy of the Çankırı Basin: late Cretaceous to early Miocene evolution of the Neotethyan suture zone in Turkey. Geological Society, London, Special Publications, 311(1), 67-106.

Kerrich, R., & Cassidy, K. F. (1994). Temporal relationships of lode gold mineralization to accretion, magmatism, metamorphism and

deformation—Archean to present: A review. Ore Geology Reviews, 9(4), 263-310.

Ketin, İ. (1955). On the geology of Yozgat region and the tectonic features of the Central Anatolian Massif (Kırşehir Crystallines). Bulletin of the Geological Society of Turkey VI (1), 1, 20.

Klein, van der, P. H. (1970). Recommendation of exploration for mineralizations in the SW part of the "Niğde-Çamardı massif. MTA Genel Müdürlüğü, Rapor, (4325).

Klein, van der, P. H., (1968). 'Field Report on the Geological and Geochemical Prospection in the Niğde–Çamardı Massiv. MTA. Maden Etüd Rapor No. M-174.

Klein, van der, P. H., (1971). Geochemical Patterns and Structural Alignments in Relation to Antimony-Mercury-Tungsten Mineralization in The Niğde Area. Turkey. Geologie en Minjbouw, 50, 763-764.

Köksal, S., Romer, R. L., Göncüoglu, M. C., & Toksoy-Köksal, F. (2004). Timing of post-collisional H-type to A-type granitic magmatism: U–Pb titanite ages from the Alpine central Anatolian granitoids (Turkey). International Journal of Earth Sciences, 93(6), 974-989.

Kuşcu, İ. (1992). Geological of the Çamardı-Niğde region and the madsan antimony deposit (Master's thesis, Middle East Technical University).

Kuşçu, İ., & Erler, A. (1999). Deformation of stibnites and pyrites in the Madsan antimony deposit (Niğde, Turkey): Implications for pressure-temperature conditions of local deformation. Turkish Journal of Earth Sciences, 8(1), 57-66.

Kuşcu, İ., Erler, A., & Göncüoğlu, M.C. (1992). Geology of the Çamardi (Niğde-Turkey) region. Geosound, Vol. v. 23, 1–16.

Kuşcu, İ., Kuşcu, G. G., Meinert, L. D., & Floyd, P. A. (2002). Tectonic setting and petrogenesis of the Çelebi granitoid,(Kırıkkale-Turkey) and comparison with world skarn granitoids. Journal of Geochemical Exploration, 76(3), 175-194.

Large, R. R., Bull, S. W., & Maslennikov, V. V. (2011). A carbonaceous sedimentary source-rock model for Carlin-type and orogenic gold deposits. Economic Geology, 106(3), 331-358.

Le Pennec, J. L., Bourdier, J. L., Froger, J. L., Temel, A., Camus, G., & Gourgaud, A. (1994). Neogene ignimbrites of the Nevsehir plateau (Central Turkey): stratigraphy, distribution and source constraints. Journal of Volcanology and Geothermal Research, 63(1-2), 59-87.

Lefebvre, C., Meijers, M. J., Kaymakcı, N., Peynircioğlu, A., Langereis, C. G., & Van Hinsbergen, D. J. (2013). Reconstructing the geometry of central Anatolia during the late Cretaceous: Large-scale Cenozoic rotations and deformation between the Pontides and Taurides. Earth and Planetary Science Letters, 366, 83-98.

Lindgren, W. (1933). Mineral Deposits, McGraw-Hill Book Company. Inc. New York.

Lünel, A. T. (1985). An approach to the naming, origin and age of Baranadağ monzonite of the Kırşehir intrusive suite. METU Journal of pure and Applied Sciences, 18(3), 385-404.

Okay, A. C. (1955). Niğde-Çamardı ve Ulukışla arasındaki bölgenin jeolojisi. Ankara, MTA Derleme, (2381).

Oktay, F. Y. (1982). Stratigraphy and Geological evolution of the Ulukışla and Surrounding Area. Geological Bulletin of Turkey, 25(1), 15-23.

Oygür, V., Güyer, F., & Yıldırım, S. (1985), Niğde masifi kuzey kesimi demir projeksiyonu jeolojisi raporu. MTA Raporu, No:169.

Özgüneyli, A. (1978). Niğde-Çamardı Kristalin masifi genel prospeksiyon çalışması ve demir-baz metal-wolfram ve altın cevherleşmeleri hakkında çalışma raporu: MTA Maden etüd arşivi no: 1710.

Özözlü, A. M. (2019). Ulukışla (Niğde) havzasındaki Esendemir tepe skarn ve Horoz skarn mineralizasyonlarının karşılaştırmalı incelemesi (Master's thesis, Dokuz Eylül Üniversitesi/Fen Bilimleri Enstitüsü).

Parlak, O., & Robertson, A. (2004). The ophiolite-related Mersin Melange, southern Turkey: its role in the tectonic–sedimentary setting of Tethys in the Eastern Mediterranean region. *Geological Magazine*, *141*(3), 257-286.

Passchier, C. W., & Trouw, R. A. (2005). Microtectonics. Springer Science & Business Media.

Phillips, G. N., & Powell, R. (2010). Formation of gold deposits: a metamorphic devolatilization model. Journal of Metamorphic geology, 28(6), 689-718.

Phillipson, A. (1918). Kleinasien, Handbuch der Regionalen Geologie, 2/2. Carl Winters Universitätsbuchhandlung: Heidelberg, Germany.

Powell, W., Yazgan, E., Johnson, M., Yener, K. A., & Mathur, R. (2021). Mineralogical analysis of the Kestel Mine: An early bronze age source of tin ore in the Taurus Mountains, Turkey. *Minerals*, *11*(1), 91.

Radwany, M., Morgan, L. E., & Whitney, D. L. (2020). Conditions and timing of incorporation of ophiolite into orogenic crust during oblique convergence, Central Anatolia. International Journal of Earth Sciences, 109(7), 2393-2406.

Radwany, M., Whitney, D. L., Brocard, G., Umhoefer, P. J., & Teyssier, C. (2017). Ophiolite gabbro from source to sink: A record of tectonic and surface processes in Central Anatolia. Geosphere, 13(5), 1329-1358.

Ray, M. (2016). Petrogenesis of the Niğde Mafic Complex, Turkey: implications for the tectonic and geomorphic evolution of Central Anatolia. (Master's thesis, University of Minnesota)

Richards, J. P. (2009). Postsubduction porphyry Cu-Au and epithermal Au deposits: Products of remelting of subduction-modified lithosphere. Geology, 37(3), 247-250.

Robb, L. (2005). Introduction to ore-forming processes. John Wiley & Sons.

Robert, F. (1990). An overview of gold deposits in the eastern Abitibi belt: Canadian Institute of Mining and Metallurgy Special.

Rutter, E. H., & Brodie, K. H. (2004). Experimental grain size-sensitive flow of hot-pressed Brazilian quartz aggregates. *Journal of Structural Geology*, *26*(11), 2011-2023.

Safalı, M. (2019). Çamardı (Niğde) Antimuan cevherleşmesinin mineralojik petrografik ve jeokimyasal özelliklerinin incelenmesi (Master's thesis, Niğde Ömer Halisdemir Üniversitesi/Fen Bilimleri Enstitüsü).

Sapancı, Ö., Köprübaşı, N., Çiftçi, E., Köprübaşı, N., Tokat, G., & Demir, Y. (2022). Mineralogy, geochemistry, fluid inclusion, and stable sulfur isotope investigation of the Terziali shear-related orogenic gold deposit (Central Anatolia, Turkey): implications for ore genesis and mineral exploration. Arabian Journal of Geosciences, 15(1), 1-19.

Schmid, S. M., Paterson, M. S., & Boland, J. N. (1980). High temperature flow and dynamic recrystallization in Carrara marble. Tectonophysics, 65(3-4), 245-280

Şengör, A. C., & Yilmaz, Y. (1981). Tethyan evolution of Turkey: a plate tectonic approach. *Tectonophysics*, *75*(3-4), 181-241.

Seyitoğlu, G., Işık, V., Gürbüz, E., & Gürbüz, A. (2017). The discovery of a low-angle normal fault in the Taurus Mountains: the İvriz detachment and implications concerning the Cenozoic geology of southern Turkey. Turkish Journal of Earth Sciences, 26(3), 189-205.

Seymen, I. (1981). Stratigraphy and metamorphism of the Kırşehir Massif around Kaman (Kırşehir-Turkey). Bulletin of Geological Society of Turkey, 24.

Shea Jr, W. T., & Kronenberg, A. K. (1993). Strength and anisotropy of foliated rocks with varied mica contents. Journal of Structural Geology, 15(9-10), 1097-1121.

Shin, T. A., Catlos, E. J., Jacob, L., & Black, K. (2013). Relationships between very high pressure subduction complex assemblages and intrusive granitoids in the Tavşanlı Zone, Sivrihisar Massif, central Anatolia. Tectonophysics, 595, 183-197.

Sibson, R. H. (1977). Fault rocks and fault mechanisms. Journal of the Geological Society, 133(3), 191-213.

Sibson, R. H. (1983). Continental fault structure and the shallow earthquake source. Journal of the Geological Society, 140(5), 741-767.

Simpson, C. (1986). Determination of movement sense in mylonites. Journal of Geological Education, 34(4), 246-261.

Tchihatcheff, P. A. de., (1869). Asie Mineure: Description physique, statistique etarchéologique de cette contrée, Quatrième Partie, Géologie III. Paris: L. Guerin.

Tekeli, O., Aksay, A., Urgun, B. M., & Isik, A. (1984). Geology of the Aladag mountains. In Geology of the Taurus belt. International symposium (pp. 143-158).

Tokay, B. (2015). Structural and kinematic analysis of a transpressional basin: Çiçekdağ Basin.

Tokoğlu, M., Kuşcu, İ., & Kaymakcı. (2016). Structural Control on a Shear Zone Hosted Gold Mineralization in Gümüşler, Niğde (Turkey). SEG-MJD 2016 Conference

Tomkins, A. G. (2013). On the source of orogenic gold. Geology, 41(12), 1255-1256.

Toprak, V. (1998). Vent distribution and its relation to regional tectonics, Cappadocian Volcanics, Turkey. Journal of Volcanology and Geothermal Research, 85(1-4), 55-67.

Tosunbaş, O. (2019). Gümüşler (Niğde) Antimuan cevherleşmesinin metalojenik incelenmesi (Master's thesis, Fen Bilimleri Enstitüsü).

Tromp, W. (1942). Kayseri, Niğde, Tuzgölü arasının jeolojisi. Maden Tetkik ve Arama Genel Müdürlüğü Rapor, (1456).

Tümüklü, A., & Tosunbaş, O. (2021). Gümüşler (Niğde) Antimon (Sb) cevherleşmesinin mineralojik ve jeokimyasal araştırılması. Gazi

University Journal of Science Part A: Engineering and Innovation, 8(1), 166-188.

Tümüklü, A., Altuncu, S., & Özgur, F. (2016). Mineralogy of the iron mineralizations associated with the Üçkapılı granitoid (Niğde Massif). Int. J. Eng. Res. Man, 3, 2058-2349.

Tümüklü, A., Altuncu, S., & Özgür, F. Z. (2018). Niğde Masifinin maden yatakları yönünden değerlendirilmesi. Niğde Ömer Halisdemir Üniversitesi Mühendislik Bilimleri Dergisi, 7(3), 1119-1123.

Turan, T. İ. (2011). Akçataş (Hacıbektaş-Nevşehir altın-uranyum-antimuan cevherleşmesinin tip özellikleri. (Master's thesis, Hacettepe University).

Turan, T. İ. (2018). Kaymaz (Eskişehir) ve Himmetdede (Kayseri) Altın yataklarının jeolojik özelliklerinin karşılaştırılması. (Doctoral dissertation, Hacettepe University).

Uçurum, A., Usman, A., Lechler, P. J., Arehart, G. B., & Molnar, F. (2007). Geology, geochemistry, stable isotope, and fluid inclusion investigation of the Iron oxide-gold mineralization in Bakir Tepe, Kangal-Sivas, east-central Turkey. International Geology Review, 49(8), 753-767.

Umhoefer, P. J., Thomson, S. N., Lefebvre, C., Cosca, M. A., Teyssier, C., & Whitney, D. L. (2020). Cenozoic tectonic evolution of the Ecemiş fault zone and adjacent basins, central Anatolia, Turkey, during the transition from Arabia-Eurasia collision to escape tectonics. Geosphere, 16(6), 1358-1384.

Umhoefer, P. J., Whitney, D. L., Teyssier, C., Fayon, A. K., Casale, G., & Heizler, M. T. (2007). Yo-yo tectonics in a wrench zone, Central Anatolian fault zone, Turkey. Special Paper of the Geological Society of America, 434, 35-57.

Vache, R. (1963). Akdağmadeni kontakt yatakları ve bunların Orta Anadolu Kristalinine karşı olan jeolojik çerçevesi. Bulletin of the Mineral Research and Exploration, 60(60), 22-36.

van Hinsbergen, D. J., Maffione, M., Plunder, A., Kaymakcı, N., Ganerød, M., Hendriks, B. W., ... & Vissers, R. L. (2016). Tectonic evolution and paleogeography of the Kırşehir Block and the Central Anatolian Ophiolites, Turkey. Tectonics, 35(4), 983-1014.

Viljoen, R. P., & İleri, S. (1973). The Geology and mineralization of partions in the Pozantıdağı (Niğde) Massif of South Central Turkey. Johannesburg Consolidated Investments Co. Ltd. Geological. Research Department. Unpublished Rep, (39).

Whitney, D. L., & Dilek, Y. (1997). Core complex development in central Anatolia, Turkey. Geology, 25(11), 1023-1026.

Whitney, D. L., & Dilek, Y. (1998). Metamorphism during Alpine crustal thickening and extension in Central Anatolia, Turkey: The Niğde metamorphic core complex. Journal of Petrology, 39(7), 1385-1403.

Whitney, D. L., & Dilek, Y. (2001). Metamorphic and tectonic evolution of the Hırkadağ block, Central Anatolian Crystalline Complex. Turkish Journal of Earth Sciences, 10(1), 1-15.

Whitney, D. L., & Hamilton, M. A. (2004). Timing of high-grade metamorphism in central Turkey and the assembly of Anatolia. Journal of the Geological Society, 161(5), 823-828.

Whitney, D. L., Teyssier, C., & Heizler, M. T. (2007). Gneiss domes, metamorphic core complexes, and wrench zones: Thermal and structural evolution of the Niğde Massif, central Anatolia. Tectonics, 26(5).

Whitney, D. L., Teyssier, C., Dilek, Y., & Fayon, A. K. (2001). Metamorphism of the Central Anatolian Crystalline Complex, Turkey: Influence of orogen-normal collision vs. wrench-dominated tectonics on P–T–t paths. Journal of Metamorphic Geology, 19(4), 411-432.

Whitney, D. L., Teyssier, C., Fayon, A. K., Hamilton, M. A., & Heizler, M. (2003). Tectonic controls on metamorphism, partial melting, and intrusion: timing and duration of regional metamorphism and magmatism in the Niğde Massif, Turkey. Tectonophysics, 376(1-2), 37-60.

Whitney, D. L., Umhoefer, P. J., Teyssier, C., & Fayon, A. K. (2008). Yo-yo tectonics of the Niğde Massif during wrenching in Central Anatolia. Turkish Journal of Earth Sciences, 17(2), 209-217.

Yalınız, M. K., & Göncüoğlu, M. C. (1998). General geological characteristics and distribution of the Central Anatolian Ophiolites. Yerbilimleri, (20), 19-30.

Yalınız, M. K., Floyd, P. A., & Göncüoğlu, M. C. (1996). Supra-subduction zone ophiolites of Central Anatolia: geochemical evidence from the Sarikaraman ophiolite, Aksaray, Turkey. Mineralogical Magazine, 60(402), 697-710.

Yalınız, M. K., Göncüoğlu, M. C., & Özkan-Altıner, S. (2000). Formation and emplacement ages of the SSZ-type Neotethyan ophiolites in central Anatolia, Turkey: Palaeotectonic implications. Geological Journal, 35(2), 53-68.

Yavuz, H., Demir, Y., Kasapçı, C., Uysal, İ., & Helvacı, C. (2022). Geology and genesis of the Silica-listwaenite hosted Kaymaz gold deposit,

Eskişehir, NW-Turkey: Implications from fluid inclusions and pyrite chemistry. Journal of Asian Earth Sciences: X, 8, 100104.

Yetiş, C. (1978). Geology of the Çamardi (Niğde) region and characteristics of the Ecemiş Fault Zone between Maden Boğazı and Kamışlı. İstanbul, Üniversitesi Fakültesi Mecmuası Seri B, 43, 41-61.

Yıldız, M. C. (1976). Türkiye'de bazı cıva yataklarının oluşum ve mukayesesi. (Doctoral dissertation, İTÜ).

APPENDICES

A. Offsets of a carbonate vein due to shearing along foliation planes of gneiss

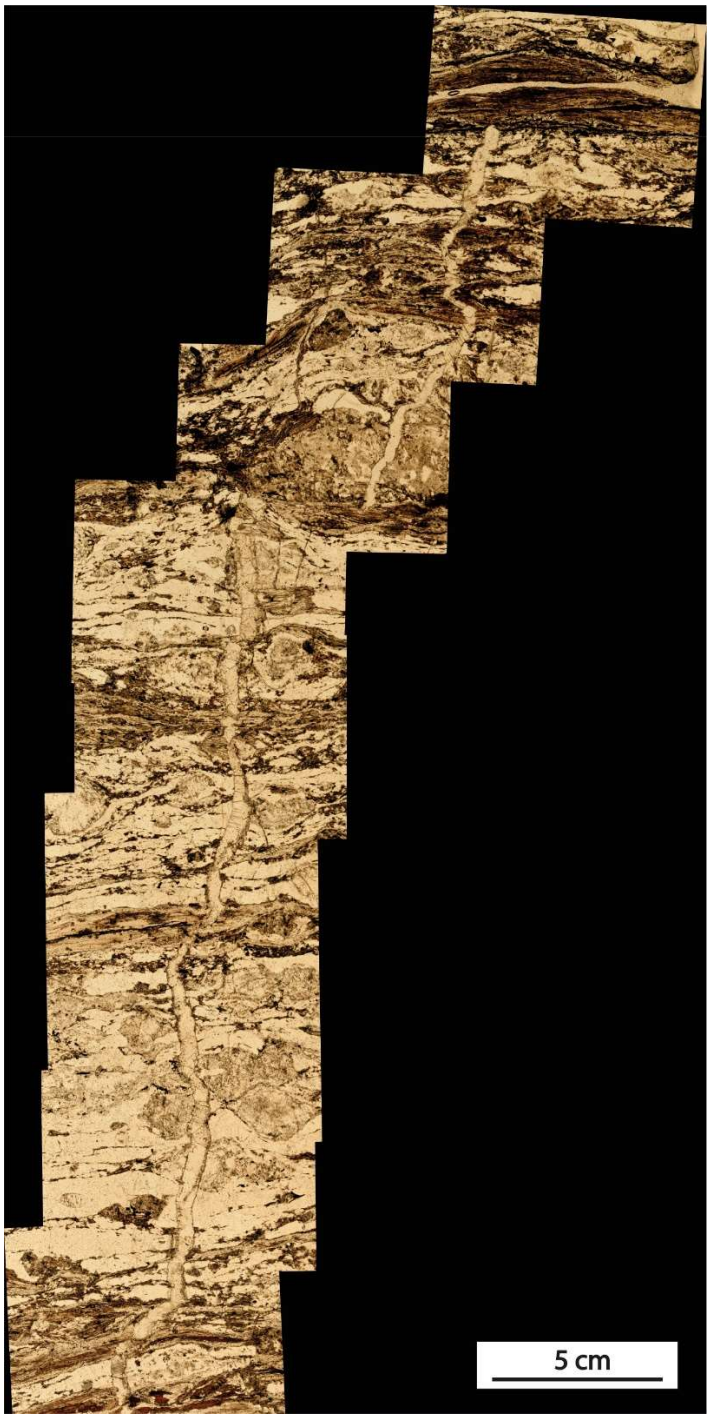

B. Composite image of sericite-carbonate-pyroxene-albite rich layer between quartz-mica layers and ore minerals in the contact of them

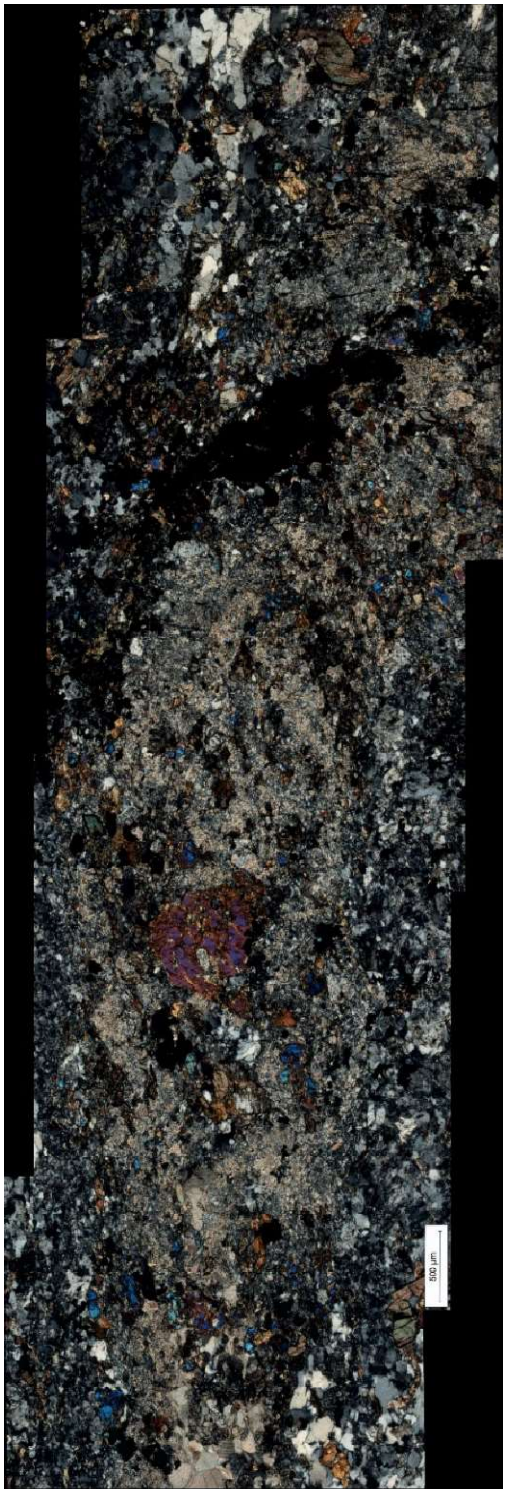

C. The contact of quartz and pyroxene-rich layers

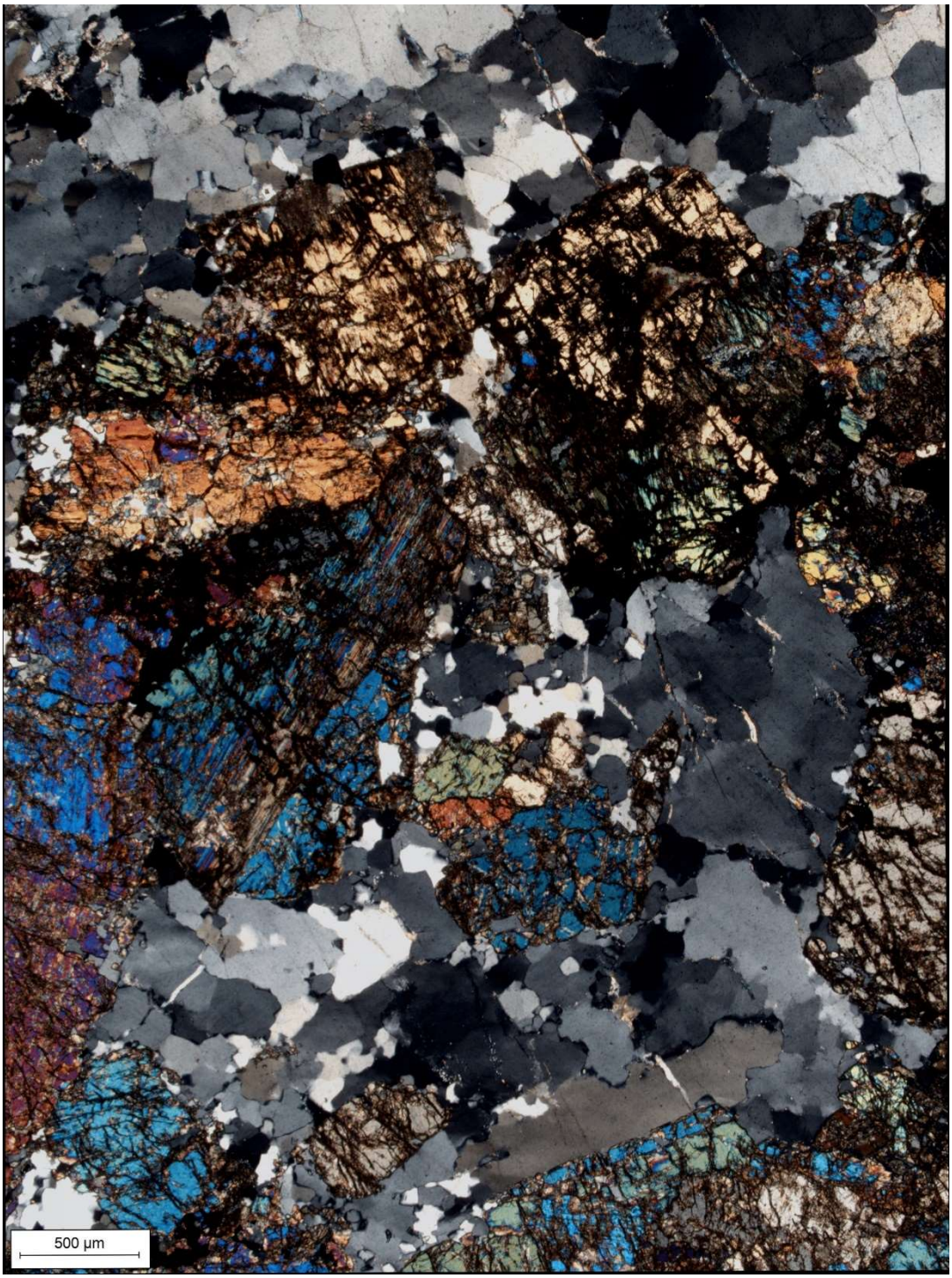

D. Stage 1 sooty textured colloform marcasite-pyrrhotite-chalcopyrite within a clay-carbonate vein replaced by subhedral, fresh-looking pyrite of stage 2

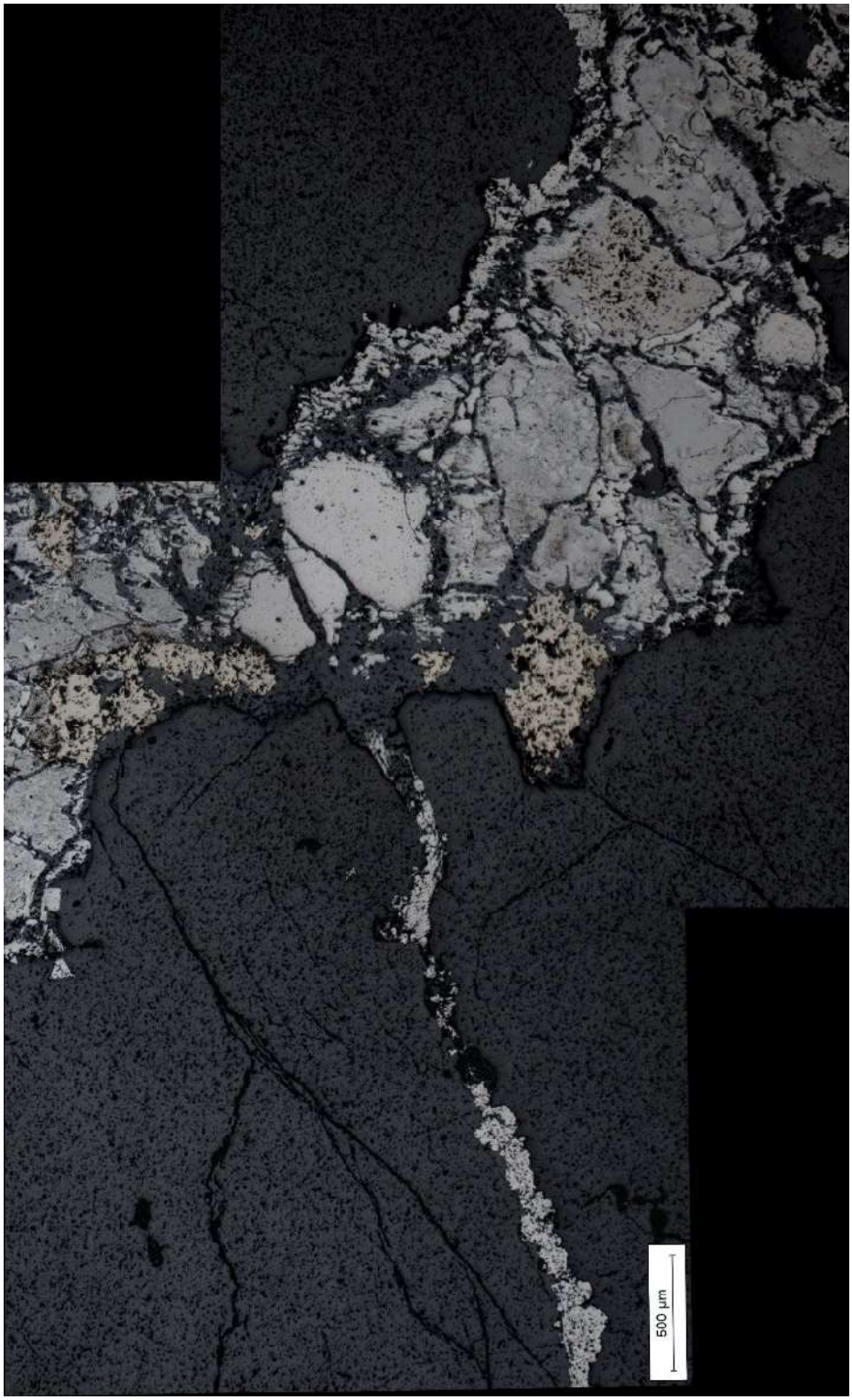

E. Stage 2 pyrite veinlets formed along fractures

F. Stage 3 pyrite within carbonate-chlorite vein crosscutting the foliation